COUPLED PLASMONIC STRUCTURES FOR SENSING, ENERGY AND SPECTROSCOPY APPLICATIONS

A DISSERTATION SUBMITTED TO

THE GRADUATE SCHOOL OF ENGINEERING AND SCIENCE

OF BILKENT UNIVERSITY

IN PARTIAL FULFILLMENT OF THE REQUIREMENTS FOR

THE DEGREE OF

DOCTOR OF PHILOSOPHY

IN

MATERIALS SCIENCE AND NANOTECHNOLOGY PROGRAM

By

Sencer Ayas

August, 2015

I certify that I have read this thesis and that in my opinion it is fully adequate, in scope and in quality, as a thesis of the degree of Doctor of Philosophy.

…….

Assist. Prof. Dr. Aykutlu Dana (Advisor)

I certify that I have read this thesis and that in my opinion it is fully adequate, in scope and in quality, as a thesis of the degree of Doctor of Philosophy.

…….

Assist. Prof. Dr. Necmi Biyikli

I certify that I have read this thesis and that in my opinion it is fully adequate, in scope and in quality, as a thesis of the degree of Doctor of Philosophy.

…….

Assoc. Prof. Dr. Ozgur Oktel

I certify that I have read this thesis and that in my opinion it is fully adequate, in scope and in quality, as a thesis of the degree of Doctor of Philosophy.

…….

Assoc. Prof. Dr. Hamza Kurt

I certify that I have read this thesis and that in my opinion it is fully adequate, in scope and in quality, as a thesis of the degree of Doctor of Philosophy.

…….

Assist. Prof. Dr. Mehmet Solmaz

Approved for the Graduate School of Engineering and Science:

…….

Prof. Dr. Levent Onural

Director of the Graduate School

ABSTRACT

COUPLED PLASMONIC STRUCTURES FOR SENSING, ENERGY AND SPECTROSCOPY APPLICATIONS

Sencer Ayas

Ph.D. in Material Science and Nanotechnology Program

Supervisor: Assist. Prof. Dr. Aykutlu Dana

August, 2015

Recent advances in nanofabrication and characterization methods have enabled the study of novel optical phenomena, thus boosting the research in nanophotonics and plasmonics. Metal nanostructures offer a route for the excitation of surface plasmons by confining the light in sub-wavelength dimensions, yielding extremely high electromagnetic field intensities. Moreover, coupling different plasmon modes offers a rich optical dispersion which cannot be obtained inherently by using single plasmonic resonator. In this thesis, we first present a detailed study of simple coupled plasmonic structures based on metal-insulator-metal structure. Then, we use similar structures to devise novel optical platforms in various applications such as surface enhanced Raman spectroscopy (SERS), surface enhanced infrared absorption spectroscopy (SEIRA) and plasmon enhanced hot-electron devices.

The first part of this thesis concentrates on coupled plasmonic structures and their spectroscopy and photodetector applications. Firstly, we study these structures numerically and analytically and show surface enhanced Raman spectroscopy (SERS) as a possible application with uniform signal intensities over large areas. Then, fabricating these plasmonic surfaces with sub-10nm gaps over large areas lead to development of single molecule Raman spectroscopy platforms. As an energy related application, a contact free characterization method is developed to probe hot electrons where similar coupled plasmonic surfaces are employed as hot electron devices. Finally, using aluminum and its native aluminum oxide hierarchical plasmonic surfaces are fabricated and its spectroscopy applications are demonstrated.

In the second part of, we develop interference-coating-based sensing platforms in the visible and infrared wavelengths. Despite large field enhancements, plasmonic

structures suffer from low signal intensities due to low mode volumes. To overcome this issue we propose another strategy, namely using interference coatings with small and uniform electric field enhancements over large mode volumes. These surfaces outperform the conventional plasmonic surfaces when they are used as infrared absorption spectroscopy platforms. Finally, similar surfaces are employed as colorimetric sensor platforms to sense monolayer and bilayer proteins simply by change in the surface color.

Keywords: Surface plasmons, coupled plasmons, spectroscopy, hot-electrons, interference coatings, optical sensors

ÖZET

Eşlenmiş Plazmonik Yapıların Sensör, Enerji ve Spektroskopi Uygulamaları

Sencer Ayas
Malzeme Bilimi ve Nanoteknoloji Programı, Doktora
Tez Yöneticisi: Assist. Prof. Dr. Aykutlu Dana
Ağustos, 2015

Nanofabrikasyon ve karakterizasyon metotlarındaki yeni gelişmeler yenilikçi optik çalışmaları hızlandırmış, bu da nanofotonik ve plazmonik çalışmalarında ciddi bir artışa sebep olmuştur. Metal nano-yapılar ışığı dalga boyundan çok küçük boyutlara hapsederek yüzey plazmonlarının uyarılması sağlayarak elektromanyetik alan şiddetini arttırmaktadır. Diğer yandan, farklı plazmon modlarının eşlenmesi tek plazmonik rezonatör yapısıyla elde edilemeyecek çok zengin bir optik bant yapısı sunmaktadır. Bu tezde, ilk olarak metal-dielektrik-metal rezonatör yapısı baz alınarak eşlenik plazmon yapıları detaylı olarak çalışılmıştır. Sonra, benzer yapılar kullanılarak yenilikçi optik platformlar üretilerek yüzey artırımlı Raman spektroskopisi (SERS), yüzey artırımlı kızılötesi emilim spektroskopisi (SEIRA) ve plazmon artırımlı sıcak elektron aygıt uygulamaları gösterilmiştir.

Tezin ilk kısmı plazmonik yapılar ve bu yapıların spektroskopi ve fotodetektör uygulamalarına yoğunlaşmıştır. İlk olarak, bu yapıları analitik ve numerik olarak çalışarak geniş alanlarda sabit artırımlı SERS uygulaması gösterilmiştir. Sonra, benzer yapıların 10nm'den küçük aralıklı olarak üretilmesiyle tek molekül Raman spektroskopisi uygulaması gösterilmiştir. Enerji uygulaması olarak da benzer eşlenik plazmonik yapıları kullanılarak sıcak elektronların ölçüldüğü XPS tabanlı bir yöntem geliştirilmiştir. Son olarak da aluminyum ve doğal aluminyum oksit tabakası kullanılarak hiyerarşik plazmonik yapıları üretilerek spektroskopi uygulamaları gösterilmiştir.

Tezin ikinci kısmında görünür ve kızılötesi dalga boylarında girişim kaplamasına dayanan sensör platformları geliştirilmiştir. Plazmonik yapılar elektromanyetik alan şiddetini çok fazla arttırmalarına rağmen, moleküllerin sinyal şiddetleri mod

hacminin küçüklüğünden dolayı azdır. Bu problemi aşmak için yeni girişim kaplamalara dayalı yeni bir strateji önerilmektedir. Bu yüzeyler kızılötesinde kullanıldıklarında plazmonik yüzeylerden daha iyi performans göstermektedirler. Son olarak da benzer yüzeyler görünür bölgede tek ve çift tabakalı proteinleri renk değişimine bağlı olarak tespit etmek için önerilmektedir.

Anahtar kelimeler: Yüzey plazmonları, eşlenik plazmonlar, spektroskopi, sıcak elektronlar, girişim kaplamaları, optik sensörler

Acknowledgement

I would like to thank my PhD advisor Aykutlu Dâna for accepting me as a PhD student in his group. This thesis would not be successful without his efforts, guidance and support. I have learnt a lot from him; mathematical modeling, coding and tips about clean room processes are few of them. I wouldn't ask for a better advisor.

I would like to thank Prof. Salim Çıracı for accepting me to PhD program.

I would like to thank my thesis committee; Assist. Prof. Necmi Bıyıklı, Assoc. Prof. Mehmet Özgür Oktel, Assist. Prof. Mehmet Ertuğrul Solmaz and Assoc. Prof. Hamza Kurt.

I would like to thank some of my present and past group members; Dr. Gökhan Bakan, Dr. Kemal Çelebi, Hasan Güner, Andi Çupallari, Mustafa Ürel, Ahmet Emin Topal and Serkan Karayalçın. I would especially thank Gökhan and Kemal for being good friends and editing this thesis' drafts. I want to thank Andi for being good friend and companion. He is one of the handy people I have known who made things happen easily; especially clean room processes. I want to thank Mustafa for AFM roughness measurements. I would like to thank Mehmet Kanık for FTIR measurements, graphical illustrations and for being a good friend.

I want to thank Mehmet Ertuğrul Solmaz for partially supporting me for the last 8 months of my PhD.

I would like to thank clean room engineers and technicians; particularly Semih Yaşar, Murat Dere and Mustafa Güler.

I greatly acknowledge TUBITAK through grant 111M344.

Finally, I thank my family for encouraging and supporting me to complete my PhD work.

Contents

List of Figures

heavy atom, with a multiple localized states. (c) In a one-dimensional periodic arrangement of the light atoms, coupling through the surface plasmon mode can introduce a coupling of the LFPs and propagating bands can be formed. (d) Similarly, in a one-dimensional periodic arrangement of the MIM structures with a relatively thick top metal and a thin gap dielectric, the MIM modes and the LFP mode formed between consecutive MIMs are hybridized to form a diatomic molecule. The molecules are coupled to form the band structure of the diatomic crystal. (e) Effect of mode coupling is observed in the reflection coefficient, plotted as a function of wavelength and dielectric thickness, *h*, for a one-dimensional crystal. Numerical computation results are shown for a 250 nm period structure with 180 nm MIM width, for normal incidence. Resonance wavelengths are calculated using the Fabry–Perot resonator model for the MIM structures (black lines; see text for details) that are superimposed. Antisymmetric modes (even mode number *m*) are not coupled to the free-space modes at normal incidence and, therefore, contribute no absorption (arrow (i)). The LFP mode wavelength is estimated using the LC model (vertical line around 520 nm, denoted by arrow (ii)). (f) Reflection coefficient is plotted as a function of wavelength and dielectric thickness *h* at a 10° angle of incidence. Due to the broken symmetry, even modes also contribute to absorption. (g) Lumped circuit model for the diatomic unit cell consists of a transmission line capacitively coupled to a localized LC resonator representing the LFP mode. The model is used to calculate the resonance frequencies of the modes, plotted as dots, on top of the computational results in (f). The model captures the essential features of numerical calculations such as the resonance frequencies and anticrossing behavior due to coupling of modes. 19

Figure 2-7. (a) Band structure of a monatomic meta-surface is calculated using the circuit model in Figure 2g and the ABCD matrix approach and superimposed on the reflection obtained through numerical calculations. When the dielectric thickness is zero, only the bands formed are through coupling of the LFP (arrow I) modes via the surface plasmon mode (arrow II) are observed. (b) Increasing the gap to 3 nm results in the appearance of a large number of MIM modes and formation of a diatomic meta-surface. (c) Increasing the gap to 13 nm results in a reduction of the number of MIM modes, while increasing the absorption in the coupled bands due to improved impedance matching of the surface with free-space propagating modes. Further band

List of Tables

Chapter 1

Introduction

Surface plasmons are known as propagating electromagnetic waves at metal-dielectric interfaces. The field of plasmonics deals with interaction of electromagnetic waves with metal surfaces and nanostructures. Since, the surface plasmon field is tightly confined to the interface; electromagnetic field intensity is enhanced at the metal-dielectric interface. Various optical sensors[1]–[3], interconnects[4]–[7], photodetectors[8]–[11], optical elements[12] and photovoltaic devices[13], [14] utilize such unique characteristic of surface plasmons. There are different ways of exciting surface plasmons at metal-dielectric interfaces such as electrons and light[15]–[17]. Among the excitation sources, light is the most common and easiest way of exciting surface plasmons[18].

Metallic nanoparticles, on the other hand, provide an easier route for plasmonics research due to ease of fabrication and characterization methods[15], [19], [20]. Various fabrication methods are utilized plasmonic metallic nanoparticles. E-beam lithography[21], [22], focused ion-beam lithography[23], nano-imprint lithography[24], [25], interference lithography[26] and nano-sphere lithography[27], [28] are among the top-down fabrication methods where nanoparticles with uniform size distributions can be fabricated. Despite the uniformity and resolution of fabricated devices, top-down fabrication methods like e-beam lithography and focused-ion-beam lithography suffer from high fabrication costs and small fabrication areas. Periodic nanopatterns can be fabricated over large areas using interference lithography and nanosphere lithography, even at wafer-scale[1], [26]. Physical vapor deposition (PVD) of nanoparticles on the other hand emerges as one of the easiest way of fabricating nanoparticles over large areas without using

chemical processes[29], [30]. Thermal evaporation and e-beam evaporation are among the most used PVD methods to fabricate metal nanoparticles[29], [31]. However, the control of physical vapor deposition of nanoparticles lacks order and uniformity due to stochastic nature of nanoparticle formation process[32], [33]. Dewetting of metal films results in nanoparticles during PVD process due to the surface energy difference between the substrate and metal film. Depending on the substrate, the thickness of the metal film, the size of nanoparticles and the interparticle distance change. The size of nanoparticles also differs depending on the deposition rate and the thickness of the metal[30]. Moreover, the post-fabrication processing of metal nanoparticles such as thermal and laser annealing modify the final shape and the interparticle distance of nanoparticles[34], [35]. On the other hand, fabrication of nanoparticles by chemical means gives flexibility to fabricate nanoparticles in low-costs with large amounts with fair size distributions[36]. Nanoparticles can be fabricated in various shapes which further provide different functionalities for specific applications[20].

When nanoparticles are brought together, they start interacting optically[37], [38]. The interaction between nanoparticles can be intuitively understood as the coupling of individual resonators which results a shifted energy spectrum compared to the individual resonators' energies[39]. Due to coupling, plasmonic coupled systems offer a very rich energy spectrum[40], [41]. Since, energy spectrums of coupled structures are broad or multispectral they are desired for various nanophotonics and plasmonic applications. Coupled plasmonic structures are fabricated by either top-down or chemical methods[19], [42]. The aggregating nanoparticles in solutions results another plasmon peak in the red wavelengths which is due coupling of nanoparticles[43]. Scattering spectra of nanoparticles changes drastically when they get close to metallic planes due to hybridization of surface plasmon and localized plasmon modes and resulting gap plasmon modes in between[44]. Gap plasmon modes are also known as metal-insulator-metal (MIM) modes when they are excited between two metal planes. MIM geometry offers rich physics as well as plasmon enhanced applications rooted in classical and quantum electromagnetics[45], [46]. Negative index metamaterials, superlensing, metamaterial absorbers, color printing, photodetectors, plasmonic sensors and surface enhanced spectroscopies are few of the novel applications of MIM based plasmonic structures[22], [47]–[54].

One of the applications of plasmonic surfaces studied here is label-free sensing. Labeled sensing platforms are tagged with fluorescent molecules or quantum dots which are prone to bleaching or deterioration[55], [56]. Label-free sensing strategies are developed to overcome the difficulties that labeled sensing platforms face. Surface plasmon sensors (SPR) are the known as the golden standard for the label-free sensing platforms. Bulk prism based SPR systems are among the widely used plasmonic sensing platforms to probe bio-molecular binding events. Various sensing platforms have been developed on nanoparticles, gratings and plasmonic metamaterials utilizing top-down and bottom-up fabrication methods. Spectroscopic methods combined with plasmonic structures offer another route for label-free sensing methods. Surface enhanced Raman spectroscopy (SERS) provides vibrational information and molecular signatures of molecular moieties[57]–[59]. Typically, Raman spectroscopy requires large amount of molecules to probe molecules due to low probability of release of a Raman scattered photon. When, a monochromatic light (typically laser light) interacts with molecules' vibrational modes, scattered photons have either higher energy (Anti-Stokes) or lower energy (Stokes) than the excitation source. Anti-stokes signals are generally filtered out from the Raman spectra due to their low intensities. Since Raman signal scales with $E = |E_0|^4$, enhancing electromagnetic field intensity near the probe molecules increases the Raman signal enormously. In SERS enhancing electromagnetic field intensity by utilizing nanostructured metal surfaces enhances the Raman signal 4-10 orders of magnitude, thus enabling the possibility of detecting single molecules. On the other hand, debate on the origin of single molecule Raman events is still unresolved. The charge transfer between the metal and molecules might lead to the single molecule Raman events. This mechanism is also known as chemical enhancement factor. SERS platforms should provide electromagnetic field enhancement at the excitation and Stoke's wavelengths. Double resonant nanoantennas, metamaterials and plasmonic gratings are good examples for good SERS platforms where each resonance is accompanied with field enhancement[25], [60], [61]. Broadband plasmonic surfaces are desired as SERS substrates whose resonances span all the vibrational bands of a molecule.

Infrared absorption spectroscopy is a well established label-free tool used in biological and chemical sciences to identify molecular moieties by utilizing specific molecular vibrational bands in the infrared wavelengths[62]. Since the selection rules

in IR and Raman spectroscopy are different, the vibrational information of these techniques is complementary[63]. However, the absorption efficiencies of molecules for specific bands are low in the IR which limits the use of IR spectroscopy for small amount of molecules, molecular or protein monolayers. Different techniques are developed in the IR to identify molecules in small amounts. Attenuated total reflectance (ATR), infrared reflection absorption spectroscopy (IR-RAS) are two widely used tools to identify molecules[64], [65]. In ATR, electromagnetic field decays exponentially when light is sent through a high index prism to a low index medium. The enhanced field at the prism medium interface is used to increase absorption of molecules. Similar to ATR, electromagnetic field is enhanced when a p-polarized light is sent to a substrate at oblique incidences on which molecules are deposited. Metal nanoparticles and deterministically designed plasmonic metal nanostructures emerge as an alternative tool to detect minute amount of molecules[58], [66], [67]. The electromagnetic field is highly enhanced and concentrated around nanoparticles which results in the enhancement of the absorption of the molecules in close proximity. The absorption of the molecules is sensed in the far field signal (reflection/transmission spectrum). This powerful technique is also known as surface enhanced infrared absorption spectroscopy (SEIRA). However, there are some limitations to SEIRA. Vibrational bands of molecules are embedded in plasmonic resonance background in the farfield reflection spectra and data post processing is required to extract positions of vibrational bands. All of the vibrational bands cannot be detected because the electromagnetic field cannot be enhanced over very large bandwidths (3-20μm band) using single resonant plasmonic structures. Moreover, the positions and shapes of vibrational modes are modified due to strong coupling between plasmonic resonances and vibrational modes. Although electromagnetic field enhancement is on the order of 10^3-10^5 signal intensities suffer from low vibrational intensities (~1-5%). Therefore, field enhancements with high mode volumes are preferred over highly localized field enhancements.

Energy harvesting is another application area that plasmonics studies target. Plasmon enhanced photovoltaics is emerged as alternative to current solar cell technologies by either incorporating metallic nanophotonics structures to thin films or silicon solar cells or providing novel solar cell designs[13], [49], [68]–[71]. Most efforts to utilize plasmons in solar cells are based on enhancing electromagnetic field

and increasing the absorption in semiconductor films to decrease the costs and thicknesses. Despite the huge amount of literature, the success of plasmons in photovoltaics area is debatable[72]. Still, the plasmonics promise a bright future for silicon photonics industry for the IR regime[8]. Structuring Schottky contacts with plasmonic structures enabled to use of silicon in photodetectors in the IR wavelengths with lower energy than silicon bandgap. Generation and capture of hot-electrons are the main mechanism for photodetection in these devices. In a Schottky diode, due to band alignment between metal and semiconductor layer, there is a band offset that is smaller than the band gap of the semiconductor. When light is absorbed by the metal contact, electrons are generated, which are either thermalizes or contribute to current through tunneling or hopping above the barrier. The electrons that have energy higher than the band offset are called hot-electrons. However, due to reflective nature of metals the most of the incident light is reflected, thus the generation rate of hot electrons is small. By patterning Schottky contacts, hot-electron generation can be increased due to plasmon enhanced electromagnetic field[8], [14]. MIM resonators emerge as one of the novel hot electron photodetection devices[52], [73]. Similar to Schottky based hot-electron devices, by patterning the metal contacts plasmons are employed to increase hot-electron generation rate. Since these devices utilize high bandgap insulators between two metal contacts, the photoresponsivities are small compared to Schottky based hot electron devices.

Perfect absorption of light is important for aforementioned and can be obtained using patterned metallic surfaces through exciting plasmons. On the other hand, strong interference coatings offer an easier way for perfect light absorption by using ultrathin absorbing semiconducting films[74], [75]. When a thin dielectric film is deposited on a metal surface, resonant light absorption occurs at thicknesses; $t \cong \lambda/4\mathrm{n}$, where n is the dielectric constant and λ is the resonance wavelength. If the dielectric constant increases the resonance thickness becomes $t < \lambda/4\mathrm{n}$ due to increased nontrivial phase at metal dielectric interface. If the dielectric film has a non-zero extinction coefficient ($n = \tilde{n} + i\tilde{k}$), the thickness decreases to $t \ll \lambda/4\mathrm{n}$ and depending on the refractive index function of metal and dielectric resonance thickness changes. Non-zero extinction coefficient results small phase accumulation at oblique angles and the absorption becomes wide-angle. Since these types of coatings exhibit distinct colors depending on the resonance wavelength, most of the

applications concentrate on reflective type color filters[74]–[78]. Light absorption on these coatings can be exploited as novel photodetectors.

In this thesis, we first develop a circuit model to understand the coupling mechanism of a coupled system based on MIM geometry. Our findings are supported with experimental results by fabricating and characterizing the proposed structures. These structures are utilized as SERS substrates with unity enhancement over large areas. Fabrication imperfections are exploited to achieve triple band plasmonic absorber geometry due to excitation of three different plasmon modes. Then, following theoretical and analytical study, MIM structures with nanoparticle top layer are fabricated. By optimizing the conditions for nanoparticle formation, large area, wide angle and broadband plasmonic surface are achieved. Single molecule Raman blinking events are observed with these structures using a confocal Raman microscope equipped with cooled CCD spectrometer. Single molecule Raman events are also detected when a mobile phone's camera used instead of cooled CCD spectrometer. To the best of our knowledge this is the first observation of a single molecule Raman blinking event using a cmos camera. Same surfaces are also used as a photodetector to probe hot electrons using a x-ray photoemission spectroscopy (XPS) system. The final part of plasmonic studies includes aluminum based plasmonic surfaces. By exploiting native oxide layer on Al forming during the fabrication processes, we are able to realize plasmonic surfaces in the visible and IR wavelengths. These surfaces are used as SERS and SEIRA platforms simultaneously. To address the issues of plasmonic surfaces such as low signal intensities narrow bandwidth, small surface area and costs, thin film interference coatings are proposed as novel sensing platforms in the infrared and visible wavelengths. These coatings perform better than conventional plasmonic surfaces when they are used as infrared sensing platforms. Similar surfaces are used as colorimetric sensor platforms to sense protein monolayers and bilayers.

Chapter 2

Well-Defined Coupled Plasmonic Structures

Plasmonic metamaterials allow confinement of light to deep subwavelength dimensions, while allowing for the tailoring of dispersion and electromagnetic mode density to enhance specific photonic properties. Optical resonances of plasmonic molecules have been extensively investigated; however, benefits of strong coupling of dimers have been overlooked. In this part, a novel plasmonic geometry and its surface enhanced Raman spectroscopy application are demonstrated. Then, fabrication related issues are exploited for a multispectral metamaterial absorber. Before going into details of this chapter, surface plasmon at different metal dielectric interfaces are studied.

Parts of this chapter were published as;

1. Sencer Ayas, Hasan Guner, Burak Turker, Oner Ekiz, Faruk Dirisaglik ,Ali Kemal Okyay and Aykutlu Dana, "Raman Enhancement on a Broadband Meta-Surface", ***ACS Nano***, **2012**, *6* (8), pp 6852–6861

2. Sencer Ayas, Gokhan Bakan and Aykutlu Dana, "Rounding corners of nano-square patches for multispectral plasmonic metamaterials absorbers" **Optics Express**, Vol. 23, No. 9, 2015

2.1. Surface Plasmons at Metal-dielectric Interface

To understand the coupling conditions, a very simple geometry (metal-dielectric interface) is used to give the basics of surface plasmons [79]. We start with the assumption of evanescently decaying and propagating surface plasmons in the z and x-directions respectively as shown in Figure 2-1.

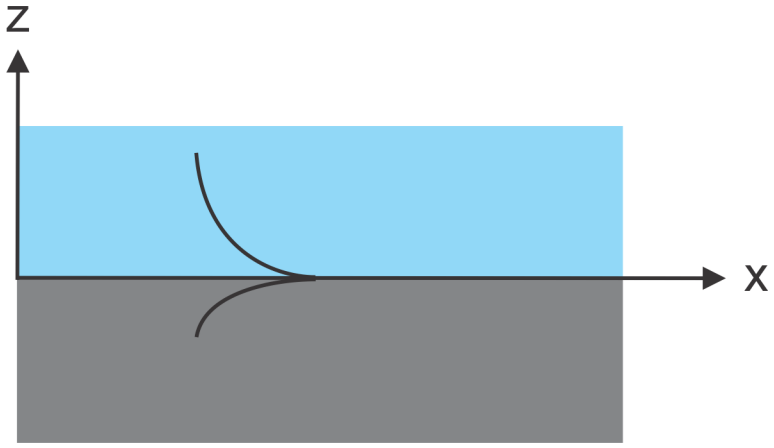

Figure 2-1 Surface plasmon excitation scheme at metal-dielectric interface.

For a TM polarized wave, electric and magnetic fields are given as

$$H_y(z) = Ae^{i\beta x}e^{-k_d z} \tag{2.1}$$

$$E_x(z) = i\frac{Ak_d}{\omega\varepsilon_o\varepsilon_d}e^{i\beta x}e^{-k_d z} \tag{2.2}$$

for z>0 (dielectric region)

$$H_y(z) = Be^{i\beta x}e^{k_m z} \tag{2.3}$$

$$E_x(z) = -i\frac{Bk_m}{\omega\varepsilon_o\varepsilon_m}e^{i\beta x}e^{k_m z} \tag{2.4}$$

for z<0 (metal region).

By equating H_y and E_x at z=0 we obtain A=B and $Ak_d/\varepsilon_d=-Bk_m/\varepsilon_m$. Hence:

$$\frac{k_m}{\varepsilon_m} = -\frac{k_d}{\varepsilon_d} \tag{2.5}$$

Since propagation constants and ε_d are real, surface plasmons are supported for materials at the metal-dielectric interface which have negative dielectric constants. Typically, metals have negative dielectric functions above plasma frequency. Although, plasma frequencies of metals are in the deep-UV regime, some metals have real dielectric functions in the visible portion of the spectrum due to interband transitions. For example, gold (Au) has an interband transition around 500nm which

limits the use of Au in the UV wavelengths. Using $\beta_x^2=k_o^2\varepsilon_{d,m}-(k_{d,m})^2$ and Equation 2.5 together results surface plasmon dispersion relation $\beta_x = k_o\sqrt{\frac{\varepsilon_d\varepsilon_m}{\varepsilon_d+\varepsilon_m}}$. In a similar manner, we can derive the surface plasmon coupling condition for TE polarized waves.

For a TE polarized wave electric and magnetic fields are given as

$$E_y(z) = Ae^{i\beta x}e^{-k_d z} \tag{2.6}$$

$$H_x(z) = i\frac{Ak_d}{\omega\mu}e^{i\beta x}e^{-k_d z} \tag{2.7}$$

for z>0 (dielectric region)

$$E_y(z) = Be^{i\beta x}e^{k_m z} \tag{2.8}$$

$$H_x(z) = -i\frac{Bk_m}{\omega\mu}e^{i\beta x}e^{k_m z} \tag{2.9}$$

for z<0 (metal region).

The continuity equation for E_y and H_x at the metal-dielectric interface (z=0) results in A=B and $Ak_d+ Bk_m=0$ where we obtain the relation $A(k_d+ k_m)=0$. Since $k_{d,m}>0$, A=0 is the only condition for TE mode. Thus, $E_y=0$, $H_x=0$ and the surface plasmons are not supported for TE polarized waves.

So far, a propagating wave at a metal-dielectric interface is assumed to derive surface plasmon dispersion relation. However, excitation of surface plasmons at metal-air interface requires special coupling geometries such as Kretschmann geometry, since the dispersion relation of surface plasmons and photonic dispersion relation do not cross as shown in Figure 2-2. In Kretshcmann geometry, light is coupled through a prism rather than air. Such excitation scheme results on a resonance when the incidence angle is scanned for a certain wavelength as shown in Figure 2-3. Surface plasmon resonance (SPR) sensors are developed by utilizing such resonant characteristic. Moreover, the reflectance spectrum depends on the dielectric environment that surface plasmons are coupled. Biomolecular interactions and binding events can be detected using SPR sensors by probing the reflected light intensity due to the change of dielectric environment close to the metal-dielectric interface during binding events. Small molecules, viruses, protein interactions and bacteria can also be detected using SPR sensors.

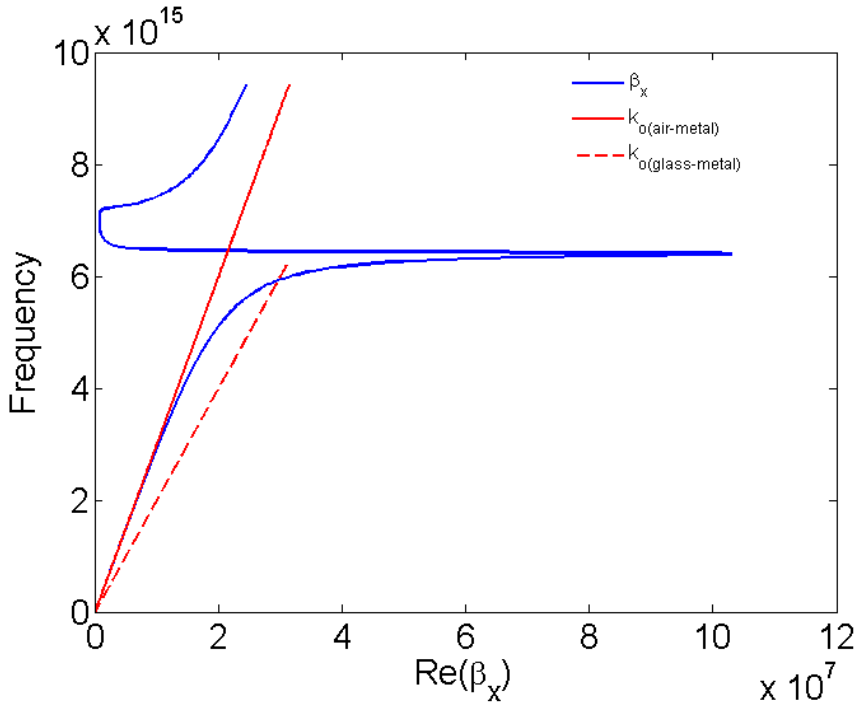

Figure 2-2. Dispersion relation of surface plasmons at metal-air interface (Solid blue curve). Dispersion of photons in air and glass are shown with solid and dashed red curves.

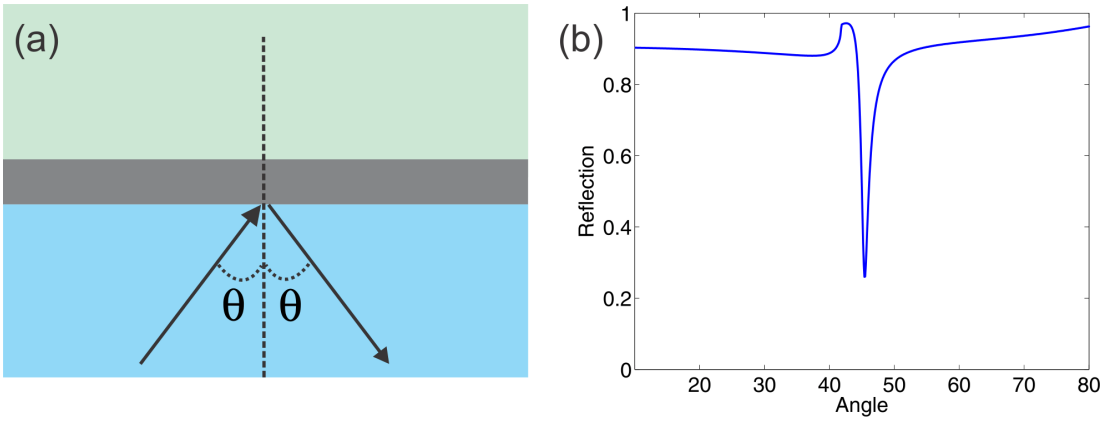

Figure 2-3. Surface plasmon excitation scheme for Kretchmann geometry (a) and angular reflectance spectrum for λ=600nm (b).

2.2. Surface Plasmons in Metal-Insulator-Metal Resonators

Different surface plasmon schemes are proposed for specific applications. Metal-insulator-metal (MIM) resonators are among the widely used geometry in plasmonics and metamaterial applications due to their ease of fabrication and tunability, while controlling surface plasmon propagation by tuning effective refractive index. Since the coupled plasmonic geometry in this study is based on MIM resonators, the general dispersion relations and effective dielectric constants are studied here. The geometry of an MIM resonator is shown in Figure 2-4. The thickness of dielectric layer is d. The metal thicknesses are assumed semi-infinite for top and metal layers.

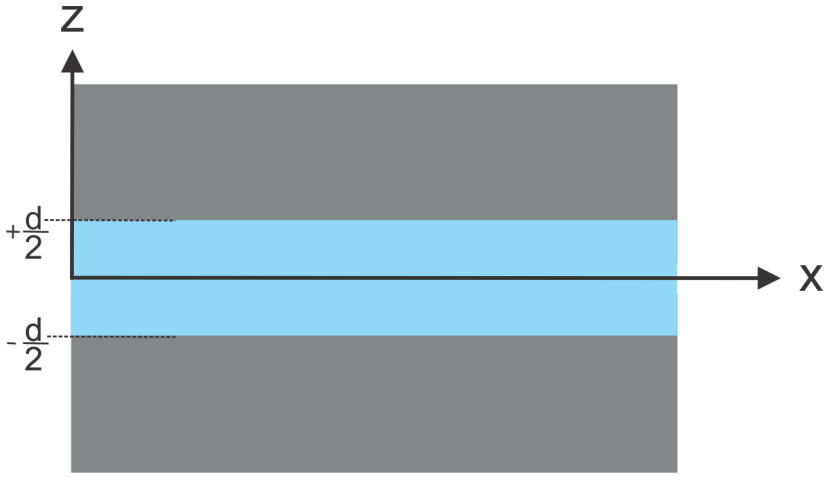

Figure 2-4. Geometry of metal-insulator-metal resonator structure.

The electric and magnetic field profiles in top metal, dielectric and bottom metal regions are given as

$$H_y(z) = Ae^{i\beta x}e^{-k_m z} \tag{2.10}$$

$$E_x(z) = i\frac{Ak_m}{\omega\varepsilon_o\varepsilon_m}e^{i\beta x}e^{-k_m z} \tag{2.11}$$

for z>d/2 (top metal region).

$$H_y(z) = Be^{i\beta x}e^{k_m z} \tag{2.12}$$

$$E_x(z) = -i\frac{Bk_m}{\omega\varepsilon_o\varepsilon_m}e^{i\beta x}e^{k_m z} \tag{2.13}$$

for z<-d/2 (bottom metal region).

$$H_y(z) = Ce^{i\beta x}e^{-k_d z} + De^{i\beta x}e^{k_d z} \tag{2.14}$$

$$E_x(z) = i\frac{Ck_d}{\omega\varepsilon_o\varepsilon_d}e^{i\beta x}e^{-k_d z} - i\frac{Dk_d}{\omega\varepsilon_o\varepsilon_d}e^{i\beta x}e^{k_d z} \tag{2.15}$$

for d/2<z<-d/2 (dielectric region).

The continuity of H_y and E_x at z=-d/2 and z=d/2 results in

$$Ae^{-k_m d/2} = Ce^{\frac{-k_d d}{2}} + De^{\frac{k_d d}{2}} \tag{2.16}$$

$$A\frac{k_m}{\varepsilon_m}e^{-k_m d/2} = \frac{k_d}{\varepsilon_d}Ce^{\frac{-k_d d}{2}} - \frac{k_d}{\varepsilon_d}De^{\frac{k_d d}{2}} \tag{2.17}$$

$$Be^{-k_m d/2} = Ce^{\frac{k_d d}{2}} + De^{\frac{-k_d d}{2}} \tag{2.18}$$

$$-B\frac{k_m}{\varepsilon_m}e^{-k_m d/2} = \frac{k_d}{\varepsilon_d}Ce^{\frac{k_d d}{2}} - \frac{k_d}{\varepsilon_d}De^{\frac{-k_d d}{2}} \tag{2.19}$$

After eliminating A and B using Equations 2.16-17 and 2.18-19 respectively, we obtain

$$\left(1 - \frac{\varepsilon_m}{k_m}\frac{k_d}{\varepsilon_d}\right)Ce^{\frac{-k_d d}{2}} = (1 + \frac{\varepsilon_m}{k_m}\frac{k_d}{\varepsilon_d})De^{\frac{k_d d}{2}} \tag{2.20}$$

$$\left(1 + \frac{\varepsilon_m}{k_m}\frac{k_d}{\varepsilon_d}\right)Ce^{\frac{k_d d}{2}} = (1 - \frac{\varepsilon_m}{k_m}\frac{k_d}{\varepsilon_d})De^{\frac{-k_d d}{2}} \tag{2.21}$$

If we multiply both sides of Equations 2.20 and 2.21, $C = \pm D$ is achieved. Then Equation 2.20 separates into two equations as follows

$$\left(1 - \frac{\varepsilon_m}{k_m}\frac{k_d}{\varepsilon_d}\right)e^{\frac{-k_d d}{2}} - \left(1 + \frac{\varepsilon_m}{k_m}\frac{k_d}{\varepsilon_d}\right)e^{\frac{k_d d}{2}} = 0 \tag{2.22}$$

$$\left(1 - \frac{\varepsilon_m}{k_m}\frac{k_d}{\varepsilon_d}\right)e^{\frac{-k_d d}{2}} + \left(1 + \frac{\varepsilon_m}{k_m}\frac{k_d}{\varepsilon_d}\right)e^{\frac{k_d d}{2}} = 0 \tag{2.23}$$

Equations 2.22 and 2.23 result in two distinct solutions which are

$$\tanh(\frac{k_d d}{2}) = -\frac{\varepsilon_m}{k_m}\frac{k_d}{\varepsilon_d} \tag{2.24}$$

$$\tanh(\frac{k_d d}{2}) = -\frac{\varepsilon_d}{k_d}\frac{k_m}{\varepsilon_m} \tag{2.25}$$

Different parameters can be extracted from Equations 2.24 and 2.25 such as effective refractive index and propagation length which are important parameters for plasmonic waveguide applications. Effective refractive index parameter can be extracted using Equations 2.24-25 and $\beta_x^2 = k_o^2\varepsilon_{d,m} - (k_{d,m})^2$ where $\beta_x = k_o n_{eff}$.

2.3. Raman Enhancement on a Broadband Meta-surface

2.3.1. Introduction

Plasmonic excitations of metallic nanostructures have attracted a great deal of attention in the past decades, due to the rich variety of geometric configurations, the associated optical properties and phenomena, and the wide range of present and potential future applications[18], [80]. Propagating and localized plasmons have been utilized in the design of photonic structures to efficiently couple free-space propagating light onto highly confined surface modes, resulting in the enhancement of electromagnetic field intensities[81], [82]. Nonlinear optical effects benefit from plasmonic field enhancement[81], and plasmonics have the potential to be an enabling technology for quantum optics and all-optical information processing[83], [84]. It has been shown that plasmonic field enhancement allows the observation of Raman scattering from single molecules with low excitation powers down to microwatts[85], [86]. The lack of reliability resulting from the spatially non-uniform nature of plasmonic field enhancement can be a problem for applications requiring repeatability. In the case of surface-enhanced Raman scattering (SERS), regions with high enhancement (so-called hot spots) are typically major contributors to the observed signal. Raman intensity enhancement is estimated through $I_{SERS} \cong I_0|E(\omega_{exc})E(\omega_{det})/E_0(\omega_{exc})E_0(\omega_{det})|^2$, where ω_{exc} and ω_{det} are the excitation and detection frequencies, and E and E_0 are the electric field intensities with and without the presence of plasmonic structures. Defining an enhancement factor, $EF(\omega) = |E(\omega)/E_0(\omega)|^2$, overall Raman enhancement factor can be written as the product of excitation and detection factors, $EF_{SERS} = EF(\omega_{exc})EF(\omega_{det})$. Spatial non-uniformity of the electric field directly translates into a spatial non-uniformity of EF_{SERS} and can be an important disadvantage for repeatability. Hot spots are typically formed when two metal regions come close (within a few nanometers) to each other, and even periodic structures may display a wide distribution of enhancement factors[87]. In order to achieve high and spatially uniform field enhancement, engineered surfaces that exhibit plasmon modes at both the excitation and scattering wavelengths are needed[53], [60], [88], [89]. Previously, metal nanoparticle clusters (bottom-up approach) and sparse structures or biharmonic gratings with double resonances (top-down approach) were used for this purpose[90].

Bottom-up approach substrates offer the advantage of simplicity and offer uniformity over large scales; on the other hand, the statistical nature of production processes, in principle, prevents completely hot-spot-free and uniform enhancement on a microscopic scale. Sparse arrays of multiply sized nanoantennas, or multiperiodic structures, may be designed to enhance fields at both excitation and scattering frequencies, however, exhibit spatially non-uniform spectral properties over the extent of a wavelength. In contrast, plasmonic meta-materials possess subwavelength periodicity. When fabricated using a top-down approach, they have the potential to offer spatially uniform, wide band coupling required for uniform Raman enhancement. In this part of the thesis, we discuss the application of plasmonic meta-surfaces to SERS. We describe the resonances and field enhancements of a closely packed metal–insulator–metal configuration, which we refer to as multiply coupled plasmonic meta-material (MCPM). Strong coupling of the modes is shown to be effective for a subset of geometric parameters. Despite the seemingly common and simple geometry, we show that, under strong coupling of various types of modes, a rich band structure can be engineered within a wide spectral range, allowing highly controllable field enhancement at excitation and scattering frequencies, thereby allowing highly repeatable SERS.

2.3.2. Description of the Plasmonic Meta-Surface

A cross-sectional schematic of the one-dimensional periodic MIM structure is shown in Figure 2-5a (a representative SEM micrograph is given in Figure 2-5b). MIM elements with relatively thick top metal layers (d≥50 nm), with widths of 150–200 nm, are repeated with periods of 200 to 300 nm, forming an inter-MIM spacing of 10–80 nm. MIM structures can be viewed as nanoscale planar waveguides[91], and individual MIM elements have modes confined inside the dielectric region (referred to as *waveguide mode*). Localized resonances result from the Fabry–Perot (FP)-type resonator formed within the MIM waveguide, terminated at both ends. The propagation wavevector β_{SPP} and effective index $n_{eff} = \beta_{SPP}/k_0$ of the fundamental TM mode of a MIM waveguide can be calculated by solving for β_{SPP} in the following equation $k_m\varepsilon_d + k_d\varepsilon_m \tanh(\frac{k_d w}{2}) = 0$ here $k_d = (\beta_{SPP}^2 - \varepsilon_d k_0^2)^{1/2}$, $k_m = (\beta_{SPP}^2 - \varepsilon_m k_0^2)^{1/2}$, and $k_0 = 2\pi/\lambda$ is the propagation wave vector in free space for wavelength λ which is also given by Equation 2.25. Typically, β_{SPP} is a complex number, and the

real part of β_{SPP} can be used to infer the effective wavelength. Assuming a unity relative magnetic permeability for propagating TM modes inside the MIM waveguide, the effective index (n_{eff}) can also be used to estimate the impedance of the transmission line, $Z_{MIM} = 120\pi/n_{eff}$ (see Figure 2-5c). The propagation constant can be used to estimate the resonances of a FP cavity. The roundtrip phase is written as $\varphi(\lambda) = 2\beta_{SPP}w + 2\Delta\varphi(\lambda)$, where $2\beta_{SPP}w$ is the phase shift due to propagation, and $2\Delta\varphi(\lambda)$ is the total phase shift acquired upon reflection at the ends of the resonator. A FP resonator exhibits resonances when $|1 - R_0 \exp i\varphi(\lambda)|$ is a minimum, where R_0 is the magnitude of the reflection coefficient. Using the above formulation, absorption resonances of uncoupled MIM waveguides have been calculated. In general, $\Delta\varphi(\lambda)$ may be calculated through the reflection coefficient at the end of the waveguide, taking into account the impedance mismatch between the waveguide mode and free-space modes[92].

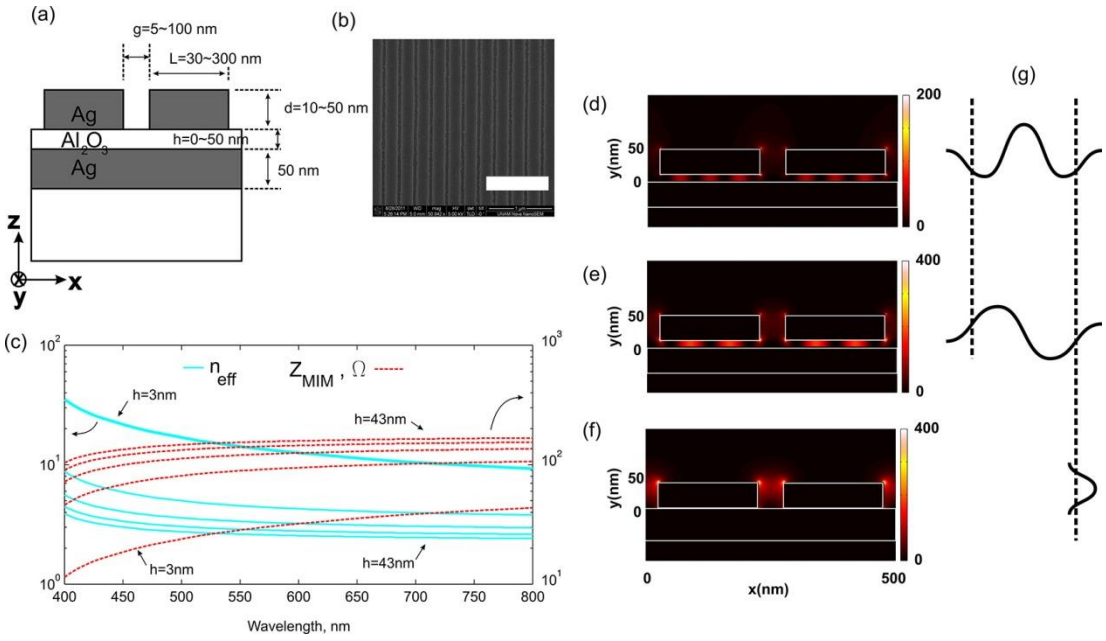

Figure 2-5. (a) Schematic cross section of metal–insulator–metal (MIM) meta-material structures. The metal layers are evaporated Ag, and the dielectric layer (0–40 nm thick) is Al_2O_3 deposited. (b) Scanning electron micrograph of a representative structure is shown; scale bar 1 μm. (c) Effective index (n_{eff}) and impedance (Z_{MIM}) of the MIM fundamental TM mode as a function of wavelength for various dielectric layer thicknesses (3, 13, 23, 33, and 43 nm) are given for convenience. (d) Depending on the frequency of excitation, different resonant modes can be excited within the MIM section. In the one-dimensional case, the MIM can be viewed as a transmission line, whose propagation constant (or effective index) depends on the gap between the top and bottom metal layers. Truncation at both ends results in a Fabry–Perot (FP)-type resonator. Electric field intensity squared is plotted for a 200 nm long MIM structure with 10 nm dielectric gap excited at 555 nm, corresponding to a resonance of the FP resonator. (e) When the same structure is excited at 660 nm, another resonance is excited displaying a different field distribution. (f) When the gap is reduced to

zero, one resonant mode persists in the vertical transmission line cavity formed with side walls of the top metal layer as conducting planes. (g) Cartoons show the field amplitudes of modes shown in (d, e, and f).

Optical properties of arbitrary metallic nanostructures have been commonly analyzed using optical first-principles calculations. Optical properties of simple geometric configurations, on the other hand, can be explained in terms of lumped circuit elements[93]–[97]. The waveguide perspective is practically adequate, as the experimentally observed optical properties of isolated structures can be well explained using this approach[98]. Figure 2-5d,e shows the electric field profiles when such structures are excited at two different wavelengths for a dielectric thickness of 12 nm. Standing wave patterns within the MIM are observed when the surface is excited near its resonances, validating the FP resonator approach (cartoons in Figure 2-5g show E-field along the structure for various modes in Figure 2-5d–f).

In the one-dimensional case, when the dielectric thickness is reduced to zero, the MIM waveguide modes disappear; however, the remaining structure still exhibits a localized mode (Figure 2-5f). This remaining vertical cavity mode (referred to as LFP, short for localized Fabry–Perot) is formed due to FP-type resonance in the vertical metallic cavity between the top metal layers of consecutive MIM regions[94]. The resonance frequency of the LFP can be approximately calculated using lumped models or using the waveguide approach used above. The fundamental resonance of closely spaced MIM structures also have been modeled previously using lumped LC elements[94], [99]. Using such a model, the LFP mode frequency can be approximated by $\omega_{LFP} = ((C_e + C_m + (C_m^2 + C_e^2)^{1/2})/(LC_mC_e))^{1/2}$, where $L \cong 0.5\ \mu hw + 3w/(2\varepsilon_O hw_P^2)$ is the inductance per unit width (μ is the magnetic permeability, h is the dielectric thickness, and w is the width of the MIM), $C_e \cong c\varepsilon_O h/g$ is the capacitance per unit width due to coupling between MIM top metals (ε is the dielectric constant, h is the dielectric thickness, g is the gap between MIMs, and c is a correction parameter), $C_m \cong 0.25\varepsilon_O\varepsilon h/g$ is the capacitance per unit width due to coupling of top metal layer of MIMs to the metallic ground plane. The model ignores resistive losses.When the areal density of such structures is increased to improve surface coverage, strong coupling of individual structures becomes inevitable, modifying the spectral properties, as well as the band structure.

2.3.3. Coupled Meta-Atoms and Meta-Molecules

The LFP mode can be considered as a light meta-atom, possessing a single energy level (Figure 2-6a). Similarly, the MIM structure constitutes a heavy meta-atom, with more than one energy level (Figure 2-6b). When the atoms are brought into contact by a coupling mechanism, bands emerge similar to the coupled resonator optical waveguide (CROW)[100] A periodic arrangement of grooves (*i.e.*, LFPs) results in a monatomic crystal (Figure 2-6c). In the monatomic case, coupling is primarily through the surface plasmon mode (SPP). Collective excitations in nanoparticle arrays have been previously reported, and for large interparticle spacing, weak coupling occurs through radiative routes[101]–[103]. On the other hand, when MIMs are arranged in a closely packed periodic fashion, MIM modes and the LFP modes strongly couple due to overlapping modes, rather than due to radiative coupling, resulting in a diatomic crystal (Figure 2-6d). The coupled MIM waveguides could also be viewed to be similar to a resonant guided wave network (RGWN)[104]; however, coupling of waveguides through an intermediate localized resonance in the vertical cavity distinguishes the MCMP from the RGWN. The coupling of the MIM and LFP modes results in an anticrossing behavior, as shown in Figure 2-6e, f. In numerical calculations, it is seen that anti-crossing-over behavior due to coupling of MIM modes with the LFP (around $h \sim 17$ nm in Figure 2-6e, f) leads to an improvement of the absorption bandwidth.

The angular dependence of coupling to the resonances is best visualized in the band structure of the plasmonic meta-surface. In order to intuitively understand the dependence of the band structure on design parameters, we construct a circuit model, as shown in Figure 2-6g. The MIM section is modeled using a transmission line, and the LFP is modeled using an LC resonator. A capacitor is used to model the coupling. The one-dimensional band structure is calculated by constructing an ABCD matrix for the lumped element model of the unit cell. In order to obtain the band structure, the ratio of the input and output parameters of the ABCD matrix are assumed to be $\exp(ik\Lambda)$ for a given propagation vector k and period Λ. In order to find the resonance frequencies, one needs to solve for ω through

$$\left| I - \begin{bmatrix} A & B \\ C & D \end{bmatrix} e^{ik\Lambda} \right| = 0 \tag{2.26}$$

where I is the 2×2 identity matrix.

The ABCD matrix of the unit cell is constructed by multiplying ABCD matrices for the transmission line representing the MIM section with ABCD matrices for the lumped elements for coupling and LFP sections of the model. Resistive or radiative losses are ignored in the model. The ABCD matrix for the transmission line section is given by

$$ABCD_{\mathrm{TL}} = \begin{bmatrix} \cos(\beta l) & jz_o \sin(\beta l) \\ jz_o \sin(\beta l) & \cos(\beta l) \end{bmatrix} \tag{2.27}$$

The coupling capacitor has an impedance of $X_c = 1/(j\omega C_{\mathrm{coupling}})$. The ABCD matrix for the coupling capacitor is given by

$$ABCD_{\mathrm{coupling}} = \begin{bmatrix} 1 & X_c \\ 0 & 1 \end{bmatrix} \tag{2.28}$$

The parallel LC resonator representing the localized Fabry–Perot (LFP) mode has an impedance X_{LFP} given by $X_{\mathrm{LFP}} = 1/(1/(j\omega L_{\mathrm{FP}}) + j\omega C_{\mathrm{FP}})$. The ABCD matrix for the LC resonator representing the mode is given as

$$ABCD_{\mathrm{LFP}} = \begin{bmatrix} 1 & 0 \\ 1/X_{LFP} & 1 \end{bmatrix} \tag{2.29}$$

The ABCD matrix for the unit cell, $ABCD_{\mathrm{uc}}$, is calculated by multiplying the matrices in correct order, $ABCD_{\mathrm{uc}} = ABCD_{\mathrm{TL}} \times ABCD_{\mathrm{coupling}} \times ABCD_{\mathrm{LFP}} \times ABCD_{\mathrm{coupling}}$. The resonance frequencies calculated by the matrix method are shown on top of numerical results in Figure 2-6e,f. The model correctly captures the essential features of the numerical results, such as mode frequencies and anticrossing behavior.

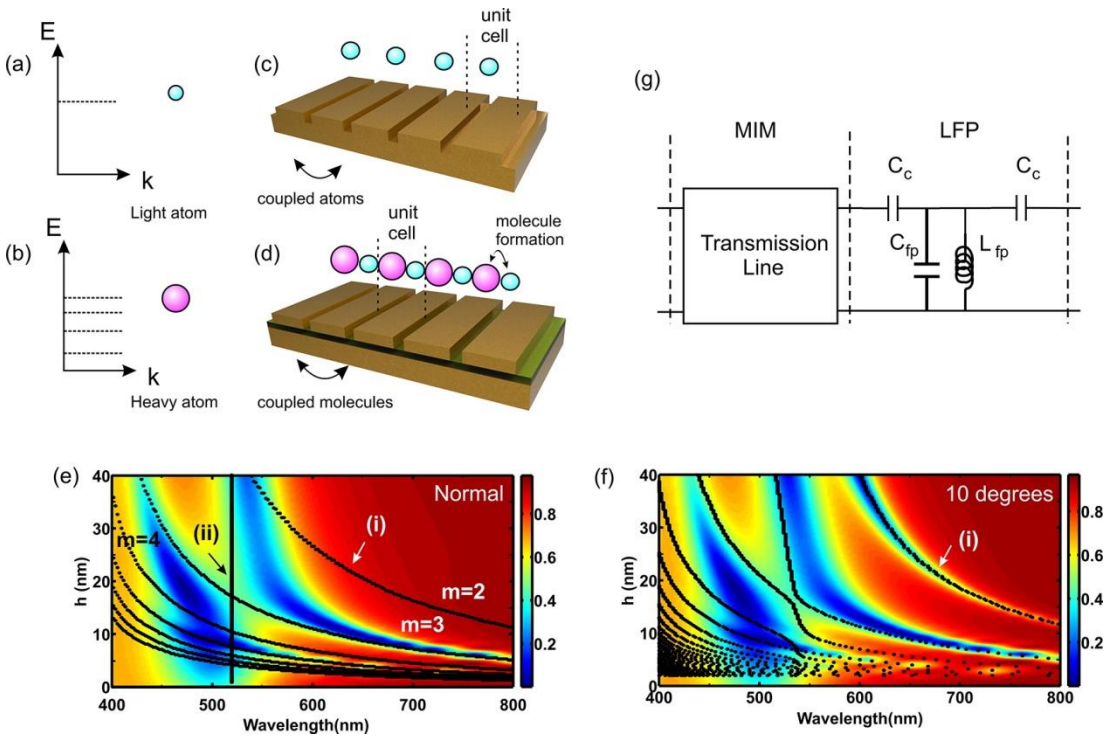

Figure 2-6. (a) Cavity resonance (LFP) can be thought as corresponding to a light atom, with a single localized state, and (b) MIM can be thought as corresponding to a heavy atom, with a multiple localized states. (c) In a one-dimensional periodic arrangement of the light atoms, coupling through the surface plasmon mode can introduce a coupling of the LFPs and propagating bands can be formed. (d) Similarly, in a one-dimensional periodic arrangement of the MIM structures with a relatively thick top metal and a thin gap dielectric, the MIM modes and the LFP mode formed between consecutive MIMs are hybridized to form a diatomic molecule. The molecules are coupled to form the band structure of the diatomic crystal. (e) Effect of mode coupling is observed in the reflection coefficient, plotted as a function of wavelength and dielectric thickness, *h*, for a one-dimensional crystal. Numerical computation results are shown for a 250 nm period structure with 180 nm MIM width, for normal incidence. Resonance wavelengths are calculated using the Fabry–Perot resonator model for the MIM structures (black lines; see text for details) that are superimposed. Antisymmetric modes (even mode number *m*) are not coupled to the free-space modes at normal incidence and, therefore, contribute no absorption (arrow (i)). The LFP mode wavelength is estimated using the LC model (vertical line around 520 nm, denoted by arrow (ii)). (f) Reflection coefficient is plotted as a function of wavelength and dielectric thickness *h* at a 10° angle of incidence. Due to the broken symmetry, even modes also contribute to absorption. (g) Lumped circuit model for the diatomic unit cell consists of a transmission line capacitively coupled to a localized LC resonator representing the LFP mode. The model is used to calculate the resonance frequencies of the modes, plotted as dots, on top of the computational results in (f). The model captures the essential features of numerical calculations such as the resonance frequencies and anticrossing behavior due to coupling of modes.

In order to illustrate the effect of geometric parameters on the optical resonances and show the quasi-omni-directional nature of the MCPM, we calculate the bands of several structures, as shown in Figure 2-7a–e. The monatomic crystal (no dielectric) is essentially a lamellar grating (cavity depth 50 nm, width 50 nm, period 250 nm), and the LFP mode couples through the SPP to form a CROW-like band (Figure 2-7a). As the dielectric gap is introduced, MIM modes emerge in the reflection spectrum. For a thin dielectric of h = 3 nm, a large number of modes that span the visible spectrum emerge (Figure 2-7b). Consecutive bands with odd and even MIM modes show improved absorption at low and high angles due to their symmetry (a similar observation was reported for MIM resonator arrays in the terahertz frequency range[92]. The band structure, which is calculated by solving Equation 2.26, displays bands that coincide with reflection minima seen in numerical calculations. As the gap is increased to 12 nm (Figure 2-7c–e), the number of bands is reduced. The effect of the surface plasmon mode becomes visible at high frequencies and is included in band structure calculations as a perturbation. The coupling of the SPP to the MIM/LFP structure has the effect of pushing and concentrating the bands to around 500 nm at high angles ($k\Lambda/\pi \sim 1$) in Figure 2-7a–e.

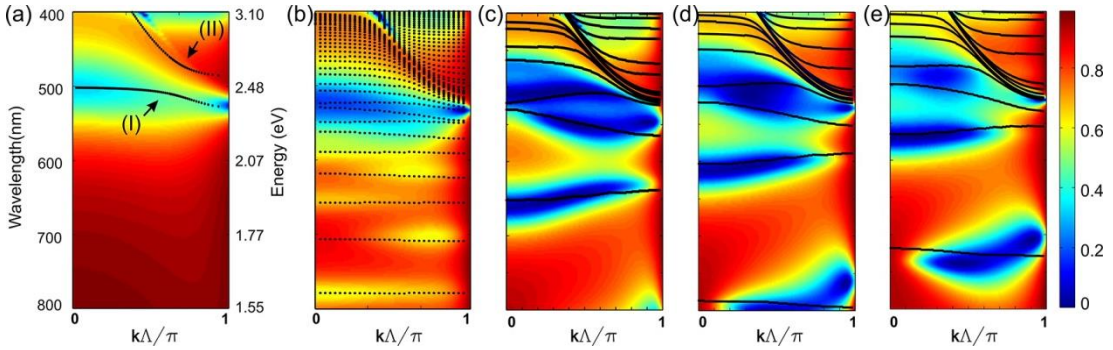

Figure 2-7. (a) Band structure of a monatomic meta-surface is calculated using the circuit model in Figure 2g and the ABCD matrix approach and superimposed on the reflection obtained through numerical calculations. When the dielectric thickness is zero, only the bands formed are through coupling of the LFP (arrow I) modes via the surface plasmon mode (arrow II) are observed. (b) Increasing the gap to 3 nm results in the appearance of a large number of MIM modes and formation of a diatomic meta-surface. (c) Increasing the gap to 13 nm results in a reduction of the number of MIM modes, while increasing the absorption in the coupled bands due to improved impedance matching of the surface with free-space propagating modes. Further band structures are shown in (d) and (e) for 180 and 160 nm MIM widths, with 250 nm period. Color bar shows corresponding reflectance values.

2.3.4. Experimental Results

The absorption spectra of the surfaces have been recorded at normal incidence using a low numerical aperture (NA = 0.05) objective for both illumination and light collection. The reflection spectra are seen to agree with simulation results for various MIM widths and periods (Figure 2-8a, b). Evidence for the quasi-omni-directional character of the one-dimensional structures can be seen in the high spatial resolution reflection maps shown in Figure 2-8c (average reflectance for a 10 nm spectral band centered at 550 nm is shown). When the structures are imaged by different numerical aperture lenses (objectives with 20×, 50×, and 100× magnification and respective numerical apertures of 0.4, 0.7, and 0.95), the absorption is seen to be quite independent of the numerical aperture. This is in accordance with the expected quasi-omni-directional character of the band structures around 550 nm.

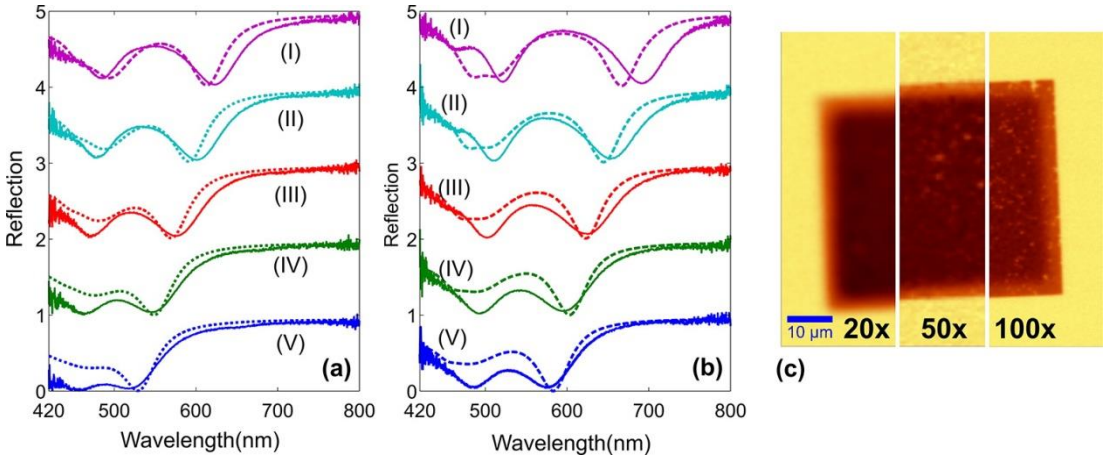

Figure 2-8. Theoretical and experimental reflectance plotted as a function of wavelength at normal incidence for (a) one-dimensional, 250 nm period structures with nanowire widths of 180 nm (I), 170 nm (II), 160 nm (III), 150 nm (IV), 140 nm (V) and (b) one-dimensional, 300 nm period structures with nanowire widths of 200 nm (I), 190 nm (II), 180 nm (III), 170 nm (IV), 160 nm (V). (c) TM mode reflectance for a 10 nm band around 550 nm observed with different numerical apertures (20×, 50×, and 100× objectives) on one-dimensional 250 nm period 150 nm width structures. Insensitivity to numerical aperture demonstrates the quasi-omni-directional absorption of the surfaces.

For most applications in sensing and spectroscopy, the locations with high field enhancements must be exposed to allow for adsorption of molecules. Such regions are present in the MCPM (LFP region and top surface), where the enhancement can be utilized for sensing or Raman spectroscopy. It should be noted that absorption and field enhancement are not necessarily proportional. However, numerical calculations show that if the resistive losses can be ignored, there is a strong correlation between the absorption and field enhancement. Typically, this is the case when the excitation

frequency is reasonably below the plasma frequency of the metal and absorption is enhanced primarily due to plasmonic resonances. In our wavelength range of interest (400 nm to NIR), dielectric constant of silver allows this approximation. The MCPM can feature multiple absorption bands (and correlated field enhancement) that cover the entire excitation and scattering wavelengths (for example 250 period, 50 nm top metal, 12 nm dielectric thickness, and 200 nm top metal width). The advantage of the MCPM structures in plasmon-enhanced Raman spectroscopy is demonstrated using Cresyl Violet dye as the example molecule. Using low powers of about 100–300 μW (measured by a placing a photodiode at the sample location in a separate measurement), the Raman spectra are recorded at various locations on the unpatterned MIM substrate (Figure 2-9a, arrow III) and on the MCMP (Figure 2-9a, arrows I and II). The unpatterned MIM reference produces little observable Raman or fluorescence signal, whereas the MCPM produces a pronounced enhancement, which is theoretically estimated to be on the order of 5×10^5 to 10^6. The TM polarized reflectance (10 nm band around 550 nm, Figure 2-8a) has a slightly non-uniform spectral response over a distance of about 50 μm, attributed to the exposure nonuniformity during the e-beam lithography. Raman signal map (591 cm^{-1} peak) collected at the same location is shown in Figure 2-9b. A spatial non-uniformity is also seen in the Raman signal (Figure 2-9b), correlated with the reflectance non-uniformity (Figure 2-9a). As expected, enhancement of the Raman signal is proportional to the absorption within the Raman band wavelength range (Figure 2-9c,d). When a longer averaging time of 22 s is used, still the Raman signal is absent on a flat Ag reference surface for the low power level used (Figure 2-9e). The fabrication related non-uniformity is insignificant over smaller length scales, and we superimpose the Raman spectra collected from 1600 locations within a 10 μm × 10 μm square region in Figure 2-10a. The fluorescence and Raman enhancements are uniformly enhanced (about 10% for fluorescence and about 20% for Raman) over the region, as is seen in the histograms (Figure 2-10b) shown for two wavelengths. When the Raman signal is represented as an image map, several defects with submicrometer diameters are clearly resolved as dark spots in the image (Figure 2-10c), indicating true high-resolution imaging capability using the MCPM (image contrast is enhanced to clarify the dark spots).

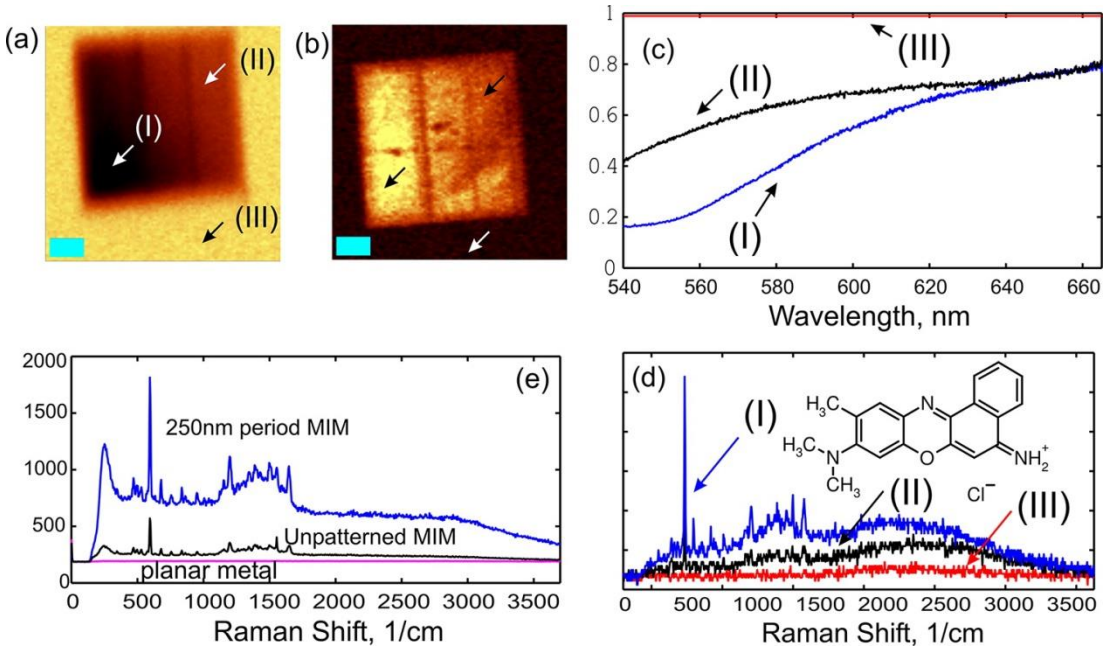

Figure 2-9. (a) Reflectance map (540–600 nm band) acquired using a 20× objective (NA 0.4) on a 250 nm period structure with 200 nm MIM width. (b) Raman spectra map (intensity of 591 cm–1 band, collected with 100 μW excitation power at 532 nm, 20× objective, 100 ms dwell time per pixel) of Cresyl Violet monolayer on the same structure. Scale bar is 10 μm. (c) Reflectance as a function of wavelength for several locations and (d) corresponding Raman spectra. Reflectance is plotted at two different locations (I) and (II) as referenced to location (III). Due to non-uniformity of the fabrication process, a gradient of the resonance wavelength is observed from top-right position to bottom-left position. When the absorption overlaps with excitation and emission wavelengths, improved Raman scattering is observed. Inset shows chemical structure of Cresyl Violet. (e) Raman signal is collected using a longer integration time (22 s, 100 μW excitation power) on a planar silver surface, unpatterned MIM, and 250 nm period MIM regions. Although Cresyl Violet exhibits no Raman signal on the plane metal surface, some enhancement is seen on unpatterned MIM regions, possibly due to the surface roughness of the top layer.

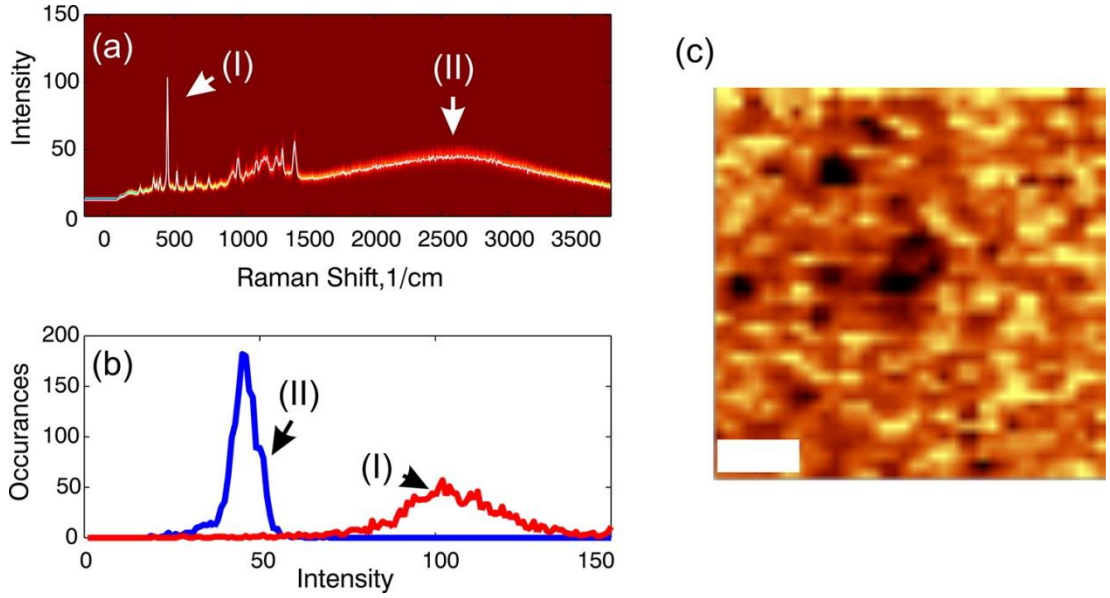

Figure 2-10. (a) Superimposed Raman spectra collected from 1600 individual spots over an area of 10 μm × 10 μm (100 μW excitation power, 100× objective, and 40 ms dwell time per pixel). (b) Histograms of intensity of two spectral locations shown by arrows (I) and (II) demonstrate uniform signal intensity within *ca.* 10% of average value for the fluorescence (arrow II) and *ca.* 20% for the Raman signal (arrow I). (c) Raman map formed using the 591 cm–1 Raman band (scale bar 2 μm) where the contrast is enhanced to show several dead-spots with submicrometer dimensions, demonstrating the high-resolution imaging capability with such substrates.

2.3.5. Discussion of Spatial Uniformity of Enhancement at the Nanoscale

Due to the periodicity of the meta-surface, Raman enhancement appears to be uniform in the far field when the diffraction-limited spot size is larger than the meta-material period. However, it is important to understand the variations of local enhancement factor within a unit cell. We plot the average and maximum enhancement factors for three different geometries, as shown in Figure 2-11, for MIM periods of 50, 100, and 250 nm. The averages are taken over rectangular sections over the top surface (10 nm thick slab is chosen), within the LFP region (air gap region between the top metals) and inside the MIM gap, within the dielectric (see Figure 2-11c inset). The dielectric gap of the MIM structure does not contribute to the Raman signal since molecules cannot be placed there after fabrication. However, enhancement in this region may be important for other applications; therefore, we plot enhancement factors for this region for convenience. The correlation of EF values for the MIM and LFP regions also demonstrates the coupling of LFP and MIM resonances. When comparing average and maximum EF of different regions and geometries, it is seen that for smaller structures (50 nm

period, 30 nm width, Figure 2-11a), a single resonance is present in the wavelength range of interest (532 to 640 nm), and average field enhancements at the top surface are greatly improved compared to 100 nm structures (Figure 2-11c) and 250 nm structures (Figure 2-11e). It is also seen that the LFP region has a stronger average enhancement factor as compared to the top surface and MIM gap. The maximum enhancement factors can be relatively large ($EF_{exc} \sim 1000$, $EF_{SERS} \sim 10^6$) for both small and larger periods (Figure 2-11b, d, and f). From the data, it can be concluded that, despite the apparent uniform enhancement in diffraction-limited far field measurements, enhancements are mostly localized to the LFP region for larger structures. For smaller structures (~50 nm period), although there is local non-uniformity and the LFP region still contributes the greater portion to the enhanced signal, the average EF values for the top surface and the LFP region have improved ratio, indicating improved uniformity.

The MCPM features propagation of multiple plasmon modes in the visible range of the spectrum, through direct capacitive coupling or coupling *via* a localized resonant mode. The simplicity of the MCPM allows fabrication of an ultrathin meta-surface with tailorable bands at wavelengths toward the near-UV. Bandwidths are comparable to thicker wideband absorbers[105]. Due to the quasi-omni-directional coupling of light to the plasmon modes, high spatial resolution SERS imaging is possible. The diffraction-limited spot size is greater than the period of the meta-material, and plasmonic enhancement of the Raman signal essentially occurs with a unity surface fill factor. High-resolution imaging capability can potentially improve biomolecular sensing[106], [107]. Raman excitation wavelength and scattering wavelengths coincide with different bands. Advancing the analogy of the meta-material with a semiconducting crystal, the Raman transition can be regarded as a photonic transition between two bands, where the transition is accompanied with the release of a phonon. Raman scattering constitutes an example for nonlinear optical phenomena, and in general, the MCPM can find application in cases where enhanced nonlinearity at low optical powers is desirable, such as enhancement of photonic interactions in all-optical classical or quantum information processing.

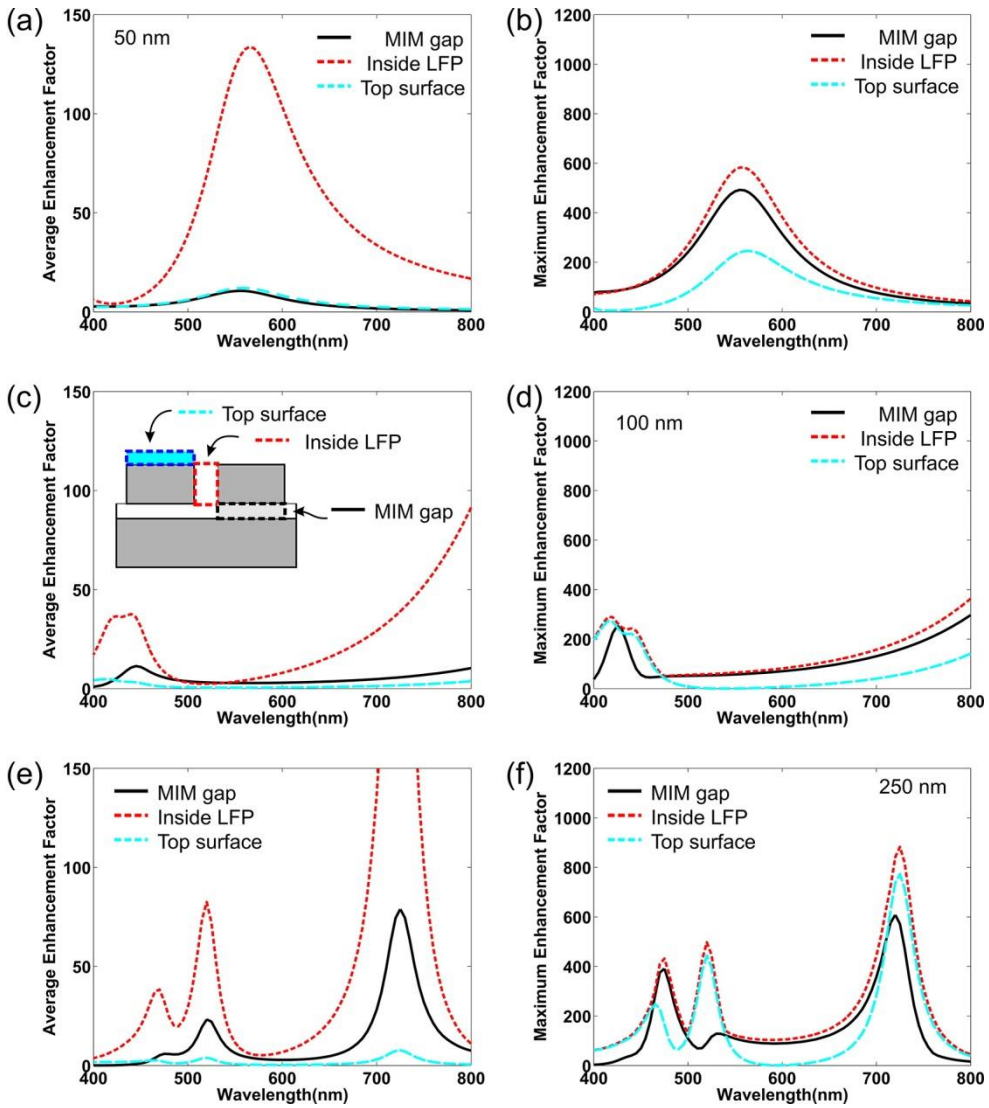

Figure 2-11. (a) Enhancement factors (EF) averaged over various regions (see inset in c) for a MIM structure with 50 nm periodicity, 10 nm top metal thickness, 20 nm dielectric gap, and 30 nm top metal width. (b) Maximum value of EF for different regions for the geometry in panel a. (c) Average EF values for a MIM structure with 100 nm periodicity, 20 nm top metal thickness, 20 nm dielectric gap, and 80 nm top metal width. (d) Maximum value of EF for different regions for the geometry in panel c. (e) Average EF values for a MIM structure with 250 nm periodicity, 50 nm top metal thickness, 20 nm dielectric gap, and 230 nm top metal width. (f) Maximum value of EF for different regions for the geometry in panel e. It is seen that shrinking the MIM size results in fewer resonances and improved average enhancement over the unit cell, especially on the top surface (10 nm thick slab over the top metal). The maximum values of the EFs are much higher than the average, showing the inherent spatial non-uniformity of enhancement. Comparing panels a–c, it is seen that tuning of the resonances through choice of geometry greatly improves EF for the wavelength range of interest (532 to 650 nm).

2.4. Edge Rounding Induced Broadband Plasmonic Metamaterial Absorber Structures

Perfect absorption of light can be achieved by exciting surface plasmons on textured metallic surfaces[108]. Metamaterials (MMs) are known as nanostructured metal surfaces to tailor the optical properties. So far, MMs are used to design negative index materials[47], optical sensor platforms[109], surface enhanced Raman spectroscopy substrate[110], solar cells[14], and optical bolometer imaging systems[111], [112]. Metamaterial absorbers (MMAs) are arrays of patterned metal insulator metal structures that have almost perfect absorption for certain wavelengths where impedance of MMAs are perfectly matched to the air's impedance near the resonant wavelengths. Nearly perfect MMAs are demonstrated in the microwave[113]–[115], terahertz[116], [117], infrared (IR)[21], [35], [97], [118]–[123] and visible frequencies[124]–[130]. Metamaterial absorbers in the visible spectrum can also be realized by using nanoparticles separated from a thick metallic ground plane with a dielectric spacer[131]–[133]. Typically, MMAs have narrow bands or single resonances attributed to their identical resonators in every unit cell[127], [128], [134], [135]. On the other hand, multispectral characteristic of a metamaterial plasmonic surface has great potential for various applications such as infrared absorption spectroscopy and surface enhanced Raman spectroscopy where the presence of resonances are generally accompanied by high field enhancements[63]. Recently, using more complex geometries broadband or multispectral MMAs are demonstrated in the visible and IR wavelengths. Multiplexing different resonator structures in a unit cell is another way to obtain multispectral absorption which requires precise control of dimensions of multiple nanostructures[114], [136]–[142]. However, multispectral MMAs based on the simultaneous excitation of electrical and magnetic plasmon modes is the least exploited approach[126], [143], [144]. MMAs are usually fabricated by using electron beam (e-beam) and optical lithography. The fabrications of nanostructures, however, are typically accompanied by process imperfections. Disc structures become more like truncated cones due to finite sidewall angle and square structures have rounded corners due to lithographic nonidealities. These fabrication related features are exploited in our MMA structure which has already multispectral absorbance bands due to the excitation of both electrical and magnetic plasmon

modes. Particularly, when corners of the top nano-square patches are rounded, a new resonance is observed to emerge. The proposed structure takes into account the imperfections of common fabrication techniques and is therefore more realistic. Unlike the multiplexed metamaterial structures having multiple resonators with different geometries in a unit cell, the multiband plasmonic structure studied here only requires the control of width of the structures to obtain multispectral and broadband response.

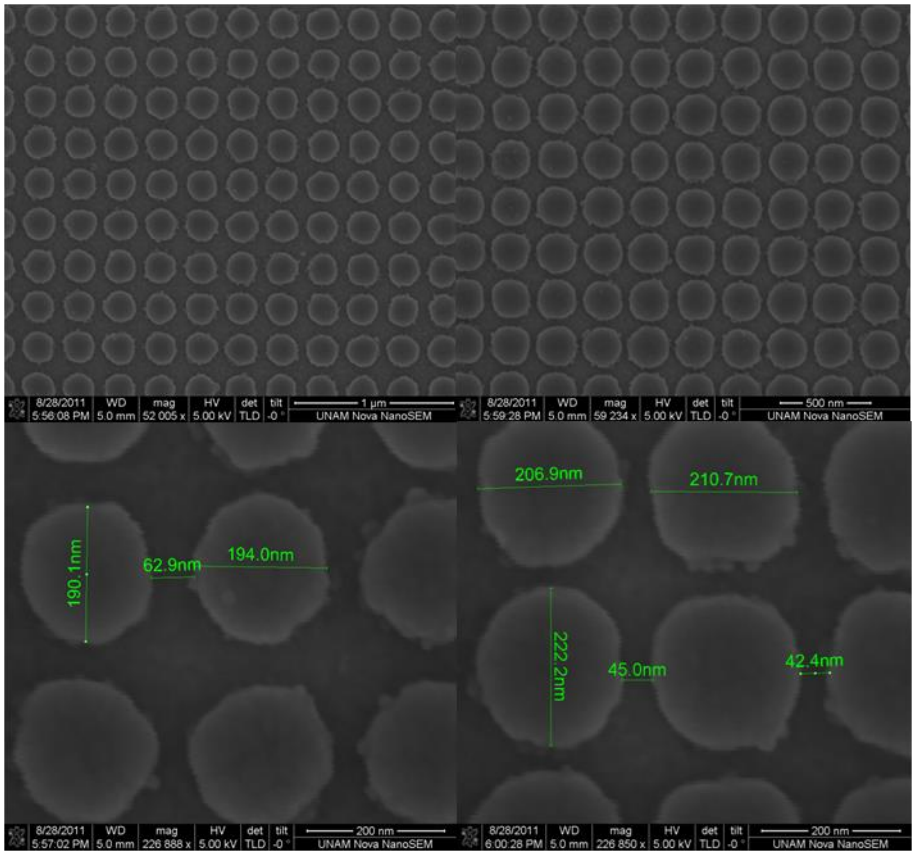

Figure 2-12. SEM images of polarization independent plasmonic metamaterial surface. The fabricated structures are disc-shaped despite they are aimed perfect squares.

2.4.1. Simulation Geometry and Method

The schematic description of the proposed structure is shown in Figure 2-13. The structure is based on metal/insulator/nano-square array geometry. Silver is used for both bottom metallic plane and top nano-square arrays. Alumina (Al_2O_3) is used as the dielectric spacer layer. The thickness of the bottom (ground) plane is 100nm for all the simulations where transmission is almost zero in the visible range. The thickness of the top layer is chosen 50nm, allowing the coupling of localized surface plasmon modes due to the interaction of adjacent square patches. Periods of square patches along x, y directions are 250nm. The simulations are based on the Finite Difference Time Domain (FDTD) method (Lumerical FDTD). The material properties (complex and real parts of dielectric function) for silver and alumina are obtained from the program's material database and fitted to a 12 order function (Palik data). The mesh size used in FDTD analysis is 2nm for both x and y directions and 1nm for z direction. A broadband electromagnetic plane wave for normal incidence illumination is used with 400nm-750nm wavelength range. Bloch boundary conditions are chosen for x and y directions and perfectly matched layer (PML) is used along the z direction. Simulation durations are further decreased by using asymmetric and symmetric boundary conditions along x and y directions.

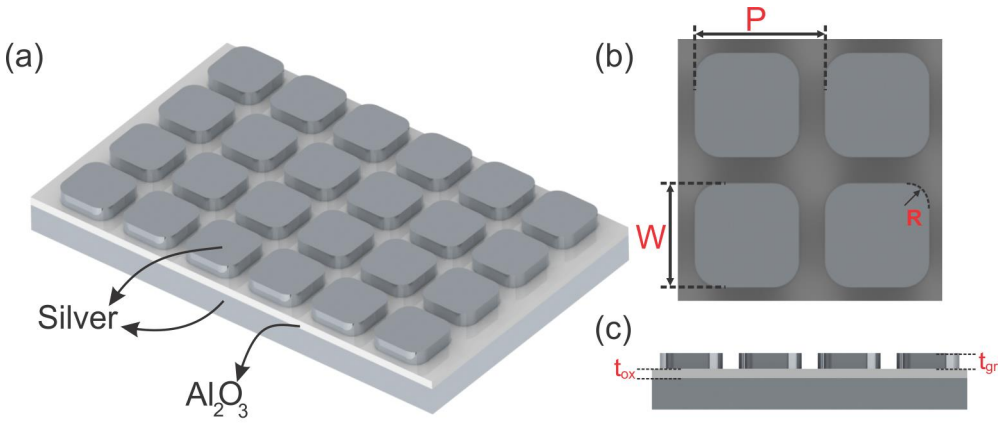

Figure 2-13. (a) Schematic description of the proposed MMA structures. Top (b) and side (c) view of simulated structures. Periods in x and y directions are 250nm. W is width of the patches and R is the curvature of the corners.

2.4.2. Results

In Figure 2-14a dual band absorber structure is demonstrated when the curvatures are omitted in the simulations and perfect square patches are assumed (R=0nm). When there is no oxide in the structures, single resonance at λ=530nm is observed due to the cavity resonance between the patches. When, a t_{ox}= 30nm of oxide spacer is included, the resonance splits into 2 modes at λ_1=480nm and λ_2=605nm as shown in Figure 2-14a. To understand the origin of these resonances electric and magnetic field distributions are plotted as seen in Figure 2-14c. Without the oxide layer, layer magnetic field is localized in the grooves and electric field is higher at the top of the adjacent ridges. This resonance resembles an electric plasmon mode. With the oxide layer, magnetic field is also confined in the grooves at λ_1=480nm. For λ_2=605nm, magnetic field is confined in the spacer layer. Hence, resonances at λ_1=480nm and λ_2=605nm are electrical and magnetic plasmon modes respectively. Then, we investigated effect of the nano-square patch width as shown in Figure 2-14b. The resonance at shorter wavelength is unaffected with increasing W which also suggests that the resonance is electric plasmon mode[126], [145]. However, as the width increases the resonance at higher wavelength shifts to longer wavelengths which verifies a magnetic plasmon mode. This resonance can be explained in terms of standing waves by $\lambda_r = 2n_{eff}\mathrm{W} + \theta$ where n_{eff} is the effective index of MIM mode, θ is the phase term due to reflections from the edges. Resonance wavelength linearly depends on W[146].

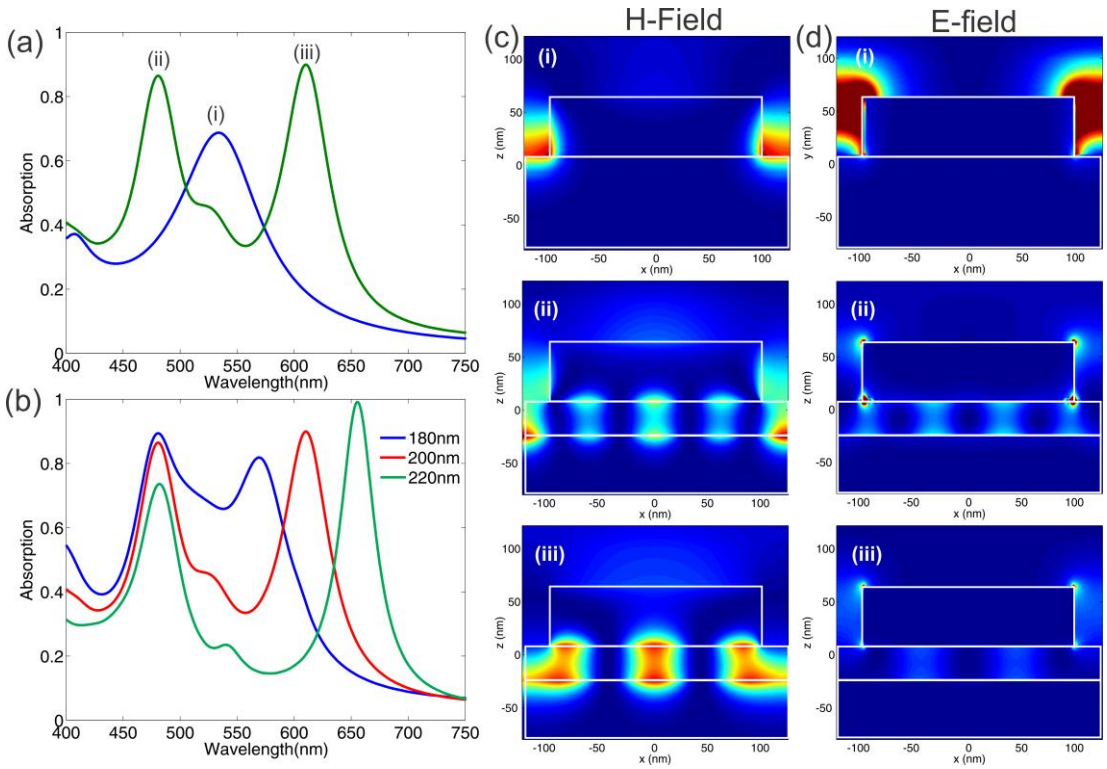

Figure 2-14. (a) Absorption spectra of the MMA structure with perfect nano-square patches (R=0nm) for t_{ox}= 0 (blue) and t_{ox}= 30nm (green) (b) Absorption spectra for various nano-square patch widths (t_{ox}= 30 nm). Magnetic (c) and Electric (d) field profiles at the resonances shown in (a).

When the structures are fabricated using electron beam lithography, due to the finite point-spread function width of the exposure process, the corners of the square patches get rounded. In order to demonstrate the effect of round corners in the absorption spectra, curvature is added to the corners of nano-square patches in the simulation (See Figure 2-13). Figure 2-15 shows the emergence of a third mode whose resonance frequency is affected by the radius of curvature of the corners. For W=200nm, R=0 nm up to R=40nm there are two distinct resonances as shown in Figure 2-15a, c. When the curvature is further increased, the magnetic plasmon mode splits into two. For R=100nm where the nano-square patches become perfect discs, three resonances are observed with almost equal wavelength spacing. The absorption of each resonance is higher than 85%. For a small change of the width of the patches, to W=210nm, the magnetic plasmon mode splits into two at a smaller curvature value (R~30nm). The wavelength spacing between the resonances is higher for the maximum curvature value (R=105nm) and, near perfect absorption is seen for the middle resonance around 550-600 nm. We further investigated the effect of dielectric thickness on the absorption of triple band plasmonic structures as shown in Figure

2-15 e, f. The electric plasmon mode at λ~500nm is almost independent of the spacer thickness as expected. However, the magnetic plasmon modes strongly depend on the spacer thickness which is due to the change in effective refractive index of the MIM waveguide formed by the top patch and bottom Ag layer, with the increasing spacer thickness.

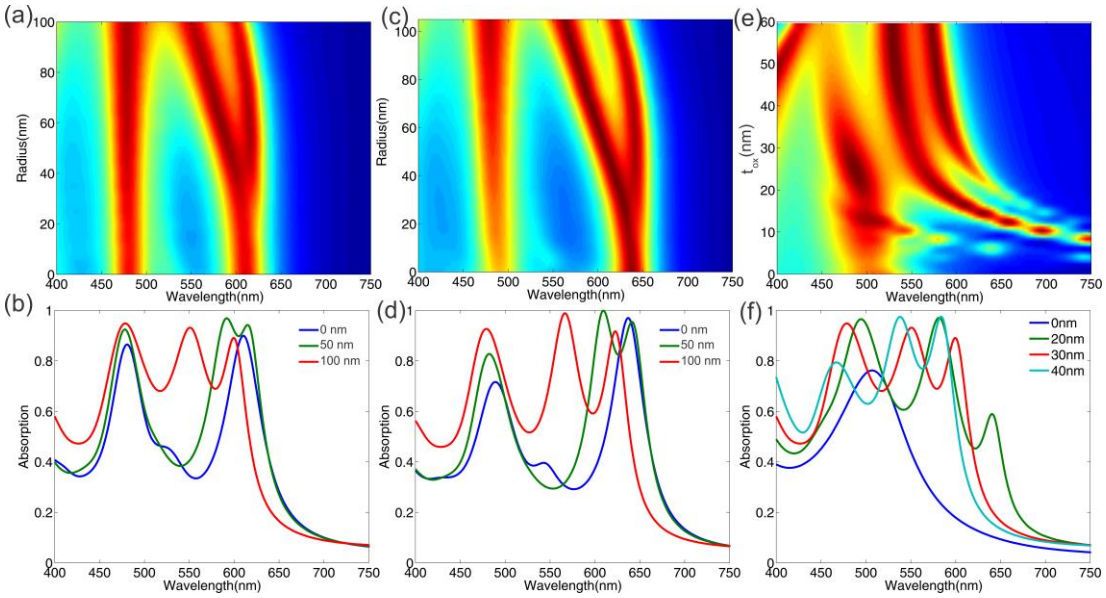

Figure 2-15. Effect of the curvature on the absorption spectra for W=200nm (a,b) and W=210nm (c,d) for t_{ox}=30nm. Effect of the oxide thickness on the absorption spectra for W=200nm and R=100nm (e-f). The magnetic plasmon mode splits into two modes at smaller radius as the width of the resonator increases.

In order to understand the origins of the resonances for the perfect nano-disc top layer (R=100nm, W=200nm), we have plotted the electric field profiles at λ=550nm and λ=600nm. The analytical approaches for circular nano patch antennas have been recently demonstrated[147], [148]. Following the steps shown in previous literature, the Helmholtz equation for metal-insulator-metal (MIM) geometry is solved in the cylindrical coordinates which is

$$\frac{\partial}{\partial\rho}\left(\rho\frac{\partial E_z}{\partial\rho}\right)+\frac{1}{\rho^2}\left(\rho\frac{\partial^2 E_z}{\partial\varphi^2}\right)+\frac{\partial^2 E_z}{\partial z^2}+k^2E_z=0 \qquad (2.30)$$

The solution to Equation 2.30 is given by $E_z=J_m\left(k_{sp}\rho\right)\cos(m\varphi+\vartheta)\,(Ae^{k_z z}+Be^{-k_z z})$ with Neumann boundary condition $\partial E_z/\partial\rho$=0 where $k_{sp}$is the wave-vector for the MIM cavity. The solution to electric field distribution is given in terms of even and odd modes as E $(O)_{mn}$ where n is the order of the roots for $\partial\left(J_m\left(k_{sp}\rho\right)\right)/$

$\partial\rho$ =0. For odd and even values of m odd and even order modes are excited, respectively. The simulated and calculated mode profiles are shown in Figure 2-16. For λ=550nm which is due to the corner curvature effect, O_{12} mode is excited as shown in Figure 2-16a, c while the magnetic plasmon mode at λ=600nm resembles O_{31} mode after the corner curvature effect (Figure 2-16 b, d).

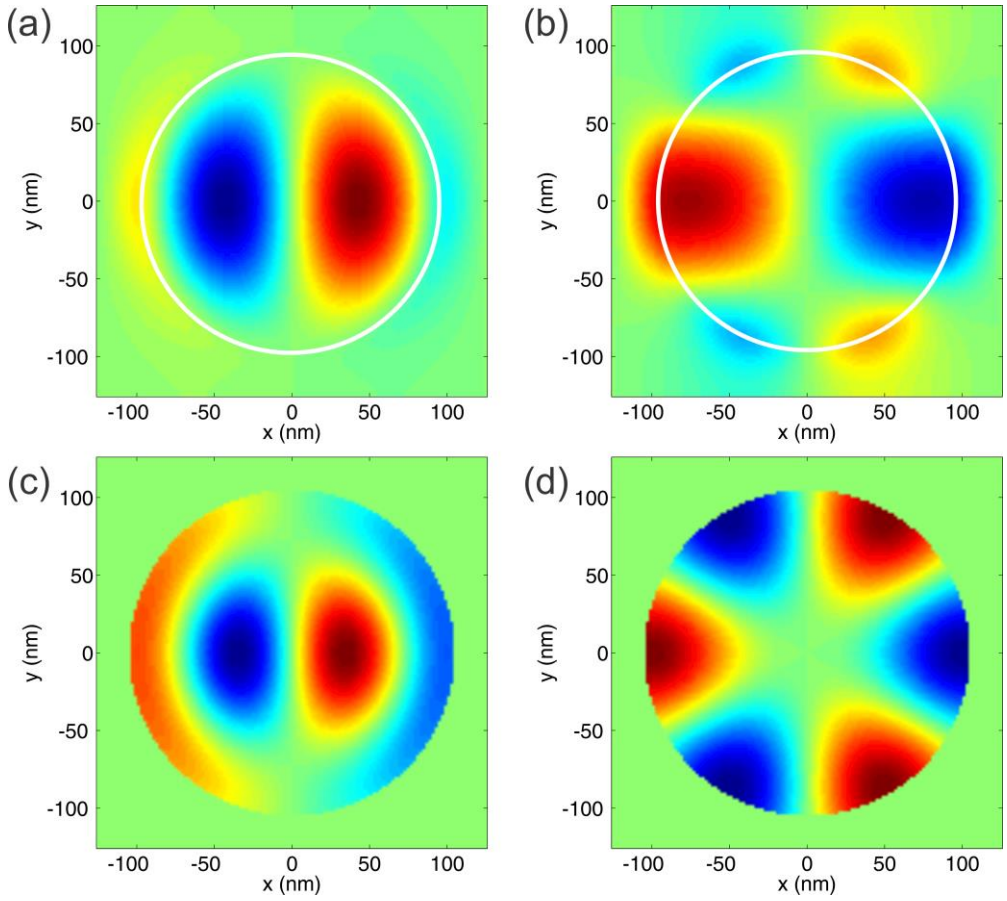

Figure 2-16. Origin of resonances for W=200nm, R=100nm and tox=30nm. Simulated z component of electric field profiles for λ=550nm (a) and λ=600nm (b). Calculated electrical field profiles for modes m=1, n=2 (c) and m=3, n=1 (d).

Fabrication of MMAs requires lithography and liftoff processes which results in slanted sidewalls of patterned surfaces. Figure 2-17a shows the cross section of a typical MMA structure. To demonstrate the effect of the side angle on the absorption spectra of the triple band absorber structure, we simulated a truncated cone shaped top metallic layer rather than a perfect disc (corresponding to sidewall angle θ=90). Absorption spectrum of such a structure is shown in Figure 2-17b, c. As the side angle decreases down to θ=75 degrees we can observe a resonance at λ=600nm, but for smaller side angles this resonance diminishes. A broad absorption band covering 400 to 550 nm can be observed for smaller sidewall angles. For θ=85 degrees or

higher, we still observe triple bands. Such a structure with high side angles can be fabricated using inductively coupled plasma or reactive ion etching , after e-beam lithography on MIM films .

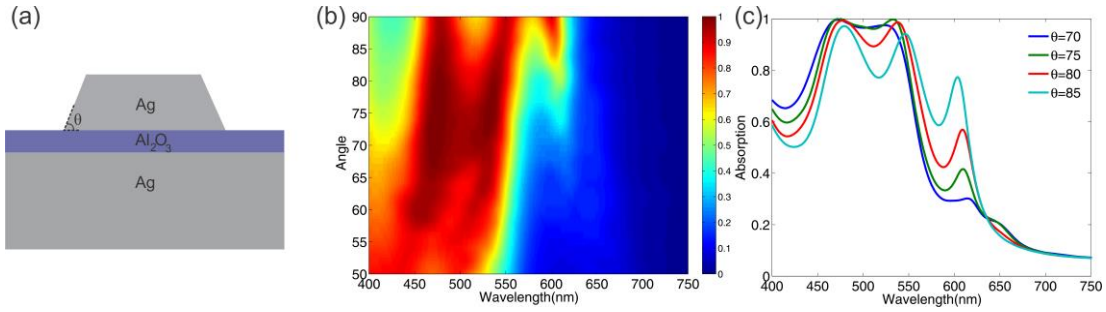

Figure 2-17. Effect of side angle on the absorption spectra. (a) Cross section of the simulated structure. (b-c) Absorption spectra with respect to the side angle. As the slope of the cone increases absorption of magnetic resonance mode decreases.

2.5. Conclusion

In this chapter 1D and 2D periodic coupled plasmon meta-surfaces are presented. For the 1D case we have developed a circuit model to understand the coupling mechanisms of different modes. Due to wide-band width of these surfaces, Raman signals can be amplified for both excitation and stokes wavelengths. The proposed geometry is also subwavelength (Period=250nm) which results in unity Raman enhancements over large areas. Moreover by utilizing the analogy of heavy and light molecule analogy, Raman transition can be seen as a photonic transition between two bands. For the 2D case, we demonstrated a triple band plasmonic metamaterial surface due to edge rounding effects occurred during the fabrication process. The emerging third resonance is attributed to the excitation of circular cavity modes.

Chapter 3

Nano-particle Based Large Area Broadband Plasmonic Surfaces and Their Applications

In this chapter we present a large area plasmonic surface based on metal-insulator-nano-particle geometry which supports localized surface plasmon modes over large bandwidths. The broad bandwidth is due to excitation of the electric and magnetic plasmon modes. The electric plasmon mode is due to inter-particle coupling. Field is confined to the insulator layer for the magnetic plasmon mode. We used these surfaces for single molecule Raman spectroscopy and as hot-electron detectors. For the first time, we have observed single molecule Raman events using a mobile phone's camera. Moreover, we have also developed a contact free characterization technique using x-ray photoemission spectroscopy (XPS) by probing hot-electrons emitted from individual metal-insulator-nano-particle photodetector.

Parts of this chapter were published as;

1. Sencer Ayas, Andi Cupallari,Yasin Kaya, O.O. Ekiz, Aykutlu Dana,"Counting Single Molecules With a Mobile Phone Camera Using Plasmonic Enhancement", **ACS Photonics**,1,1,2014

2. Sencer Ayas(*), Andi Cupallari(*) and Aykutlu Dâna,"Probing Hot-Electron Effects in Wide Area Plasmonic Surfaces using X-Ray Photoelectron Spectroscopy", **Appl. Phys. Lett.,**105, 221608 (2014) (* equal contribution).

3.1. Large Area Plasmonic Metasurfaces

We use the same geometry we have developed in the chapter 2 for the applications presented here. However, fabrication of such surfaces requires top-down fabrication techniques such as electron-beam lithography and focused ion beam (FIB). We have developed a large area plasmonic surface by dewetting of thin Ag films over insulator/metal surfaces. Substrates fabricated by dewetting of silver films were studied before for their plasmonic properties and SERS enhancement[149], [150]. Metals near percolation threshold have localized surface plasmon resonance due to their nanoparticle nature. By changing fabrication conditions, resonances of the surface can be tuned. Placing metal nanoparticles over a metal surface, with an dielectic separator in between, results in strong changes in overall plasmonic properties due to the interaction of metal nanoparticles with the metal film[44], [151]–[153]. It is seen that Ag nanoislands form at a mass thickness of 1 nm, coarsening takes place at 3 nm and percolation begins at 5 nm mass thickness (Figure 3-1a). For 3 nm top metal mass thickness, the gap between individual nanoparticles is about 5-10 nm and nanoisland thickness is 10 nm on average. HfO_2 thickness of 30 nm and Ag nanoisland layer mass thickness of 3 nm produce a wide band perfect absorber as measured by spectroscopic ellipsometry (Figure 3-1c, d). The metasurfaces are quasi-omnidirectional and absorption is above 90% for the 30 nm thick HfO_2 sample over a wavelength range of 450 to 800 nm, for angle of incidence of up to 60 degrees (Figure 3-1e).

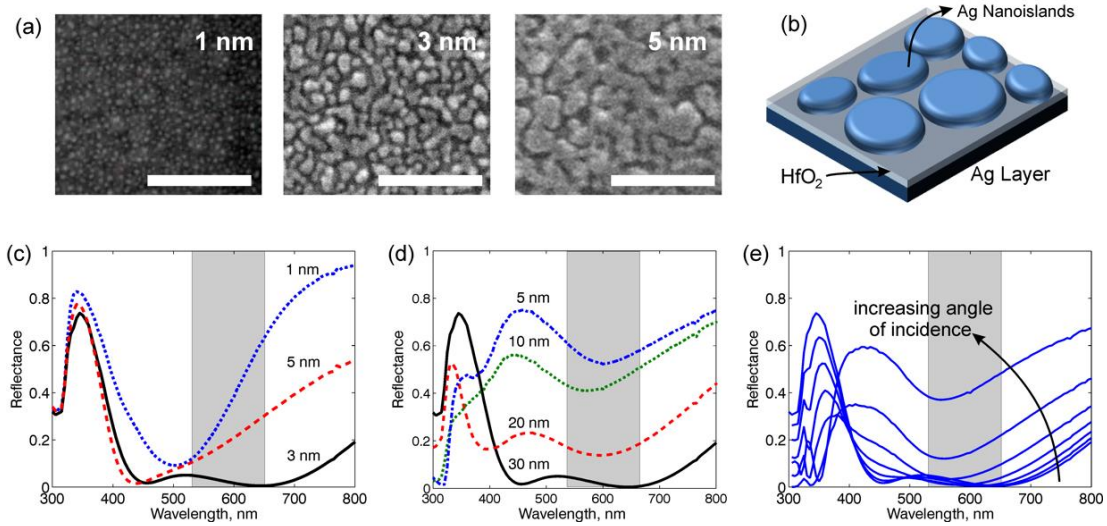

Figure 3-1. (a) SEM of plasmonic surfaces with 1, 3 and 5 nm mass thickness Ag overlayer shows coarsening and percolation of Ag nanoislands. Scale bars 250 nm. Plasmonic field enhancement is greater as the nanoislands approach each other, reducing the inter-particle gap. 3 nm mass thickness sample exhibits greatest hot spot density. (b) Schematic view of the substrate showing layer structure. (c) Reflectance of the surfaces near normal incidence for 1, 3 and 5 nm mass thickness Ag over-layer and 30 nm HfO_2. Gray band shows the wavelength region of interest for Raman scattering excited by 532 nm light. Ag mass thickness of 3 nm results in a wide band meta-surface. (d) The reflectance is plotted for HfO_2 thicknesses of 5, 10, 20 and 30 nm. (e) Dependence of reflectance on angle of incidence is plotted for 20, 30, 40, 50, 60, 70 and 80 degrees. The 30 nm HfO_2/ 3nm Ag surface is quasi-omni-directional, maintaining high absorption over a wide wavelength range at angles up to 60 degrees.

Electromagnetic properties are calculated for periodic nano-islands with 75 degree sidewall angles (Figure 3-2a, b), as well as for SEM data based model surfaces (Figure 3-2c, d and Figure 3-3) using computational tools. Plasmonic metamaterial surfaces have been demonstrated to have broadband absorption and superior field enhancements that are fabricated using electron beam lithography[127]. In contrast, the surfaces presented here require no lithography, hence are easy to fabricate over large areas. The resonance wavelengths can be tuned by changing the thickness of spacer layer and by control of island diameter and thickness. Optimized surfaces with 30 nm HfO_2 dielectric thickness and 10 nm island thickness have broadband plasmon resonances over the whole visible spectrum with almost 90% average absorption.

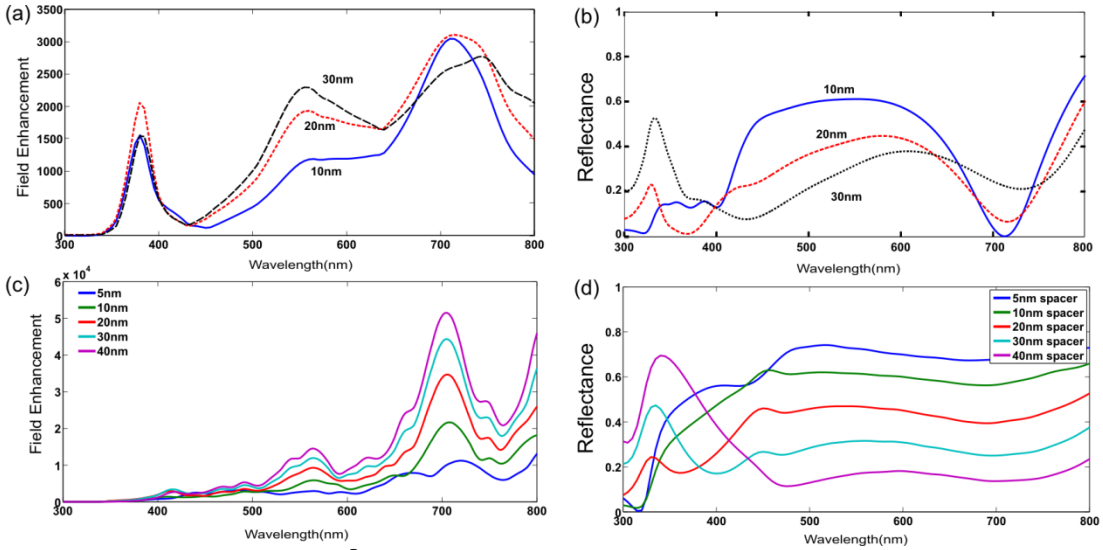

Figure 3-2. **.** (a) Maximum $|E|^2$ field enhancement factor as a function of wavelength, plotted for 10, 20 and 30 nm dielectric thickness for a periodic arrangement of Ag nanoislands (40 nm period, 10 nm thickness, 35 nm island size, 75 degree sidewall angle), shows increase in the enhancement around 550 nm as thickness increases to 30 nm. (b) Calculated reflectance of the periodic arrangement, plotted as a function of wavelength. (c) Maximum $|E|^2$ field enhancement factor as a function of wavelength, for a quasi-random surface derived from SEM data as a function of dielectric thickness. (d) Calculated reflectance of the quasi-random arrangement, plotted as a function of wavelength and dielectric thickness. A dielectric thickness of 40 nm is also included in the calculations, as it better fits the experimental reflectance for 30 nm HfO_2 shown in Figure 3-3.

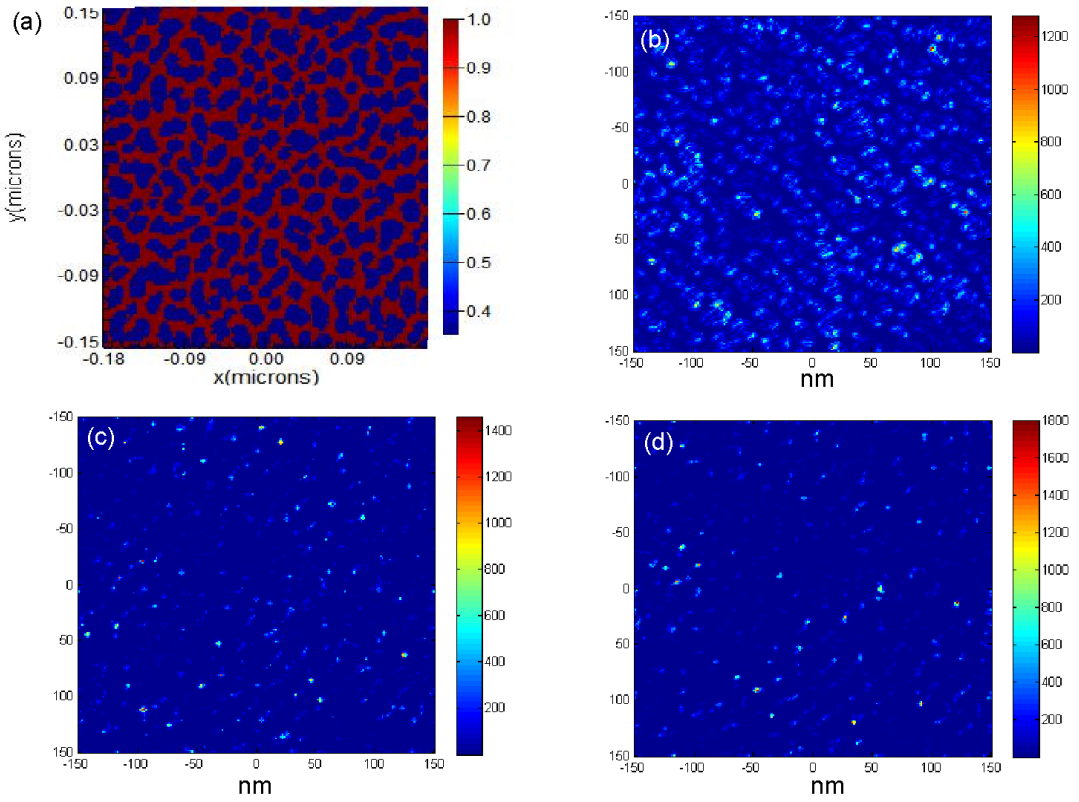

Figure 3-3. SEM derived surface model for field enhancement and reflectance calculations. a) The SEM data is used to extract silver island shapes. b) Field enhancement factor ($|E|^2$ for 550 nm excitation) at the top metal-dielectric interface. c) Field enhancement in the middle point of upper boundary of the top metal and dielectric interface. d) Field enhancement at the upper boundary of the metal islands.

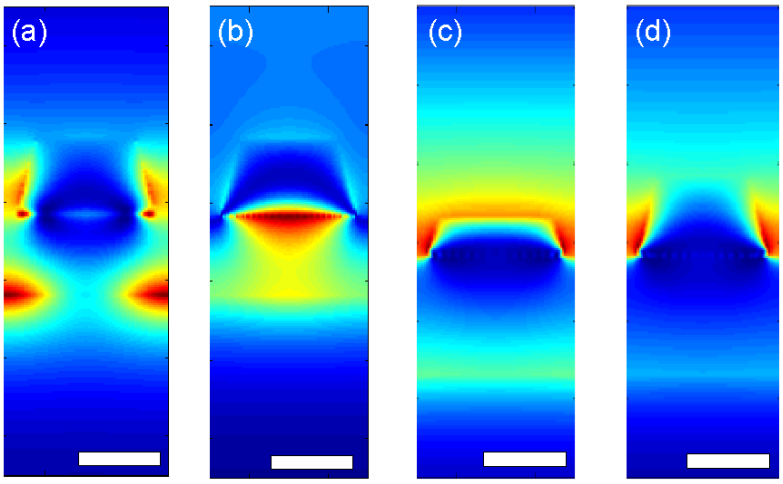

Figure 3-4. (a) Cross sectional magnetic field profile for a periodic arrangement of metal-insulator-metal resonators (40 nm period, 35 nm width, 20 nm thickness, 75 degree sidewall angle Ag, on 20 nm HfO2, on Ag) at 430 nm excitation wavelength and (b) at 700 nm excitation wavelength. (c) For a top metal thickness of 10 nm, fields have enhancement at the top surface (excited at 550 nm) as compared to (d) a top metal thickness of 20 nm (all scale bars are 20 nm wide).

The broadband absorption is due to both the inter-particle and particle-metal film couplings. Mode confinements are shown for a periodic nano-island arrangement as shown in Figure 3-4. Inter-particle coupling is attributed to a dipolar coupling between individual nano-particles, which is known as electrical resonance where magnetic field is confined between the nano-particles (Figure 3-4a). The particle-metal film coupling, typically referred to as the magnetic resonance has the magnetic field confined to the spacer layer (Figure 3-4b) [94]. A coupling of the two types of resonances is also present and enhances the absorption in the intermediate wavelength region between the two resonances. The thicknesses of the Ag islands are important for having an optimal enhancement (Figure 3-4c, d). For single molecule SERS enhancement, the surfaces need to be optimized, and optimal SERS enhancement is achieved when plasmonic resonances cover the range of excitation and scattering frequencies[154]. We optimized the SERS enhancement at excitation and scattering wavelengths (532 to 650 nm wavelength range, corresponding to Raman range of 0 to 3500 cm^{-1}) by sweeping the fabrication parameters. The dielectric layer is very important in achieving the enhancement levels presented here, and provides about an order of magnitude improvement. This effect is studied recently by independent groups, using SiO_2 as the spacer[30].

3.2. Single Molecule Raman Events Using Large Area Plasmonic Surfaces

Plasmonic structures can enhance the Raman signal significantly, thereby increasing the signal from single or few molecules to levels that can be detected using a cooled CCD spectrometer or a photomultiplier. In order to characterize the spectral content of the single molecule blink events, we record the time dependent Raman spectra on a bright hot spot, using a cooled CCD spectrometer, as shown in Figure 3-5. The integrated intensity between 0-3500 cm^{-1} is plotted as a function of time in Figure 3-5a. The integration time of the spectrometer is 100 ms. Sudden changes of the spectrum are observed as peaks in the time series. The spectra show distinct Raman bands which fluctuate in both intensity and frequency, which is commonly interpreted as a positive indication for single molecule level sensitivity (Figure 3-5b). The debate about the interpretation of fluctuating Raman bands as

evidence for single molecule SERS is ongoing in the literature[155]–[159]. It is claimed that, thermally activated diffusion and Brownian motion of molecules are possibly responsible for the observed SERS signals[160]–[162]. Fluctuations of intensity of optical emission from silver nanoparticles were claimed to be independent of the intentional presence of probe molecules but an inherent feature related to Ag nanoparticles[163]. However, we note that in our experiments, when untreated surfaces are subjected to airborne molecules, for example by spraying a mixture of carbon compounds from a fragrance bottle, a sudden increase of blinking is observed. Diffusion of large molecules on metal surfaces has been directly observed and characterized using scanning tunneling microscopy[164]–[166]. Also, spurious lines are routinely present in blinking SERS spectra[167]. Based on such previous observations, we attribute the unidentified spectra to the presence of adsorbed volatile organic compounds present in ambient air[168], [169]. It is observed that the plasmonic substrates also enhance the fluorescence signal, and once in a while a broad fluorescence spectrum is captured as shown in Figure 3-5c. Such enhancements of the fluorescence were previously studied using plasmonic antennae[170]. The optical spectrum during most blink events exhibit Raman bands, shown in Figure 3-5d, typically superimposed on a broad fluorescence background from the Ag nano-island layer. In comparison, no signal can be observed on a flat Ag surface.

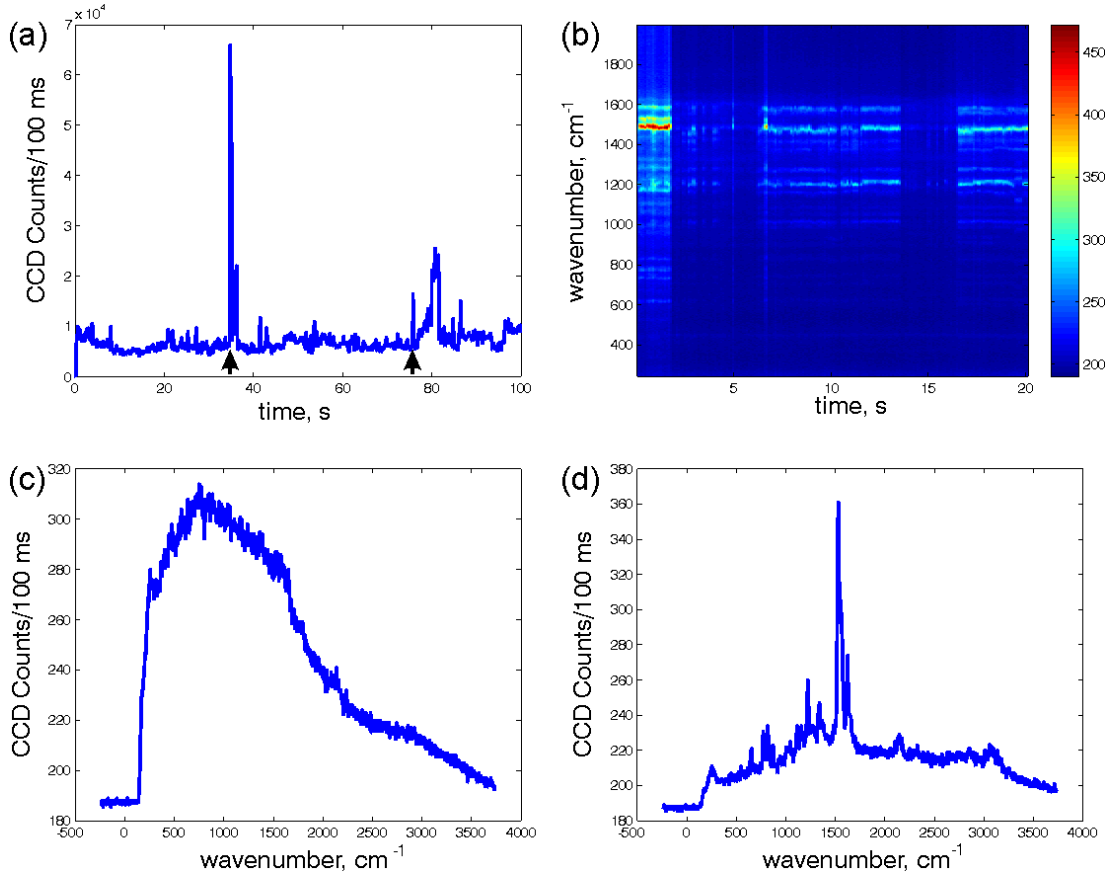

Figure 3-5. (a) Time series of the integrated intensity within 0 to 3500 cm^{-1}, as recorded by the cooled CCD spectrometer on a particularly bright hot-spot, shows blinking events as fluctuations in the intensity (500 µW of excitation at 532 nm). (b) The time series plotted to feature the full spectrum exhibits Raman lines that fluctuate in intensity and frequency, characteristic of single molecule SERS. (c) Occasionally, a fluorescent molecule is captured in the hot-spot (at time 35 s in (a)). (d) Typical Raman spectra during a SERS blink (at time 76 s in (a)) exhibits a broad fluorescence superimposed with distinct Raman bands.

3.2.1. Observation of Single Molecule Raman Events Using Smart Phone's Camera

We have used mobile phone's camera in two configurations. First, we captured the blink events directly placing the smart phone to the eyepiece of Raman setup as shown in Figure 3-6.

The blinks are captured using the smart phone camera at 30 fps, and are shown in Figure 3-7a. The relative enhancement of the substrates as a function of dielectric thickness and Ag over-layer thickness can be seen in the increase of fluorescence signal from the Ag nanoisland layer. A dielectric thickness of 30 nm and an Ag over-layer mass thickness of 3 nm produces the highest blink rate with high blink intensities, an observation which correlates well with the reflection spectra of the surfaces. The blinks are counted using QuickPalm and histograms are generated as

shown in Figure 3-7b[171]. The pixel noise superimposed on the fluorescence background causes the QuickPalm algorithm to detect erroneous blink events with low peak intensity, causing an increased blink count at low intensities.

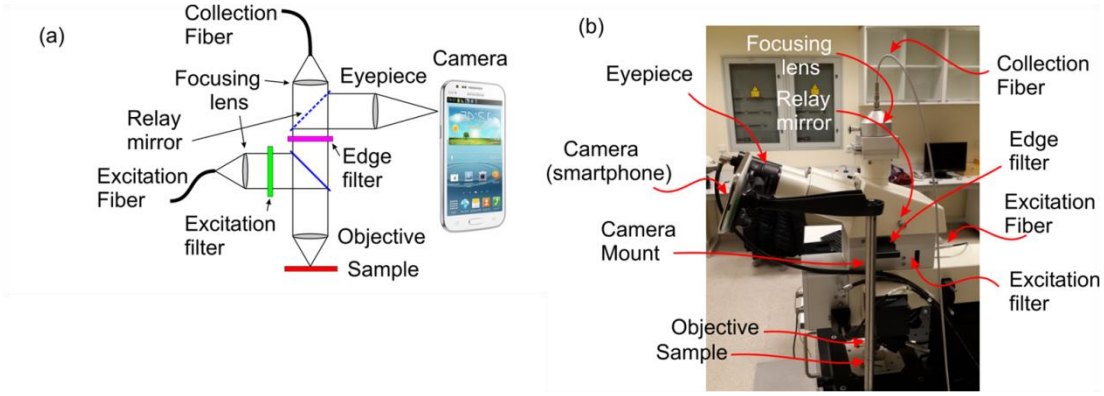

Figure 3-6. a) Schematic of the measurement set-up for using the camera of a smart-phone for imaging with a confocal Raman system. b) Photograph of the measurement set-up showing various components described in (a).

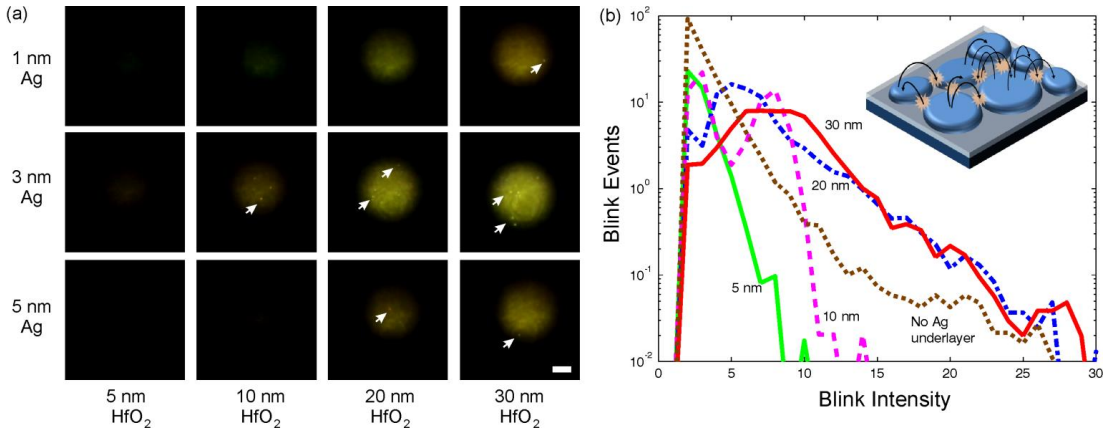

Figure 3-7. (a) Frames from video captures using the smart phone camera on plasmonic surfaces with 1, 3 and 5 nm mass thickness Ag over-layer and 5, 10, 20, 30 nm HfO_2 dielectric layer thickness. Excitation laser is defocused to illuminate an area 50 µm in diameter. Arrows denote blink events on a fluorescence background of the Ag nano-island layer. Scale bar is 20 µm wide. (b) Video frames are analyzed to extract a histogram of blink event intensity for the 3 nm Ag samples at varying HfO_2 thickness. A dielectric thickness of 30 nm produces brightest blink events. As the bottom Ag layer is removed (dielectric thickness infinite), blink events can still be observed, however at a decreased rate and intensity. Inset shows the potential source of blinking, i.e. surface diffusion of physisorbed volatile organic compounds into and out of hot-spots.

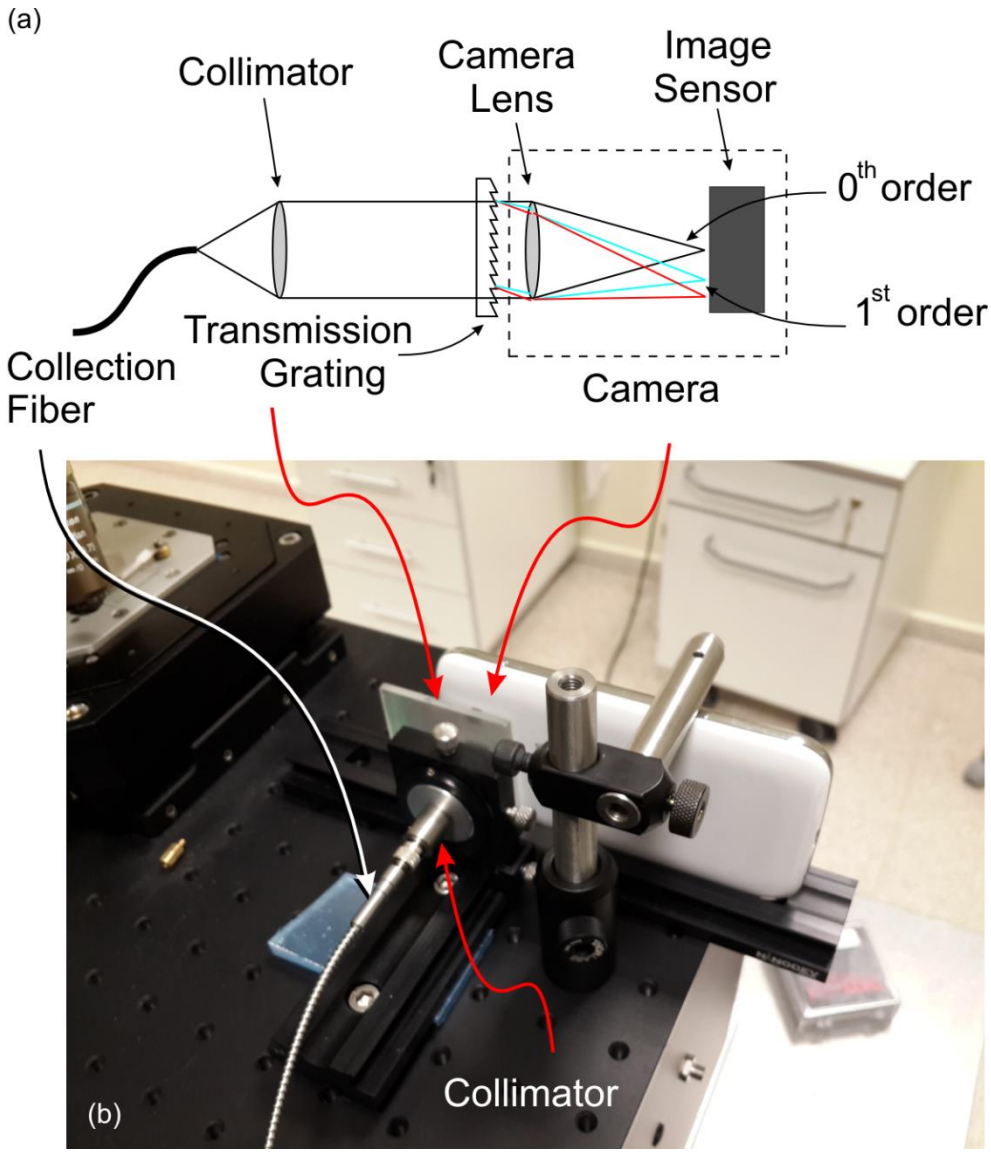

Figure 3-8. a) Schematic of the spectrometer configuration. b) Photograph of the measurement set-up showing various components described in (a).

Second configuration for probing single molecule events is shown in Figure 3-8. This configuration is simply a spectrometer configuration. The collection fiber output is collimated using a lens and a transmission grating is positioned before the focusing lens of the camera. In this configuration, wavelength separation of the light can be achieved with reasonable linearity. A similar configuration has been recently used to record the spectra of a white light source and perform label-free biomolecular detection[172]. The wavelength dependent response is not uniform due to the color filters on the camera, however we do not attempt spectral equalization and use the data as it is extracted from the snapshots and video captures. We record the unenhanced Raman spectrum of silicon and ethanol on silicon using the cooled CCD spectrometer as shown in Figure 3-9b and compare the results with the smartphone-

spectrometer data shown in Figure 3-9c. A 600 lines per mm (lpmm) transmission grating allows observation on 0^{th}, 1^{st} and 2^{nd} order diffraction orders, as shown in the insets. A close-up of the 2^{nd} order region is shown in Figure 3-9d, superimposed with the original Raman spectra shown in Figure 3-9b, convolved with a point spread function of the smartphone-spectrometer. The resolution (> 180 cm^{-1} for 532 nm excitation) is limited by the diffractive power of the grating as well as the diameter of the fiber (25 µm diameter) and focal length of the collimator (10.99 mm, F220-SMA-B Thorlabs). The fluctuating Raman spectra can be recorded using the SERS substrate as shown in Figure 3-10a, where multiple snapshots are recorded consecutively, using a 600 lpmm grating, with an integration time on the order of 1 sec. Distinct spectral features can be observed during blink events. The spectral features can still be observed at 30 fps, as shown in Figure 3-10b. In order to demonstrate the superior signal intensity of SERS, we record the Raman spectra on plasmonic substrates treated with 10 nM Methylene Blue solution and 1 µM Cresyl Violet solution in using 100 µW excitation (Figure 3-10c, d). Corresponding spectra are also captured using the smart phone camera as shown in Figure 3-10e, f. Although the fluctuating spectra contain signatures that can be attributed to Cresyl Violet and Methylene Blue, spurious signals are also present that show presence of unidentified molecules occasionally producing Raman bands. As SERS spectra are typically modified as compared to bulk spectra, we do not attempt to identify the spurious molecules.

Although the experiments were performed on a non-portable microscope system, the setup does not differ from a fluorescence measurement setup and can be potentially miniaturized. Use of low excitation powers (0.1 to 10 mW) also favors the potential for miniaturization. It must be noted that, although electromagnetic calculations estimate an overall enhancement factor of about 10^7, the large intensity of the blinking signals suggest that the chemical or first layer contribution to SERS is not negligible. Such chemical enhancement can be significant, up to two orders of magnitude chemical enhancement due to complex mechanisms leading to charge transfer between the metal and the probe molecule has been predicted[173]. Therefore, the SERS spectra differ significantly from unenhanced Raman spectra, and should be understood beyond simpler electromagnetic models. On the other hand, SERS spectra are repeatable in themselves, and the plasmonic substrates that enable the observations can be fabricated on large area substrates without the need

for top-down patterning, therefore can be produced at low cost. The width of the spectra acquired using a 600 lpmm grating is about 1/8th of the overall field of view. In principle, by using a grating with higher groove density, the dispersion can be increased and resolution of the spectrometer configuration can be improved to better allow discrimination of spectra. However, for using the full field of view of the camera, additional optics may be required to improve the resolution to about 20 cm^{-1}. The remarkable sensitivity of the smart phone camera combined with high plasmonic enhancement of the optical signal, may pave the way for low cost hand-held systems which can be used in the analytical study of samples at a single molecule level.

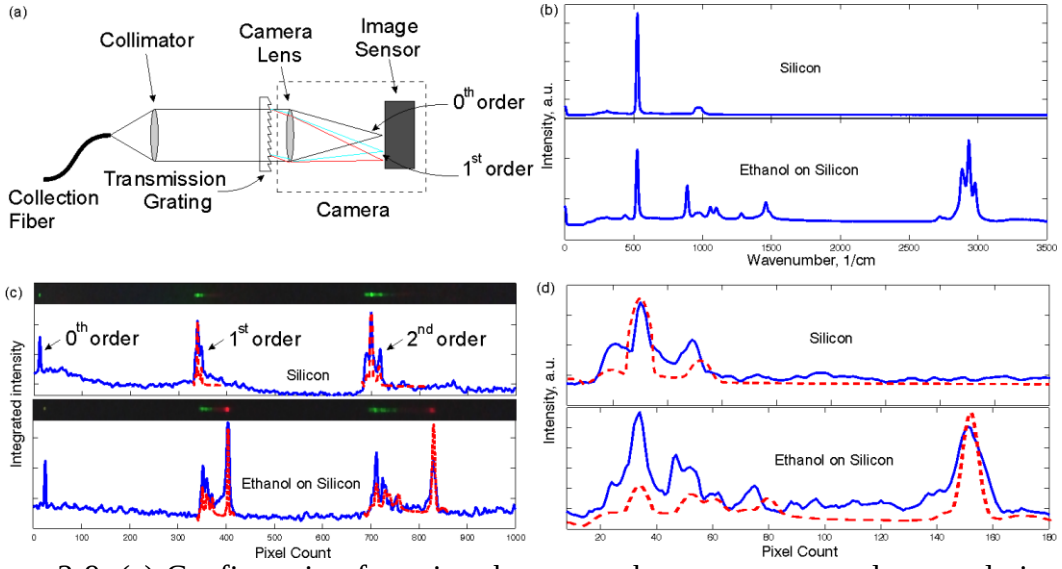

Figure 3-9. (a) Configuration for using the smart phone camera as a low resolution spectrometer. The collection fiber from the Raman set-up is collimated and dispersed with a transmission grating (300 lines per mm) before entering the camera. (b) Raman spectra of silicon and ethanol on silicon collected with 13 mW of 532 nm excitation using the cooled CCD spectrometer are shown. (c) Smart phone camera recordings of the two orders of the dispersed input light in the snap-shot mode. Solid blue lines show integrated pixel intensity and dotted red line shows superimposed Raman spectra convolved with a lineshape function that represents the point spread function (PSF) of the optical configuration. Insets show actual camera excerpts. (d) Close-up of the second order diffraction region of the camera output (solid lines) superimposed with Raman spectra shown in (b) convolved with the PSF of the configuration.

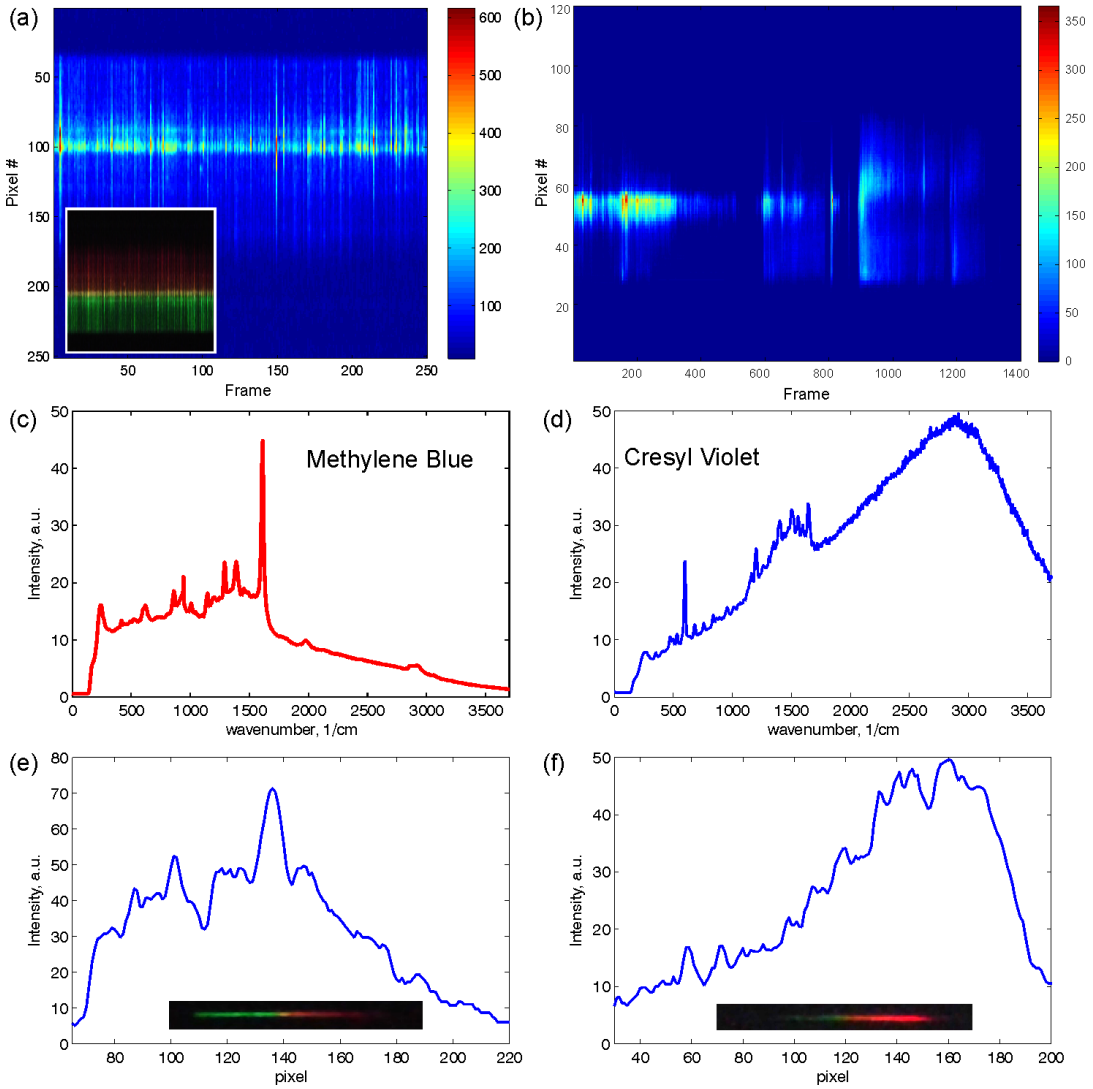

Figure 3-10. (a) False color coded excerpts from series of smart phone camera snapshot captures during blink events on the plasmonic substrate, in the spectrometer configuration (1 mW excitation at 532 nm). The spectral region is cropped, rotated and stitched for each frame. Inset shows actual camera color coding of the same data. Integration time per frame is ~ 1 sec. (b) False color coded excerpts from a video sequence recorded at 30 frames per second. Although video recording is at lower resolution, distinct spectral features during blink events can be observed (also see Supporting Video). The SERS spectra of plasmonic surfaces (30 nm HfO_2 thickness) were also recorded using the cooled CCD spectrometer, treated with 10 nM Methylene Blue solution in (c) and 1 µM Cresyl Violet solution in (d) using 100 µW excitation. Corresponding spectra are also captured using the smart phone camera as shown in (e) and (f). Insets show excerpts of the region of interest from actual camera captures in snapshot mode.

3.3. Probing Hot-electron Effects in Wide Area Plasmonic Surfaces Using XPS

3.3.1. Introduction

Plasmonic structures have attracted increasing attention in the recent years, enabling engineering of optical properties of surfaces[174]–[176]. Hot-electron effects (HEE) in plasmonic structures have been investigated as alternative mechanisms for solar energy harvesting and photo-detection[177]–[180]. HEE rely on transfer of hot carriers from one contact to another through a thin dielectric barrier and provide a semiconductor free route for the photoconversion. A relevant thin film structure is the metal-insulator-metal (MIM) configuration, where optical properties of the surface can be tuned through plasmonic resonances, while separately allowing engineering of carrier transfer and collection. Hot-electron transfer competes with thermalization in the conversion of the absorbed light into a DC or voltage[181], [182]. The transient electron energy distributions of metallic surfaces excited by light pulses are thermalized in short time scales ranging from 100 fs to 1 ps. Photoelectron emission with pulsed X-ray, UV, and visible light sources was used in investigation of non-equilibrium energy distributions of carriers on surfaces[183]–[185]. Such pulsed or pump-probe measurements provide direct information about carrier dynamics, however require advanced light sources. X-Ray Photoelectron Spectroscopy (XPS) was used to investigate surface photovoltaic and photoconductivity effects in nanocomposite surfaces without using femtosecond or picoseconds light or X-ray pulses[186]–[190]. Here, we extend such use of XPS to investigate HEE in plasmonic MIM structures. Laser excitation is used to illuminate the plasmonic surfaces (Figure 3-11a). The top metal of the MIM structures acts as the plasmonic antenna (metal nanodiscs or gratings/stripes) that provides enhanced optical absorption. Plasmonic enhancement leads to more efficient hot-electron generation. HEE result in surface photovoltages and are observed by comparing shifts of binding energy (BE) of the top metal islands for dark and illuminated conditions.

3.3.2. Results

A schematic description of the band diagram of a MIM surface under X-ray and visible light illumination is shown in Figure 3-11b. A top metal layer, Ag, is separated from a bottom metal layer by a thin dielectric barrier. Under X-ray illumination, the photoelectrons that escape from the top metal islands result in a positive current (J_x), charging the surface positively (Figure 3-11a). As a consequence, band bending occurs as shown in Figure 3-11b. In the absence of a compensating electron gun, the surface potential reaches steady-state due to the presence of direct (or trap assisted) tunneling current from the bottom metal to the surface, denoted by J_t in Figure 3-11b. When the surface is illuminated, absorption takes place at the top and bottom metals and the hot-electrons acquire an energy distribution, as shown by rectangles in Figure 3-11b on both sides of the junction. The electron mean free path is on the order of 20–30 nm, which is longer than the dielectric thickness. Therefore, hot-electrons with energies greater than the barrier height can be partially transmitted towards the top metal island where they are thermalized. This causes a negative shift of the observed BE of Ag. In contrast, hot-electrons generated in the top metal layer are not able to tunnel from the positively charged island.

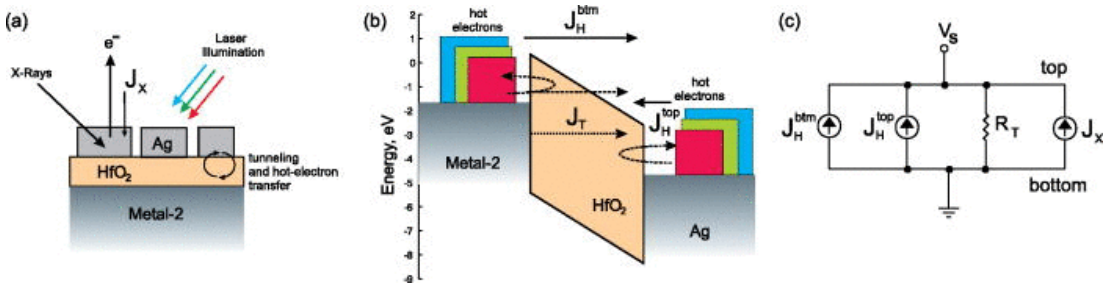

Figure 3-11. (a) Cross-section of the MIM surface during an XPS measurement with laser illumination. J_x represents the X-ray induced photoemission current into the vacuum. (b) The band diagram of the MIM junction under X-ray and laser illumination. Hot-electron energy distributions are shown with rectangles above the Fermi level, due to absorption of light in the top and bottom metal layers. (c) A simplified circuit model with various currents acting on the top metal layer which acquires a steady state voltage of V_s. Current J_T through the dielectric is modeled within a first order approximation by the resistor R_T.

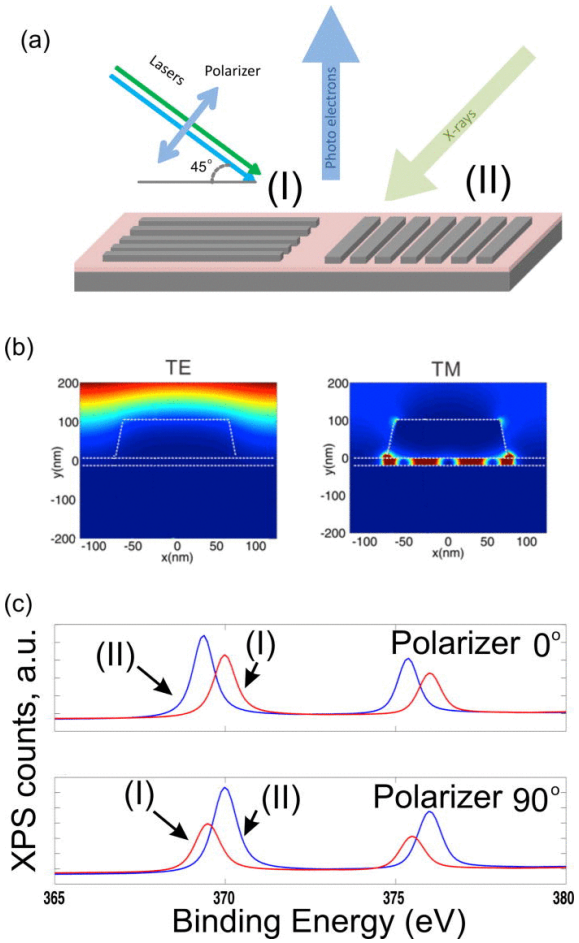

Figure 3-12. (a) Schematic description of the MIM grating structures used in polarization dependent measurements. (b) Calculated field profiles of the structures for TE and TM polarizations. Field enhancement is minimal for TE polarization, while plasmonic enhancement is present in the gap for TM polarization. (Scale bar 50 nm). (c) XPS spectra of the Ag 3d peaks acquired on gratings labeled as (I) and (II) for two polarizer orientations. As the polarizer is rotated from 0° to 90°, apparent binding energy shifts of the Ag $3d_{3/2}$ and $3d_{5/2}$ are observed for the gratings with different orientations. Each polarization excites only one of the gratings, for which the plasmonic modes are excited.

Recently, a nanostripe antenna was used to demonstrate plasmonic hot-electron current enhancement in MIM devices[52]. Polarization dependence of the enhancement was measured to show that optical absorption in the metal layers was dominated by plasmonic effects. Here, we demonstrate that HEE related surface photovoltages can be measured in similar MIM structures using XPS. Periodic MIM structures are fabricated using standard techniques. A 70 nm thick Ag layer is covered with 5 nm HfO_2, deposited using Atomic Layer Deposition (ALD) at 100 °C. Metal stripes are patterned by electron beam lithography and lift-off, resulting in 50 nm thick Ag stripes. The width, period, and length of the stripes are 150 nm, 250 nm, and 50 μm, respectively. The area of the patterns (250 μm^2) matches the XPS data collection spot size. In order to elucidate the plasmonic nature of

absorption in the metal layers, two grating structures perpendicular to each other are fabricated (Figure 3-12a). The MIM gratings feature wide angle and localized resonances in their optical response[191]. Field localization is calculated using Finite-Difference Time-Domain (FDTD) simulations for the TE and TM polarizations (Figure 3-12b). The plasmonic absorption P_a in the metal layers is resistive and location dependent and given by,

$$P_a(r) = \langle j(\vec{r}).E(\vec{r})\rangle = \frac{1}{2}\varepsilon_o\varepsilon_i|E|^2 \quad (3.1)$$

where $j(\vec{r})$ is the current density, ε_o is the vacuum electric permittivity, ε_i is the imaginary part of the relative electric permittivity of the metal, ω is the angular frequency, and E(r) is the local electric field. Total absorption can be calculated by integrating the absorbed power over the material boundaries. It is seen in Figure 3-12b that TE polarization does not excite the plasmonic mode and little or no field penetrates the metal within the gap region. In this case, hot-electron generation is minimal. In contrast, TM polarization excites the plasmonic resonance and enhances hot-electron generation in the top and bottom metal layers, within the regions facing the dielectric gap. The hot-electrons tunnel across the dielectric and disturb the charge equilibrium of the surface Ag layers and cause shifts in the apparent BE of Ag under 532 nm illumination at 40 mW/mm^2 (Figure 3-12c). The work-function of Ag is assumed to be 4.7 eV. The HfO_2/Ag conduction band barrier is 2.05 eV and this facilitates partial tunneling of hot-electrons for the used laser wavelengths 445 nm (2.77 eV), 532 nm (2.34 eV), and 650 nm (1.92 eV)[192]. The laser is incident at 45° and the polarization can be chosen to be parallel or at an angle to the surface plane by a polarizer. Under dark conditions, the Ag 3d peaks whose native binding energies are 374.35 eV (Ag $3d_{3/2}$) and 368.24 eV (Ag $3d_{5/2}$) are shifted towards positive energies (to 370.2 eV for the Ag $3d_{5/2}$ peak) due to X-Ray induced charging. When the polarization has a vertical component, a negative BE shift is observed for the grating that is perpendicular to the light propagation vector (from 370.2 eV to 369.1 eV for the Ag $3d_{5/2}$ peak, II in Figure 3-12c), while the gratings parallel to the excitation (I in Figure 3-12c) do not exhibit a significant shift. When the polarization is rotated, the responses of the periodic stripe antennas are reversed, highlighting the plasmonic origin of the observed shifts.

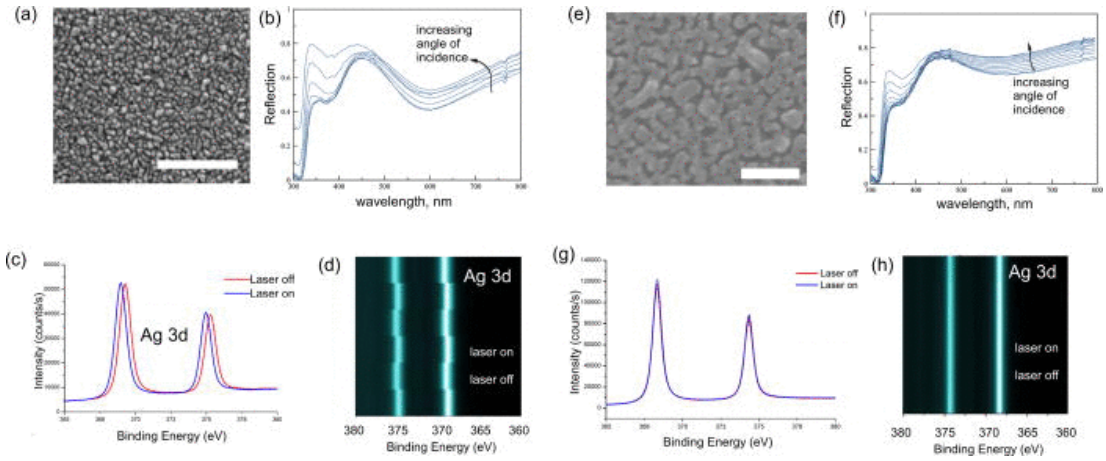

Figure 3-13. (a) Scanning electron micrograph of MIM surface fabricated by atomic layer deposition of HfO2 on Ag and self-organized formation of Ag nanoislands on HfO2 upon 3 nm thick Ag evaporation (Scale bar 250 nm). (b) Reflectance of the surfaces for incidence angles ranging from 20° to 80° shows a broad plasmonic absorption peak around 580 nm. (c) Photo-response of the MIM surface when illuminated by 532 nm excitation, measured by XPS. (d) Consecutive measurements of the XPS spectrum under dark and illuminated conditions exhibit repeatable differential shifts of the Ag 3d lines. (e)–(h) Same as in (a)–(d) except the top Ag mass thickness is 5 nm and a semicontinuous Ag film is formed instead of MIM nano-islands and no surface photovoltage is observed.

In order to demonstrate that HEE can be observed in wide area plasmonic surfaces, we use spontaneously organized MIM surfaces (Figure 3-13). The surfaces are fabricated by depositing 5 nm thick ALD deposited HfO_2 (at 100 °C) on an 80 nm thick Ag layer on silicon. A thin Ag layer of 3 nm mass thickness is evaporated on the HfO_2, which forms Ag nano-islands of average diameter of 30 nm and thickness of 10 nm[29], [191]. The surface exhibits a broad plasmonic absorption band around 580 nm (Figure 3-13b) and a repeatable photoresponse as measured by XPS, as shown in Figure 3-13c, d. When a semicontinuous film is formed on top of HfO_2 by depositing 5 nm thick Ag, no photoresponse can be observed (Figure 3-13e-h). The lack of surface photovoltage in the 5 nm Ag case is attributed to reduced plasmonic absorption and lower density of openings in the film where the excitation can couple to into modes between the metal layers.

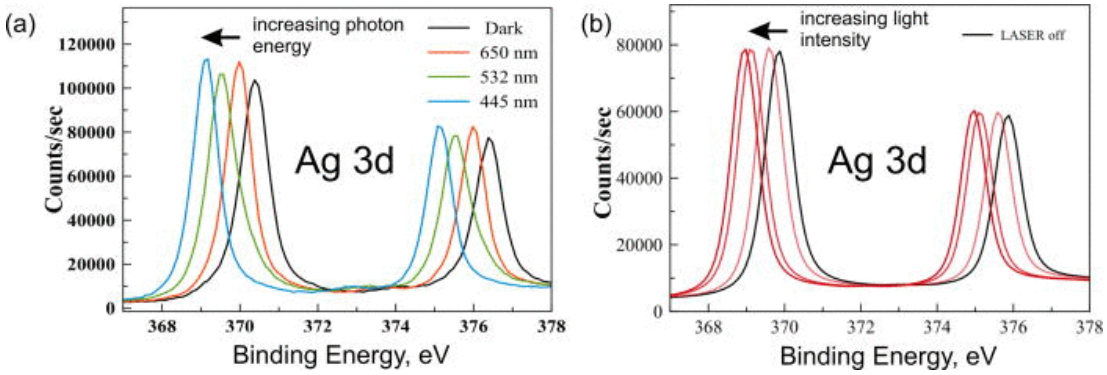

Figure 3-14. a) XPS spectra of the Ag 3d peaks measured on the MIM surface for dark and illuminated conditions, using lasers of 650, 532, and 445 nm wavelength, 20 mW power. The binding energies shift to negative due to hot-electron tunneling from the bottom metal to the top Ag island. Greater shifts are observed for increasing photon energy. (b) As the illumination intensity (445 nm) is increased from 5 to 20 mW, greater negative shift of the binding energy is observed which saturates at high intensities.

When the surface is illuminated by lasers of wavelength 445, 532, and 650 nm (22 mW/mm^2), the BE shifts on the 3 nm Ag surface are observed to be dependent on photon energy (Figure 3-14a). The observed binding energies are shifted from 370.2 eV for the Ag $3d_{5/2}$ under dark conditions to 369.01 ± 0.03 eV for 445 nm, 369.33 ± 0.03 eV for 532 nm, and 369.81 ± 0.03 eV for 650 nm excitation. The apparent BE is dependent on excitation power (Figure 3-14b) for 445 nm excitation at 5, 10, and 20 mW/mm^2. The shifts, with respect to observed BE under dark conditions (at 370.2 eV), are towards the native (grounded, bulk) BE of Ag $3d_{5/2}$ at 368.4 eV and increase with increasing excitation power density, saturating at high intensities.

The observations can be understood in terms of steady state currents, including hot-electron, tunneling, and photoemission currents. The IV characteristics of MIM junctions under illumination have been previously studied in the context of energy harvesting and photo-detection. If no other internal current sources are present, the open circuit voltage is independent of excitation power and is given by

$$V_{oc} = -\frac{h\nu - \varphi_e}{e}\left[1 - \frac{J_H^{bottom}}{J_H^{top}}\right] \tag{3.2}$$

where J_H's and V_{oc} are hot-electron currents and open-circuit voltage, $h\nu$ is the photon energy, φ_e is the barrier height, and e is the electronic charge. In the case of the MIM junction illuminated by light and X-rays, the photoelectron current J_x must also be included in calculation of the equilibrium condition. For $V_S > 0$, i.e., a net

positive charging of the top islands, the hot-electron currents can be written as $J_{btm}^{H} = -\gamma P_a^{btm}(h\nu - \varphi e)/h\nu$ and $J_{top}^{H} = \gamma P_a^{top} max(h\nu - \varphi e - eVS, 0)/h\nu$, where P_a^{btm} and P_a^{top} are the absorbed power at the bottom and top metal. Here, γ is a proportionality constant, which is included to approximately take into account the hot-electron density and velocity inside the metals. Assuming the surface is positively charged, i.e., $V_S > 0$, the circuit diagram in Figure 3-11c can be used to infer the steady state surface voltage V_S. For V_S larger than (Eph−φe)/e≈0.72 V for 445 nm illumination, all hot-electrons from the top metal are assumed to be reflected and J_c^{top}=0 . It was demonstrated that the dielectric behaves as a resistive layer under X-ray exposure, due to continuous ionization within the layer[193], [194]. Resistance of a 4 nm thick SiO_2 layer was determined to be 8.0 ± 1.0 MΩ in an XPS measurement specifically designed to extract electronic properties. We assume that the HfO_2 layer behaves similarly, like both a tunnel barrier for hot-electrons and a Poole-Frenkel conductor, i.e.,$J_t \cong V_S/R_t$. A more accurate quantitative analysis requires direct measurement of the photoelectron current or effective resistance of the HfO_2 layer (as done in Ref. [193]). The circuit model is still relevant for providing a qualitative understanding of the observed shifts. The steady state condition for $V_S > 0$ is

$$Jx + \gamma P_a^{top} \frac{max(h\nu - \varphi e - eVS, 0)}{h\nu} - \gamma P_a^{btm} \frac{(h\nu - \varphi e)}{h\nu} = \frac{V_S}{R_T} \qquad (3.3)$$

which predicts a surface voltage of $V_S = R_T J_x$ for dark conditions ($P_a^{btm} = P_a^{top}$=0). For the case of high power illumination (P_a^{btm}, P_a^{top}=0→∞), Equation 3.3 predicts a surface voltage $V_S = \frac{(h\nu - \varphi_e)}{e}[1 - P_a^{btm}/P_a^{top}]$, which is equivalent to the open circuit voltage given in Equation 3.3. Using $Jx \approx$ 72 nA/mm^2 measured for a similar XPS system, we estimate the resistance of the 5 nm thick HfO_2 layer as 25 MΩ over 1 mm^2 surface area. According to the data shown in Figure 3-14b for 445 nm excitation, 5 mW incident power causes a surface voltage shift of 256 mV over a 300 μm diameter illumination area, corresponding to a hot-electron current of 2.5 nA. The current is used to estimate the external quantum efficiency (EQE) as 11× 10^{-6} and responsivity as 500 nA/W, for the 300 μm diameter measurement area. The calculated responsivity compares favorably with the 75 nA/W measured for the same wavelength in stripe nanoantenna devices[52]. At higher excitation densities at

445 nm (Figure 3-14b), the surface voltage approaches 0.54 V, which would require a J_H^{bottom}/J_H^{top} ratio of 0.25 according to Equation 3.2.

3.4. Conclusion

In this chapter, we have developed a nano-particle based braodband and wide angle large area plasmonic meta-surface. The broad bandwidth is due to the excitation of electrical and magnetic plasmon modes. Then, we have used these surfaces for single molecule Raman spectroscopy and photo-detector applications. For the first time, we have imaged single molecule Raman event using a mobile phone's camera. We have also developed a contact free technique to probe hot-electrons using XPS.

Chapter 4

Exploiting Native Aluminum Oxide for Multispectral Aluminum Plasmonics

Aluminum, despite its abundance and low cost, is usually avoided for plasmonic applications due to losses in visible/infrared (IR) regimes and its inter-band absorption at 800nm. Yet, it is compatible with silicon complementary metal oxide semiconductor (CMOS) processes, making it a promising alternative for integrated plasmonic applications. It is also well known that a thin layer of native Al_2O_3 layer is formed on aluminum when exposed to air which must be taken into account properly while designing plasmonic structures. For the first time we report exploitation of the native Al_2O_3 layer for fabrication of periodic metal-insulator-metal (MIM) plasmonic structures that exhibit resonances spanning a wide spectral range, from the near ultraviolet (UV) to mid-infrared (MID-IR) region of the spectrum. Through fabrication of silver nano-islands on aluminum surfaces and MIM plasmonic surfaces with a thin native Al_2O_3 layer, hierarchical plasmonic structures are formed and used in surface enhanced infrared spectroscopy (SEIRA) and surface enhanced Raman spectroscopy (SERS) for detection of self-assembled monolayers of dodecanethiol (DDT).

Part of this chapter is published as;

Sencer Ayas, Ahmet Emin Topal, Andi Cupallari, Hasan Güner, Gokhan Bakan and Aykutlu Dâna,"Exploiting Native Al_2O_3 for Multispectral Plasmonic Structures", **ACS Photonics**,1,12,2014

4.1. Introduction

Recent advancement in plasmonics enabled the development of better performing plasmonic materials for the ultra-violet (UV)[195]–[199] and infrared (IR)[200]–[207] portion of the light spectrum. Typically gold (Au) and silver (Ag) are most common materials used to fabricate nanostructures to study novel plasmon-enhanced and enabled optical phenomena such as negative refraction,[208], [209] transformation optics,[12] surface plasmon sensors,[2], [59] surface enhanced Raman spectroscopy (SERS),[210], [211] surface enhanced infrared absorption spectroscopy (SEIRA),[64], [67] plasmon enhanced solar cells and detectors[14], [72]. Au has an internal band transition around 500nm which limits utilization of gold towards the UV portion of the visible spectrum[34]. Due to its chemically inert properties, stability and its tailorable binding to biomolecules, Au is widely used for surface plasmon resonance sensor applications working at visible wavelengths closer to NIR regime. Ag is considered as the optimal material for plasmonic applications in the visible spectrum due to its low loss compared to other metals[34]. However, Ag suffers from atmospheric sulfur contamination and oxidation[212]. Aluminum arises as a promising material for UV[213], [214] and deep UV plasmonic applications[16], [197], [198], [215], [216] owing to its high plasma frequency. Al has high losses from visible to IR range as well as an interband absorption around 800 nm which makes it less favorable as a NIR plasmonic material[34], [195], [217]. Still, localized plasmon resonances in Al have been demonstrated in several geometries, including nanoparticles,[213], [216], [218] triangles,[197], [214], [219] discs,[198], [220], [221] rods and nanoantennas[16], [222], [223]. Relative abundance of Al can be advantageous for the design of plasmonic absorbers in solar energy conversion, or

for inexpensive, disposable SERS and fluorescence enhancing substrates. Due to CMOS compatibility, Al plasmonic nanostructures would be optimal for silicon integrated optoelectronic applications, such as integrated biomolecular sensing,[3], [224] on-chip plasmonic nanoantennas, waveguides and interconnects[7], [208], [225]–[227]. Furthermore, the surface oxide of Al self-terminates at a thickness of 3−5 nm, forming a durable protective layer and preserving the metal, making this material a convenient choice for plasmonic applications that require durability[223], [228]. In this part of this thesis, we demonstrate exploitation of native oxide (NO) layer to form metal-insulator-metal (MIM) structures with resonances spanning a wide spectral range by enabling extreme mode confinement limit where multiple modes can be excited on the same structure due to ultrathin native oxide spacer layer. Nano-particle based MIM structures are demonstrated over large areas using a thin dewetting Ag top layer near the percolation threshold on naturally oxidized aluminum. The optical properties of such MIM structures is tuned by simply allowing a thicker native oxide layer to form by longer exposure to ambient conditions. The native oxide also allows simple fabrication of hierarchical plasmonic surfaces that exhibit simultaneous resonances in the visible and infrared regimes. Such hierarchical multispectral MIM structures feature simultaneously surface enhanced Raman spectroscopy (SERS) and surface enhanced infrared absorption spectroscopy (SEIRA).

4.2. Native Oxide Based Plasmonic Meta-surfaces

Periodic MIM structures on aluminum bottom layers are studied where the insulator is the native oxide layer which is naturally formed during the fabrication process that eliminates the need for depositing an insulator layer. Typically, fabrication process of native oxide based MIM (NO-MIM) structures requires multiple metal deposition processes (See Figure 4-1). After depositing the first Al

layer, the vacuum is broken for PMMA coating and e-beam lithography, which is accompanied by formation of a thin layer of Al_2O_3 on the surface of Al. The first set of plasmonic structures are formed through fabrication of nanodisc arrays on a silicon substrate coated with a thick layer of aluminum to demonstrate NIR resonance due to presence of native oxide. Figure 4-2a illustrates the formation of NO-MIM plasmonic surfaces with top nanodisc array. The fabricated NO-MIM structures show a resonance at NIR regime (Figure 4-2c) as characterized by a Fourier Transform Infrared Reflection (FTIR) microscope system equipped with a 15x Cassegrain objective. A knife edge aperture is used to limit measurement area to regions containing lithographically defined structures (100μm x 100μm). FDTD calculations show that a resonance emerges with the presence of a thin Al_2O_3 layer and blueshifts with increasing oxide thickness (Figure 4-2b). Evolution of the native oxide thickness is monitored by x-ray photoelectron spectroscopy (XPS) as shown in Figure 4-3. Uniformity of the oxide thickness is verified by XPS measurements at various spots on a continuous Al film. The thickness of the native oxide layer is also characterized by spectroscopic ellipsometer measurements. However, it is not possible to determine the exact value of the native aluminum oxide thickness due to the surface roughness of aluminum. Neglecting the surface roughness of Al which has 1.5nm of RMS value, the thickness of the native oxide layer is found to be 5.2nm after 24-hour exposure to air (20˚C, 35% relative humidity).

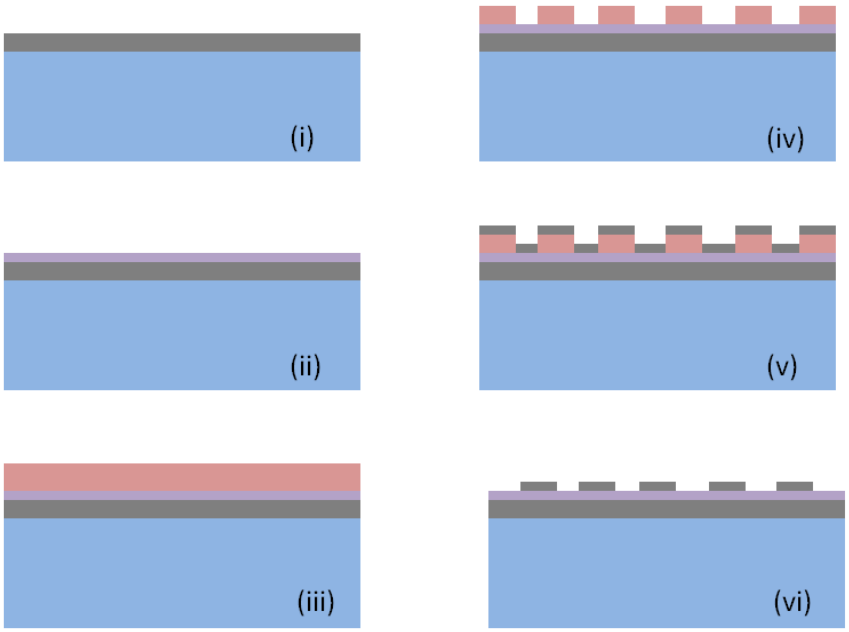

Figure 4-1. (i) Thermal evaporation of Al on silicon substrates. 3nm germanium is evaporated as an adhesion layer prior to Al deposition. (ii) Formation of a thin aluminum oxide (Al_2O_3) layer upon exposing the Al films to air for e-beam lithography. (iii) ~100nm PMMA is spin coated and annealed at 180˚C for 120 seconds. (iv) Patterns are formed using e-beam lithography. (v) 50nm of Al or Ag is evaporated. (vi) Lift-off process to form the final structures.

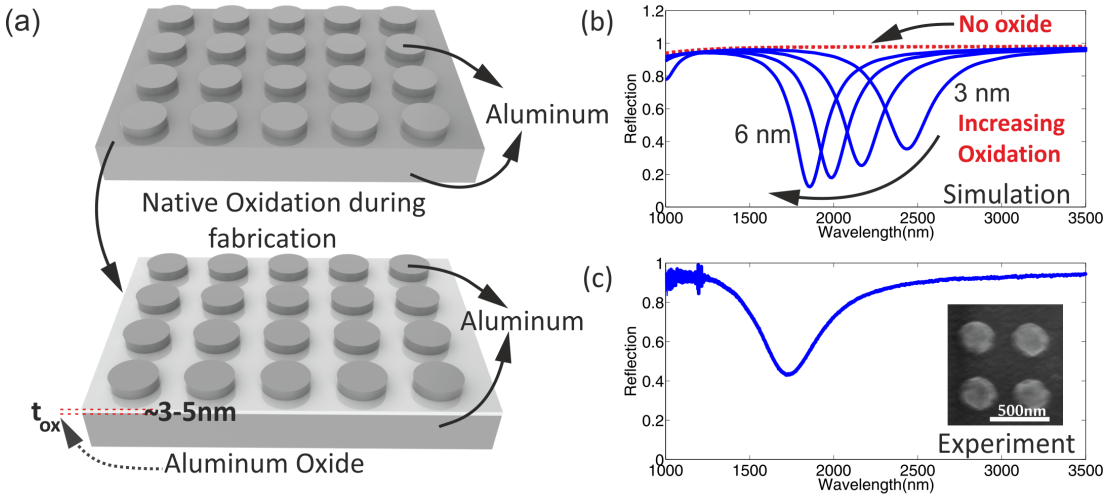

Figure 4-2. Verification of NO-MIM structures through observations of resonances in NIR. (a) Schematic of formation of NO-MIM surfaces during fabrication process (Top patterned layer height is 50 nm). (b) Simulated reflectance spectrum of NO-MIM structures for various Al_2O_3 thicknesses. While no plasmonic resonance is observed in the absence of native oxide, plasmonic resonances in NIR are observed due to the native oxide layer. Resonances blue-shift with increasing oxide thickness. (c) Experimental reflection spectra of the fabricated nanodisc NO-MIM structure. Diameter and period of the discs are 250nm and 400nm, respectively. (Inset) SEM image of the nanodisc array.

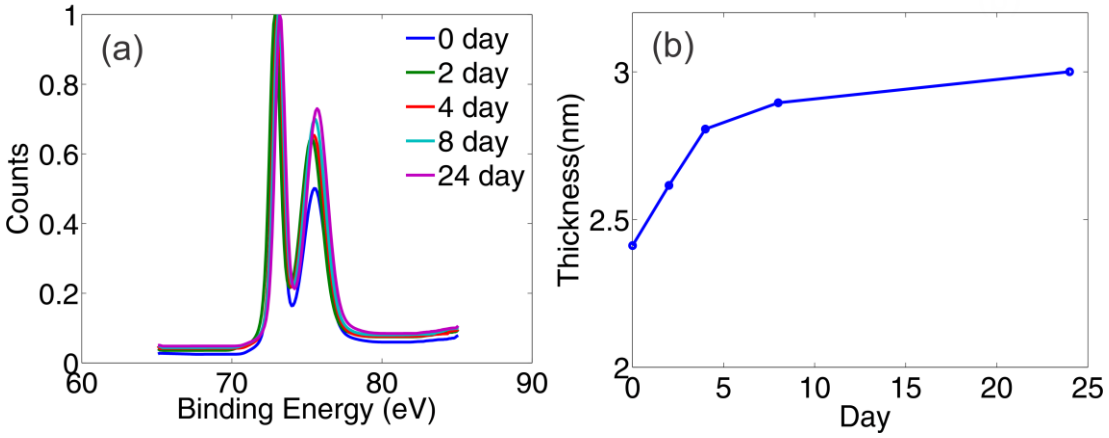

Figure 4-3. Characterization of the native oxide thickness over a time span of 24 days using XPS. (a) XPS spectrum of an aluminum film. High energy shoulder corresponds to the aluminum oxide peak. (b) Evolution of the calculated native oxide thicknesses.

In order to demonstrate the versatility and the tunability of NO-MIM structures, anisotropic structures that support resonances in the NIR and MIR regimes are investigated with long and short axes periods of 2μm by 500nm, respectively. Schematic of these structures is shown in Figure 4-4a. SEM images of the fabricated structures are shown in Figure 4-4b. Tunability of reflection spectra by increasing either long or short axis width is shown in Figure 4-4b. The reflection depths get weaker at these wavelengths due to weaker coupling of long wavelengths to the thin native oxide layer. In an MIM cavity the effective propagation constant and effective refractive index depend on the thickness of the dielectric film. The plasmonic resonances are strongly dependent on the period and the width of the surfaces. Within a first order approximation, the MIM mode of a patterned surface can be modeled as a standing wave that reflects back and forth from the edges of the top patterned layer, where individual resonators are assumed to be non-interacting. For closely spaced MIM resonators, coupling becomes important. Period of MIM structures affects the coupling of these individual nanocavities and typically for a constant MIM width, the interaction increases for smaller periods due to stronger intercavity coupling. Otherwise, period of an array of MIM resonators is assumed to be not dominant in determining the individual resonator response. In order to find the resonance wavelengths, one has to solve the characteristic equation given by,

$$W_{S,L}\frac{2\pi}{\lambda}neff = \pi - \varphi_{S,L} \tag{4.1}$$

where $W_{S,L}$ are the widths along the short and long axes, n_{eff} is the effective refractive index of the propagating mode and $\varphi_{S,L}$ is the phase term due to the reflection from the terminations. The effective refractive index, n_{eff}, is calculated by solving the Maxwell equations analytically for continuous MIM waveguide as shown in Figure 4-4d (See also Section 2.2). Figure 4-4c shows the calculated resonance frequencies of NO-MIM modes with experimentally measured resonance frequencies for varying widths along either short or long axes. An Al_2O_3 thickness of 5±0.5 nm is deduced from the model which agrees well with the ellipsometer measurements. It is observed that a dispersive dielectric function explains the observed resonance frequencies better than a constant dielectric function for Al_2O_3. Moreover, the cavity size of 1000nm x 310nm asymmetric resonators is about $\lambda^3/500{,}000$ assuming 5nm thick native oxide layer.

A simple MIM structure with 1D Al bar array offers tunable simultaneous resonances in both visible and NIR regime due to accommodation of the first and higher order modes when period and width of 1D structures are chosen properly (P=250nm). Only odd order modes are excited for normal illumination, due to symmetry. Even order modes can be excited at oblique angles due to the broken symmetry condition. Schematic and an SEM image of the fabricated 1D NO-MIM structures are shown in Figure 4-5a. Figure 4-5b shows the measured reflection spectra for the visible regime with increasing 1D structure width. The reflection spectra are measured with fiber coupled white light, polarized along the grating axis, using reflection from an aluminum mirror as the reference. Resonance wavelength red-shifts with increasing width (Figure 4-5). NIR reflectance spectra of the same structures are measured with the FTIR microscope using un-polarized NIR light source (Figure 4-5c). The resonance wavelength starts from 1200nm and shifts to 1400nm with increasing width. Measured visible and NIR reflectance spectra agree well with the simulations shown in Figure 4-5c,d. Simulations performed with neglecting NO show no distinct resonances which also indicates that the resonances are due to the presence of native oxide layer. Although almost zero reflection is observed in the simulations, the reflection depths for NIR measurements are smaller compared to the simulated values due to the use of un-polarized light. Surface roughness is neglected in the simulations which might account for some of the discrepancies such as resonance wavelength mismatch between experiments and simulations. Magnetic field distributions are simulated as shown in Figure 4-5f to

further understand the origin of the observed visible and NIR resonances. Magnetic field is confined to the oxide layer for both resonances. For the NIR resonance, first order or fundamental mode is excited. For visible, third order resonance is excited where there are three magnetic field peaks in the oxide layer ($\lambda_1 \cong 3\lambda_3$).

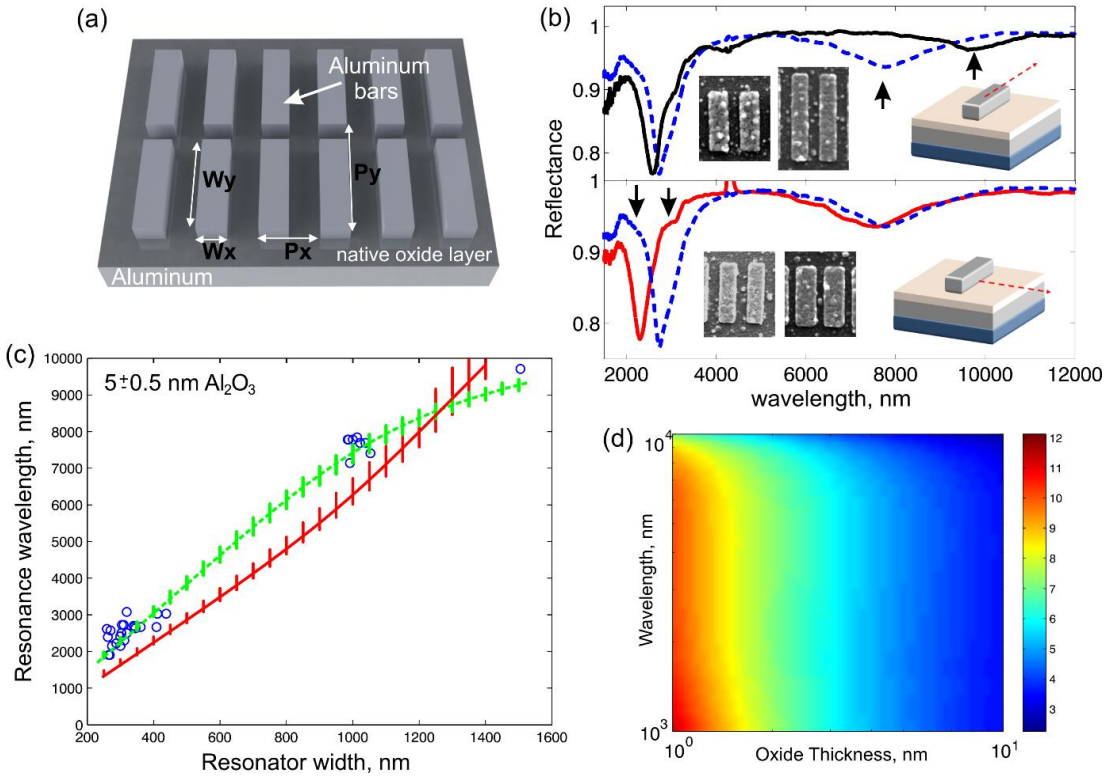

Figure 4-4. Resonance tuning in the NIR and MIR range using anisotropic Al bar arrays. (a) Schematic of asymmetric NO-MIM structures with nonidentical periods and widths along x and y directions to excite multiple modes in IR (Top patterned layer height is 50 nm). (b) Typical reflection spectra showing multiple resonances in the NIR and MIR range due to the asymmetry of the structures with P_x=500nm, P_y=2000nm and W_x=310nm and W_y=1000nm (black curve), 1500nm (blue curve) (top) and W_x=250nm (red curve), 310nm (blue curve) for W_y=1000nm (bottom). (Inset) SEM images of corresponding structures. Red dashed lines on the cartoon illustrations indicate the axis on which the structures' width is modified. (c) Experimentally observed resonance wavelengths as functions of the Al bar width either along the short or long axis (blue dots). Calculated resonances by treating the NO-MIM structures as Fabry-Perot (FP) resonators consisting of truncated waveguides (green and red curves). A better fit of the FP resonator model to the experiments can be achieved if the dielectric function of Al_2O_3 is assumed to be wavelength dependent (green curve), as opposed to a constant (red curve, n=1.6). Vertical lines on the curves are errors bars corresponding to 0.5nm uncertainty in the oxide thickness. (d) Effective refractive index of the waveguide forming the FP resonator as a function of Al_2O_3 thickness, using the wavelength dependent dielectric function.

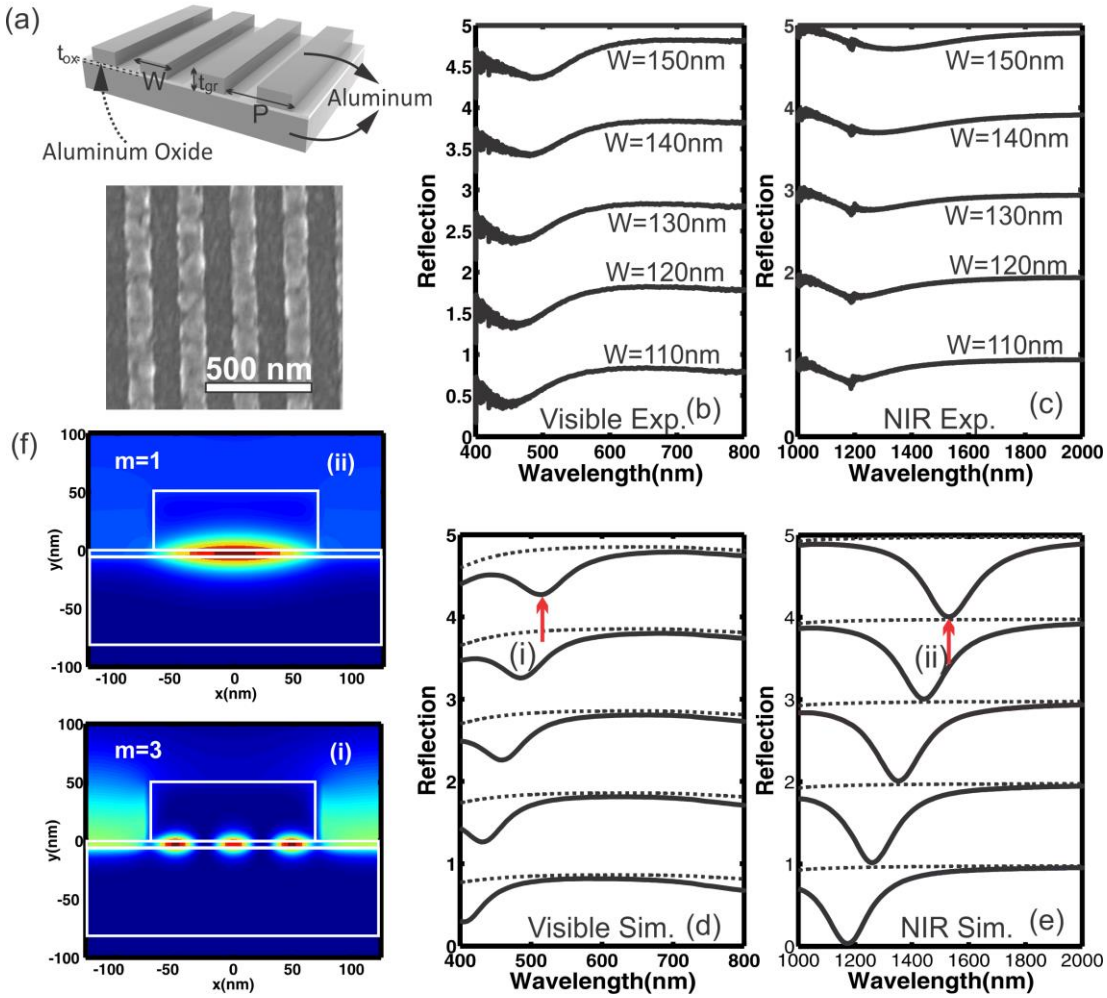

Figure 4-5. Simultaneous resonances in visible and NIR regime using 1D NO-MIM. (a) Schematic of 1D NO-MIM structures. t_{gr}=50nm and P=250nm. Experimental results showing tuning of resonance wavelengths as W changes between 110 and 150nm, (b) in the visible and (c) in the NIR regime. Simulation results for the experimented structures shown in (d-e) being in a good agreement with the experimental results. Each spectrum curve is shifted by 1 along y-axis for clarity. (f) First order (m=1) and third order (m=3) mode profiles corresponding to NIR (ii) and visible (i) resonances as indicated with arrows in (d) and (e). The even mode (m=2) is not observed for normal incidence. In the simulations 5nm of native oxide layer thickness is assumed.

4.3. Nanoparticle Based Large Area Surfaces

The studies presented in this part so far includes a lithography step to pattern the top layer which always yields a native oxide layer. To study the existence of native oxide layer, NO-MIM structures based on self-forming Ag nanoparticles on Al bottom layer is fabricated with and without exposing Al layer to air by breaking the vacuum. Such approach also offers larger area plasmonic surfaces compared to top down fabrication techniques such as e-beam lithography and focused ion beam

milling. For this study, Ag nanoparticles with an average size of 25 nm are obtained by evaporating 3nm Ag film (See Figure 4-6). Exposing Al surfaces to air for longer duration, hence forming a thicker oxide causes a blue-shift in the reflection spectrum (Figure 4-7a). Sequential deposition of Ag on Al films without breaking the vacuum does not show a resonance due to lack of an oxide layer. The effect of native oxide layer on Ag nanoparticle based MIM structures is simulated by modeling the nanoparticle film as an array of truncated cones as seen in Figure 4-7b. Increasing exposure time is captured through increasing NO thickness in the simulations which shows a blue-shift.

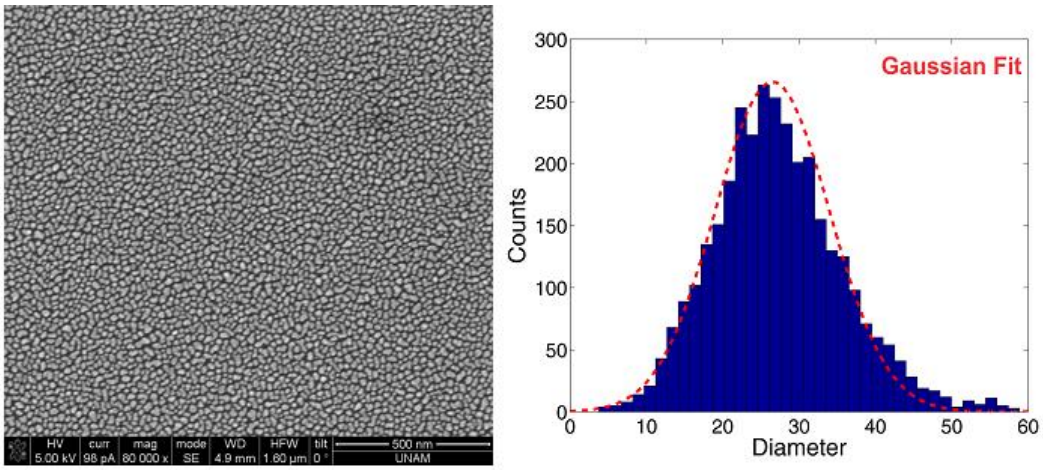

Figure 4-6. SEM images of Ag nanoparticles on silicon and their size distribution.

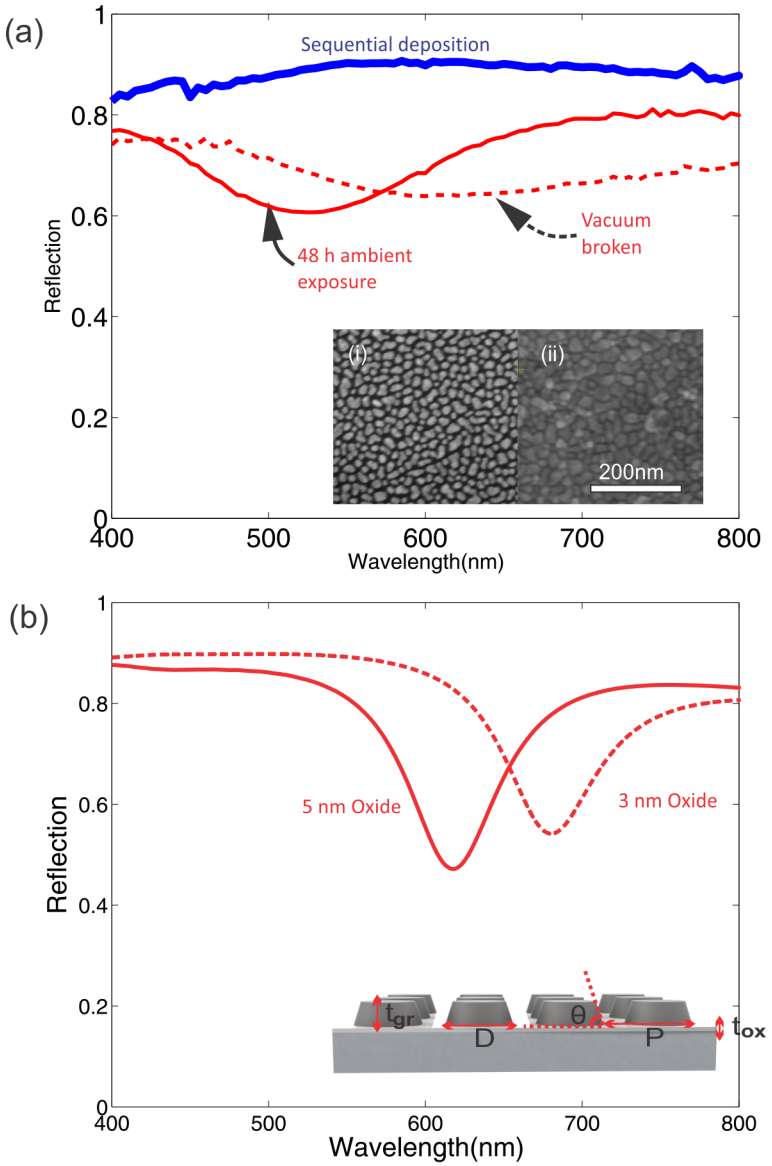

Figure 4-7. Nano-particle based large area NO-MIM structures. (a) Reflection spectra for Ag nano-particle based NO-MIM structures. Resonance blue-shifts if the time period between two deposition processes increases (dashed and solid red lines). No resonance is observed if the deposition of Al and Ag is done without breaking the vacuum (blue solid line). (Inset) SEM images of 3nm Ag on Si(i) and Al(ii). (c) Simulation results and simulated structure (inset) for t_{ox}=3nm and 5nm. Simulated structure is a periodic array of truncated cones with D=35nm, P=40nm, t_{gr}=20nm and θ=75 degrees

4.4. Surface Enhanced Infrared Absorption (SEIRA) Spectroscopy and Surface Enhanced Raman Spectroscopy (SERS) Using Hierarchical Plasmonic Surfaces

The studied plasmonic structures in this part of the thesis are used by sensing organic materials under Raman and infrared absorption spectroscopy which give information about the molecular structures and vibration spectra of molecules. The symmetry requirements in these two phenomena are different and they give complementary information about a molecule. Typically, high concentration of molecules is required in these techniques. On the other hand, SERS and SEIRA can magnify the signal levels up to 10^8 folds where resonant light structures are used to enhance field intensities enabling observation of the molecular vibrational signatures from few molecules. By taking advantage of multispectral characteristic of NO-MIM surfaces we demonstrate SERS and SEIRA on the same structures. In the experiments dodecanethiol (DDT) is used as the probe molecule. DDT cannot form a monolayer on aluminum. However, DDT molecular formation on Ag has been long studied[229]. Therefore, we first tried to demonstrate SEIRA on NO-MIM structures with a Ag top layer ($Ag/Al_2O_3/Al$). The resonance frequency of the structures is around 3500 cm^{-1} which is close to the C-H stretching of both DDT and PMMA (2930 and 2955 cm^{-1}). However, during fabrication resist residues, i.e. polymethyl methacrylate (PMMA) for e-beam lithography, are left on or under the patterned metals, resulting vibrational signatures coincide with those of DDT. Despite the presence of PMMA residues, the molecular signature of DDT after monolayer formation can be observed as shown in Figure 4-8. The number of molecules contributing to the SEIRA signal is estimated to be 4.6 femtomole on such periodic

structures. Less than 1 attomole sensitivity can be achieved by taking measurements from a single NO-MIM resonator, if a light source with very high SNR is used such as synchrotron light source.[230] The SEIRA enhancement factor is calculated as 2200 for these structures using a bare Ag film as the reference (Figure 4-9).

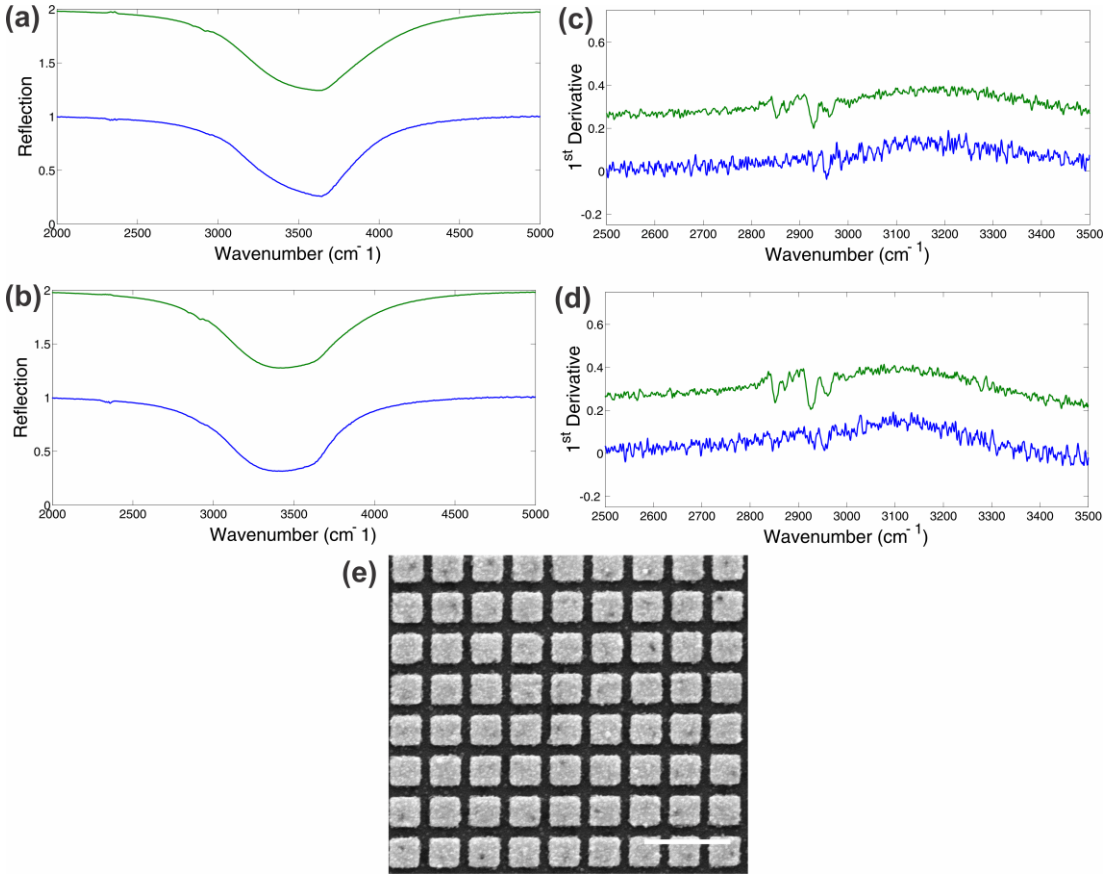

Figure 4-8. SEIRA on NO-MIM structures with patterned Ag top layer fabricated by e-beam lithography. Reflection spectra of these structures before (blue) and after (green) DDT monolayer formation for (a) $W_{x,y}$=300nm and (b) $W_{x,y}$=350nm. Periods along x and y directions are the same (P_x=P_y=500nm). (c) and (d) First derivative of the reflection spectra in (a) and (b), respectively. Molecular signatures of PMMA and DDT are more visible in the first derivative curves in (c) and (d) compared to the reflection spectra in (a) and (b). (e) An SEM image of the fabricated structures. (Scale bar: 1 μm).

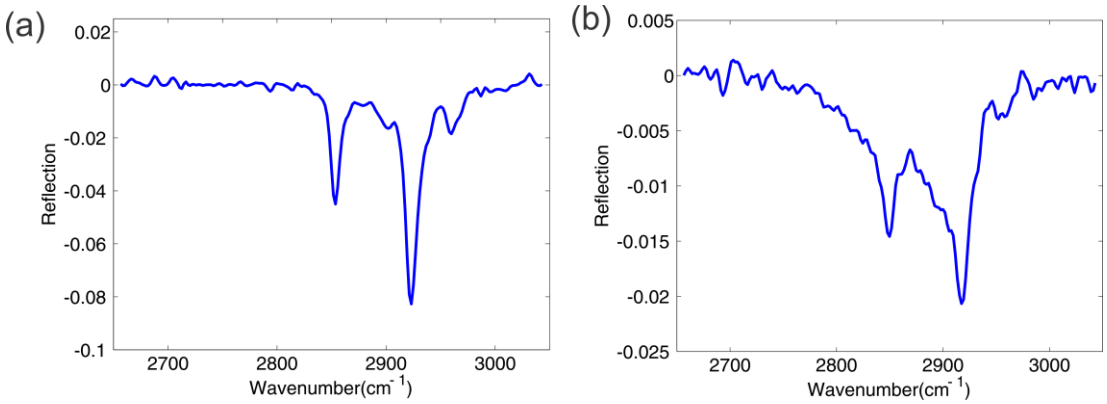

Figure 4-9. (a) Infrared reflection spectrum of the monolayer DDT on bare Ag mirror measured under Grazing Angle Illumination after background subtraction. (b) Infrared reflection of the monolayer DDT on the NO-MIM structures with Ag top layer after background subtraction.

In order to eliminate PMMA signatures from residues, the NO-MIM structures are treated in oxygen plasma. Since, oxygen plasma deteriorates top silver layer, a different type of resonator structure with multiple hierarchical MIM cavities is developed. Figure 4-10a illustrates the hierarchical NO-MIM (metal-insulator-metal-insulator-metal, MIMIM) structures developed for SEIRA measurements to eliminate the PMMA residues with oxygen plasma. Oxygen plasma does not harm Al, but increase oxide thickness on Al slightly. The fabrication steps of such structures are shown in Figure 4-11. First, an all-aluminum NO-MIM structure is fabricated by e-beam lithography with 500nm period and 350nm width that exhibits resonance in the IR (around 3500 cm^{-1}). Then the structures are cleaned in oxygen plasma, for PMMA residue removal. By evaporating 3nm of Ag on cleaned $Al/Al_2O_3/Al$ resonators, final MIMIM structures are obtained. Simulations show that depositing Ag nanoparticles on the Al NO-MIM structures change these structures' reflection spectra significantly in the visible regime, whereas it only causes a slight blue-shift in the IR regime (Figure 4-12). Figure 4-10b shows SEM image of the fabricated structure. Ag nanoparticles are formed both on and between the rectangular Al patterns. We first measured the FTIR reflection spectra of DDT

solution on bare Al surface to determine the molecular bands of DDT close to resonance of the fabricated structures as shown in Figure 4-10c. Then, FTIR reflection spectra are recorded in each step of the fabrication process as shown in Figure 4-10d, e. The resonance wavelengths do not change significantly after oxygen plasma and Ag deposition. The molecular signature of PMMA residues after liftoff can be determined before oxygen plasma. After oxygen plasma, PMMA residues are cleaned and no molecular bands for PMMA are observed. Following 3 nm Ag evaporation, the structures are treated with 1 mM DDT in ethanol solution for monolayer formation. The surfaces are washed with ethanol to remove unattached DDT molecules, and reflection spectra are recorded. Molecular signatures of DDT molecules can be identified without any post processing in the reflection spectra. The first derivative of each reflection spectrum is shown in Figure 4-10f, which better differentiates the DDT and PMMA signatures[231].

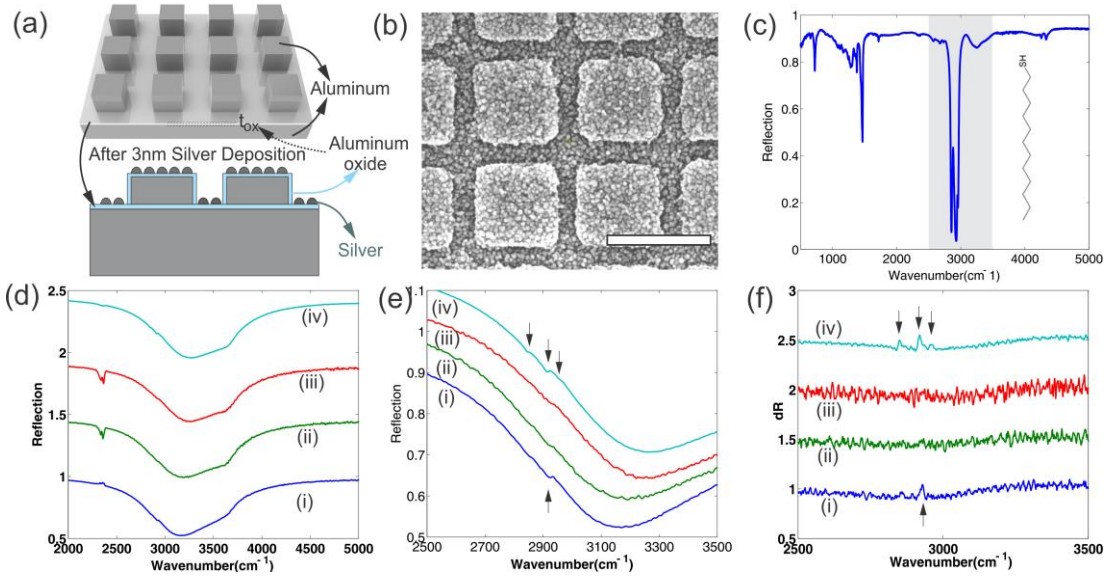

Figure 4-10. SEIRA detection of molecular monolayers on hierarchical NO-MIM structures. (a) Schematic of hierarchical NO-MIM structures before and after nanoparticle deposition with top patterned layer height of 50 nm. Periods and widths along x and y directions are the same, P_x=P_y=500nm and W_x=W_y=350nm. (b) SEM image of NO-MIM structures after 3nm Ag deposition (Scale bar: 500nm). (c) FTIR reflection spectrum of thick DDT solution on a

bare Al film. Region of interest is highlighted in grey. (Inset) Molecular sketch of DDT molecule. (d) FTIR reflection spectra of NO-MIM structures for: (i) just after fabrication of all Al NO-MIM structures, (ii) after plasma cleaning of PMMA residues, (iii) after the formation of hierarchical NO-MIM structures by 3nm Ag deposition, (iv) after DDT molecular monolayer formation on hierarchical NO-MIM structures. (e) FTIR reflectance between 2500 and 3500 cm^{-1}, and its derivative (f) for better visualization of stretching of monolayer DDT molecules. Arrows mark the DDT and PMMA signatures in (e). Molecular signatures (2930 cm^{-1} and 2955 cm^{-1}) of PMMA are observable before oxygen plasma cleaning. No distinctive bands are observed after oxygen plasma (ii) and Ag deposition (iii).

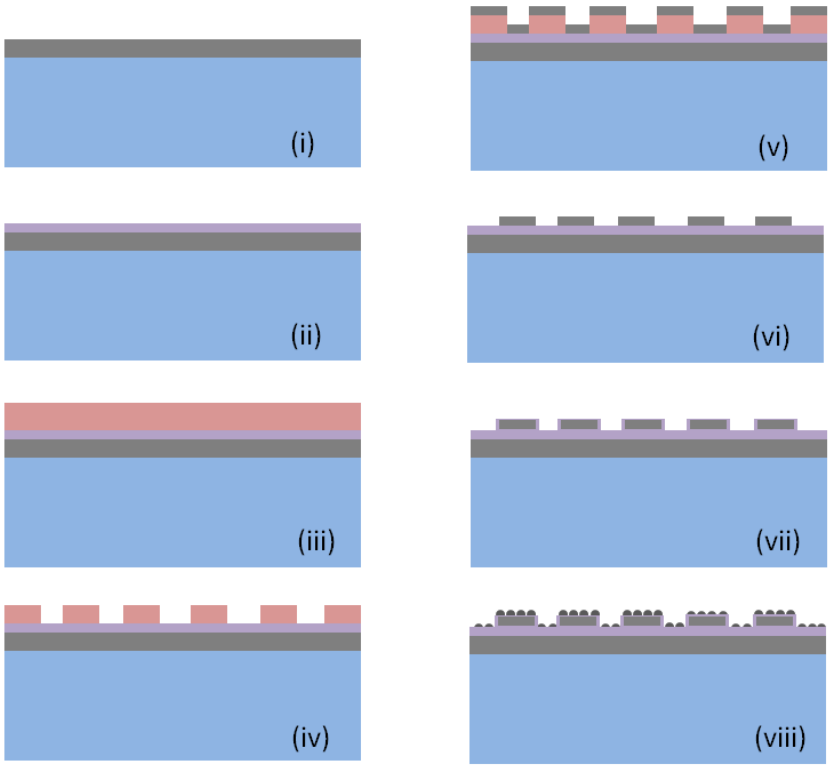

Figure 4-11. (i) Thermal evaporation of Al on silicon substrates. 3nm germanium is evaporated as an adhesion layer prior to Al deposition. (ii) Formation of a thin aluminum oxide (Al_2O_3) layer upon exposing the Al films to air for e-beam lithography. (iii) ~100nm PMMA is spin coated and annealed at 180˚C for 120 seconds. (iv) Patterns are formed using e-beam lithography. (v) 50nm of Al is evaporated. (vi) Lift-off process to form all Al MIM structures. (vii) O_2 plasma cleaning for PMMA residue removal and formation of a thin oxide film on the top Al structures. (viii) Formation of Ag nanoparticles through evaporation of 3nm Ag film.

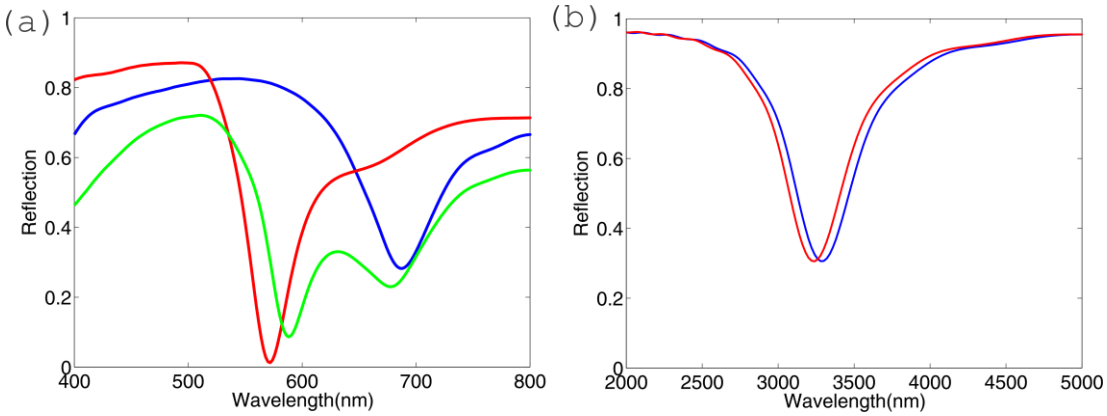

Figure 4-12. (a) Reflectance spectra for Ag nanoparticles-based NO-MIM (blue), all Al NO-MIM (red) and hierarchical NO-MIM (green) surfaces in the visible regime. (b) Reflectance spectra for all Al NO-MIM and hierarchical NO-MIM (red) surfaces in the MIR regime.

We have also used another method to fabricate PMMA-free NO-MIM surfaces with top Ag layer using focused ion beam (FIB) milling (Figure 4-13). Since the area that can be fabricated with FIB is smaller compared to e-beam lithography, the resonance contrast in the reflection spectrum from these surfaces is weak (Figure 4-13d). Other nanofabrication techniques can be used to eliminate the molecular signatures coming from the residues such as nano-stencil-lithography[231].

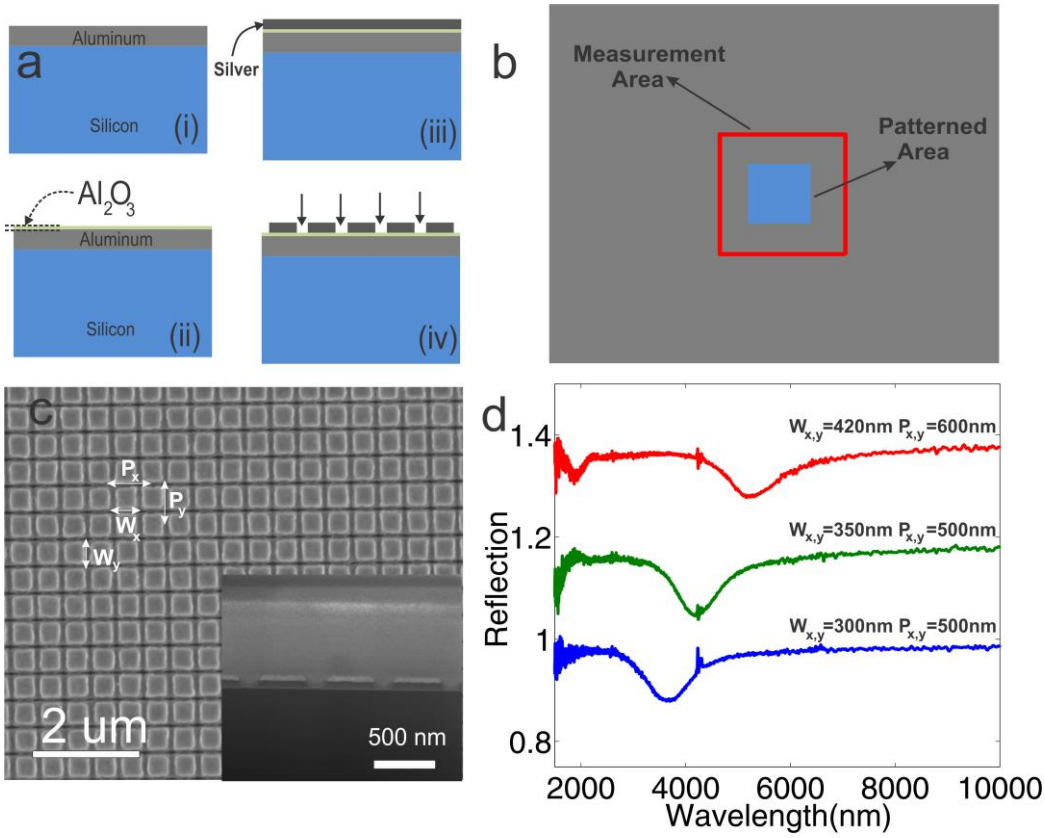

Figure 4-13. Characterization of NO-MIM structures fabricated using Focused Ion Beam (FIB) milling. (a) Fabrication steps for NOMIM structures: (i) Thermal evaporation of 100nm of Al on silicon substrates, (ii) formation of a thin aluminum oxide (Al2O3) layer upon exposing the Al films to air, (iii) thermal evaporation of 50nm of Ag, (iv) FIB patterning of the top Ag layer. (b) Measured (100µmx 100µm) area with respect to the fabricated area (50µmx 50µm). (c) Top-view and cross-section (inset) SEM images of FIB fabricated surfaces. (d) Reflectance spectra for the FIB fabricated surfaces with shown widths and periods.

The presence of closely spaced Ag nanoparticles on top of the hierarchical NO-MIM resonators with resonances in the visible and infrared presents an opportunity to perform SERS and SEIRA simultaneously. The Raman spectrum of a thick DDT solution on an Al covered Si substrate, recorded in 10 s using 13 mW excitation at 532 nm is shown in Figure 4-14a. In comparison, SERS data of DDT monolayers formed on hierarchical NO-MIM surfaces is shown in Figure 4-14b, collected using 0.5 mW excitation and 100 ms integration time. Despite shifts and changes in intensity of several lines, main features of the spectra are comparable to

Raman data shown in Figure 4-14a. No distinct spectral features of DDT are observed on bare Al films on Si (Figure 4-14b), since DDT does not stick on Al. It should be noted that, by coinciding the visible resonances of the NO-MIM structures with the resonances of Ag nanoparticle layer, an enhancement of the field intensities is predicted by computational study of MIMIM structures (Figure 4-14c, showing |E| distribution). While a small field enhancement is obtained for all Al NO-MIM structures around 532nm, Ag nanoparticle based NO-MIM structures show improved field enhancement due to better impedance matching of the resonances to free space modes, as well as due to reduced interparticle spacing. In contrast, hierarchical NO-MIM structures show further improvement in field enhancement, due to overlapping of the visible resonances of the Al and Ag island layers. Visible resonance is relatively weak, and accounts for the diminished reflectance over the hierarchical NO-MIM structures as shown in Figure 4-14d. The hierarchical NO-MIM structure however shows improved SERS performance as shown in the Raman map in Figure 4-14e. When the surface is illuminated by a defocused 532 nm excitation and inspected with a monochrome CMOS camera, blink events[232], typically associated with single molecule SERS are observed on the hierarchical portions of the sample (Figure 4-14f). Although FDTD calculations suggest overall SERS enhancement of $1.6x10^5$, we attribute the blinking spots to the presence of hot spots with greater field enhancement, due to the random nature of the top Ag nanoisland layer. We have estimated the enhancement factors as $2.2x10^3$ for SEIRA and 10^3 for SERS on our multispectral plasmonic structures. These values are comparable to the ones reported in the literature[63], [206], [207] and one order of magnitude smaller than the reported values in Ref. [233] .

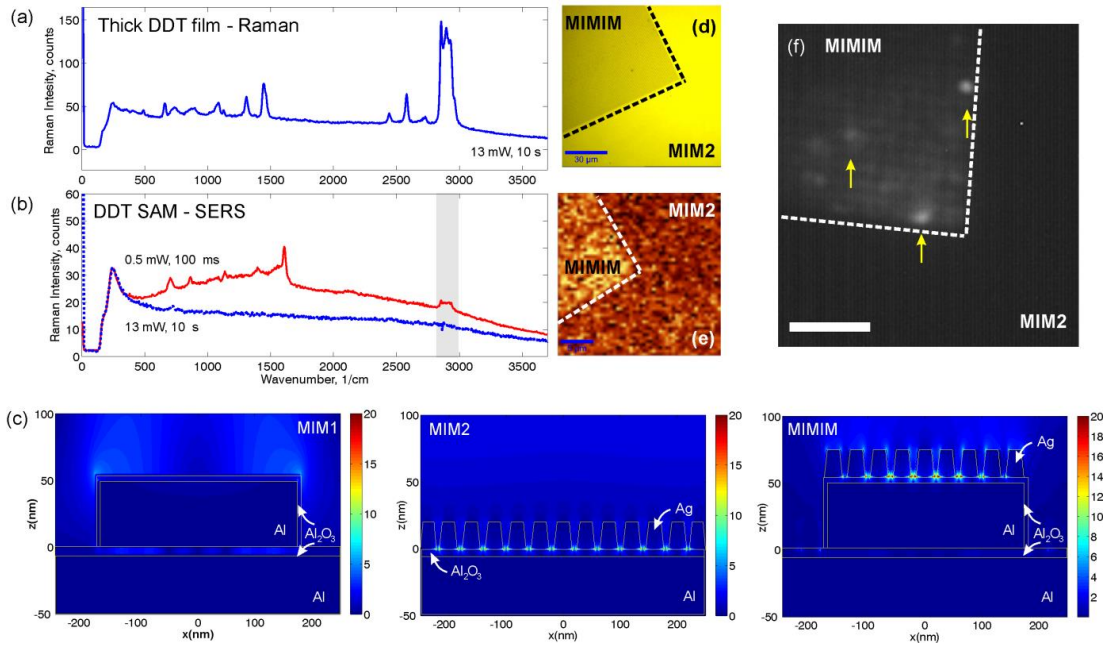

Figure 4-14. SERS detection of molecular monolayers on hierarchical NO-MIM structures. (a) Raman Spectra of a thick DDT solution on 80nm Al coated silicon. (b) SERS spectra of monolayer DDT on hierarchical NOMIM surfaces and an Al coated Si substrate. Integration time and laser power are 100ms and 0.5mW, respectively, for hierarchical NOMIM surfaces; where they are 10s and 13mW, for Al films on Si. (c) Simulated field profiles for all Al NO-MIM (MIM1), Ag nano-particle based NO-MIM (MIM2) and hierarchical NO-MIM (MIMIM) structures. (d) Optical micrograph of hierarchical NO-MIM surfaces. (e) SERS mapping of DDT on hierarchical NO-MIM surfaces. Brighter and darker regions emphasize hierarchical NO-MIM and nano-particle based NO-MIM structures, respectively. (f) Wide-field CMOS camera image of blink events on NO-MIM structures. Blink events are only observed on hierarchical NO-MIM structures.

4.5. All Aluminum Hierarchical Surfaces in the Infrared

So far we presented hierarchical surfaces utilizing Ag nano-particles on top of NO-MIM surfaces. Here, we present all-aluminum broadband hierarchical plasmonic surfaces using multiple Al and native Al_2O_3 layers. The hierarchical plasmonic surfaces are simply fabricated by sequential deposition and oxidation of Al films through breaking the vacuum of the physical vapor deposition system to expose the Al films to air. The fabricated hierarchical structures have multiple resonances in the MIR wavelengths as characterized by FTIR measurements and confirmed by simulations. Simulations of higher order hierarchical plasmonic surfaces show broader spectrum and reveal the importance of the native Al_2O_3 layers thicknesses. These structures have potential for applications that require durability, multispectral

characteristics such as surface enhanced spectroscopies, optical waveguides, color printing and thermal emitters.

The 3D schematics and top-down scanning electron microscopy (SEM) images of the fabricated hierarchical structures are shown in Figure 4-15. The top layer of these structures is designed to have arrays of squares with widths around 300nm and a period of 500nm along both x- and y-axis. The thickness of each top Al layer is chosen as 50nm. Typically the fabrication of such structures requires deposition of multiple dielectric and metal layers. Using Al eliminates the deposition of dielectric layers through the formation the native Al_2O_3. The thickness of the oxide layer depends on the exposure time of the Al surface to air. Since the native Al_2O_3 is ultrathin, even small changes in its thickness result in large shifts in the resonance wavelengths of the fabricated structures. The hierarchical Al surfaces are fabricated using e-beam lithography and multiple Al deposition steps. The fabrication steps are shown in Figure 4-15c and summarized here. First, silicon substrates are coated with 80nm thick Al using thermal evaporation following deposition of a thin layer of germanium (5nm) adhesion layer. The Ge layer also helps achieving smoother Al films as confirmed by AFM measurements. The first Al layer grows a thin Al_2O_3 layer when exposed to air. Then the samples are spin-coated with 250nm PMMA for e-beam lithography. Once the PMMA is patterned, 50nm thick Al is deposited. This first Al layer is exposed to air to form the second native oxide layer by breaking vacuum of the deposition chamber. Then the final Al layer is deposited and the final structures are formed using lift-off process. The area of the fabricated surfaces is 50μm x 50μm. The thicknesses of the top and bottom oxide layers are expected to be different. A Thermo K-Alpha monochromated high-performance X-ray photoelectron spectroscopy (XPS) system is used to characterize the thickness of the native Al_2O_3 layers.

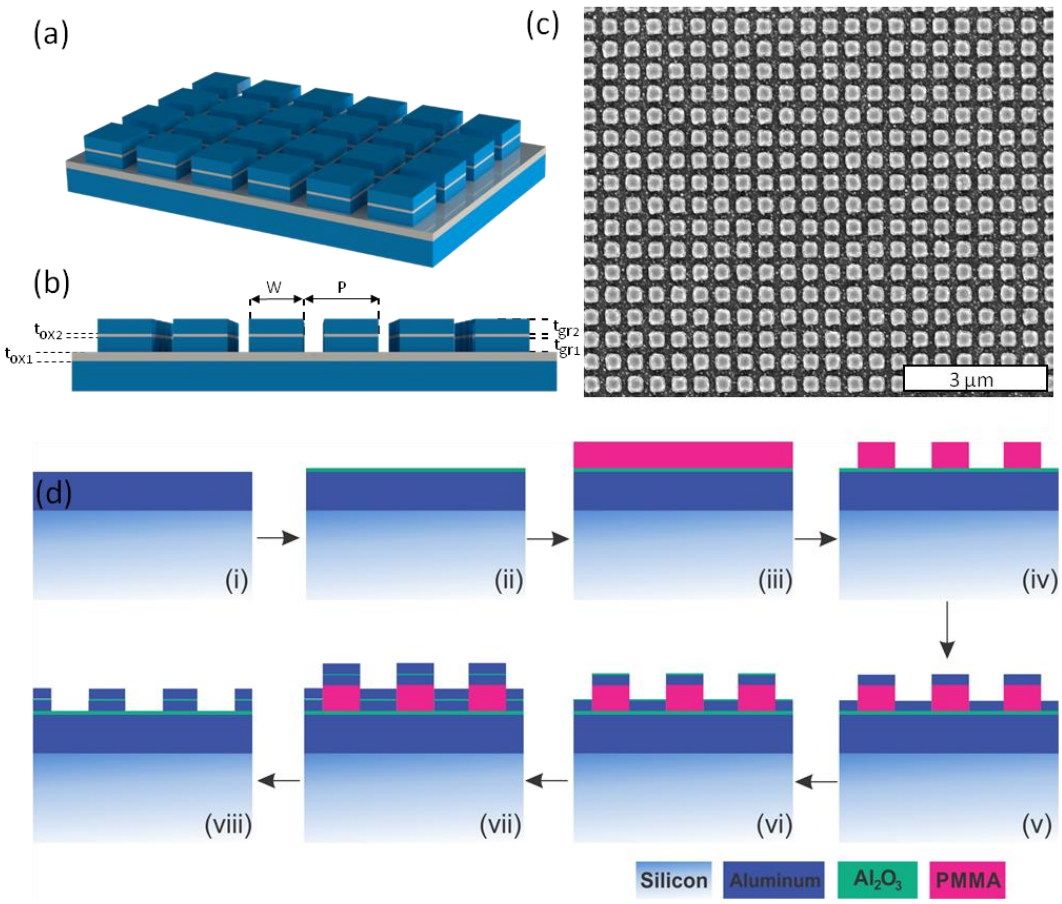

Figure 4-15. (a) 3D and (b) side view of the hierarchical aluminum surfaces. Top Al layer thicknesses (t_{gr1} and t_{gr2}) are 50nm. The thicknesses of the bottom and top oxide layers are denoted as t_{ox1} and t_{ox2}, respectively. (c) Top-down SEM image of the fabricated structures. (d) Fabrication of hierarchical Al structures. (i) Deposition of 80 nm thick Al. (ii) Formation of native Al_2O_3 after exposure of the Al films to air. (iii) PMMA coating. (iv) Pattering PMMA with e-beam lithography. (v) Deposition of the 1st 50 nm thick Al. (vi) Formation of the 2nd native Al_2O_3 layer after vacuum break. (vii) Deposition of the 2nd 50 nm thick Al layer. (viii) Lift-off process.

Depth dependent x-ray photoelectron energy spectra of the fabricated Al surfaces are shown in Figure 4-16. The depth dependent binding energy spectrum is obtained by etching the surfaces with ion gun and measuring the energy of the emitted photoelectrons from the etched surface. To characterize the thickness of the top oxide layer, the depth dependent binding energy spectrum for a thick Al film (80nm) on a silicon substrate is measured just in an hour after the deposition of the film (Figure 4-16a). The high energy peak corresponds to the aluminum-oxygen binding which indicates the formation of the native Al_2O_3 film. After 2nm of etch depth, the high energy peak reduces to 20% of its original intensity value. For 3nm of etch depth, the high energy peak almost disappears. Hence, the thickness of the native Al_2O_3 on a freshly deposited Al film is deduced to be 2-3 nm. Figure 4-16b shows the depth

dependent XPS energy spectra for the Al surfaces outside the patterned area after the fabrication of hierarchical Al structures. The high energy peak is stronger compared to the freshly deposited Al films. After 5nm of etching, the high energy peak reduces more than 80% and it only slightly changes for further etching. Hence, it is concluded that the thickness of the native Al_2O_3 on the Al films experienced the fabrication steps is about 5nm or more. The thicker native oxide on the bottom Al films is expected to be due to longer exposure to air and the chemical processes during the fabrication. The use of acetone, isopropanol alcohol and water might also affect the final thickness of the films.

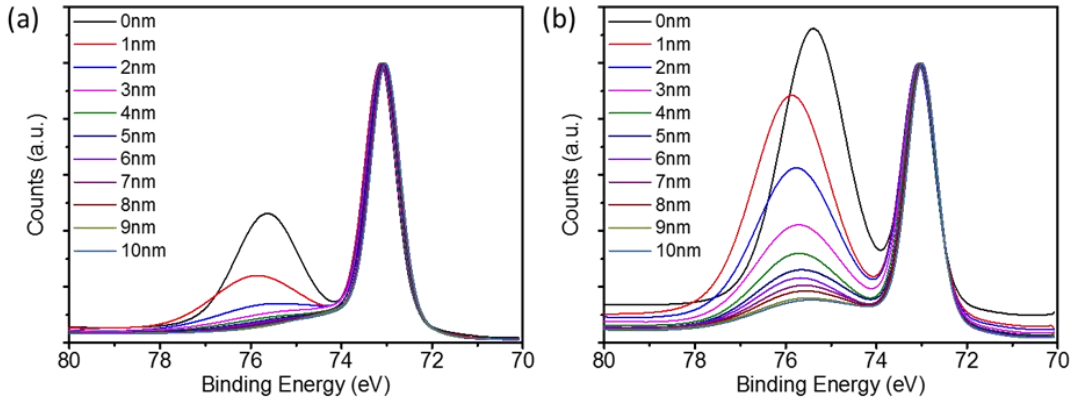

Figure 4-16. Depth dependent XPS characterization of Al surfaces with thin native Al_2O_3 on top. (a) Just after the deposition of Al films. (b) After the fabrication of hierarchical Al structures.

The reflection spectra of the hierarchical Al structures are characterized using Fourier transform infrared spectrometer (FTIR) equipped with a 15x Cassegrain objective in the MIR regime. Since the area of the fabricated hierarchical Al surfaces is 50 μm x 50 μm a knife edge aperture is used to collect light reflected from the patterned area. As the reference sample, an 80 nm thick Al coated silicon substrate is used. Owing to two different oxide thicknesses, two distinct MIR resonances are observed (Figure 4-17a). These resonances red-shift with increasing widths as expected. These structures are simulated using 2.5nm and 5nm thicknesses for the top and bottom oxide layers respectively (Figure 4-17b). The simulated spectral responses are similar to the experimental results, however the depths of the experimental resonances are weaker. This discrepancy might be due to surface roughness of the Al films which is not accounted for in the simulations. Moreover, the native oxide layer, which might be lossy by its nature, is assumed to be lossless in the MIR simulations (See Figure 4-18). The simulated electric and magnetic field

distributions are shown in Figure 4-17c corresponding to the resonances denoted with (i) and (ii) in Figure 4-17b. Since magnetic field is confined to the Al_2O_3 layers, the resonances are magnetic plasmon modes by its nature. Magnetic fields are confined to the bottom (5nm) and top (2.5nm) native Al_2O_3 layers for short and long wavelength resonances, respectively. The confinement of longer wavelengths to the thinner oxide layer can be intuitively explained by increased effective refractive index with decreasing oxide thickness, accompanied by a red-shift in the resonance wavelength[234]($\lambda_r = 2n_{eff}W$).

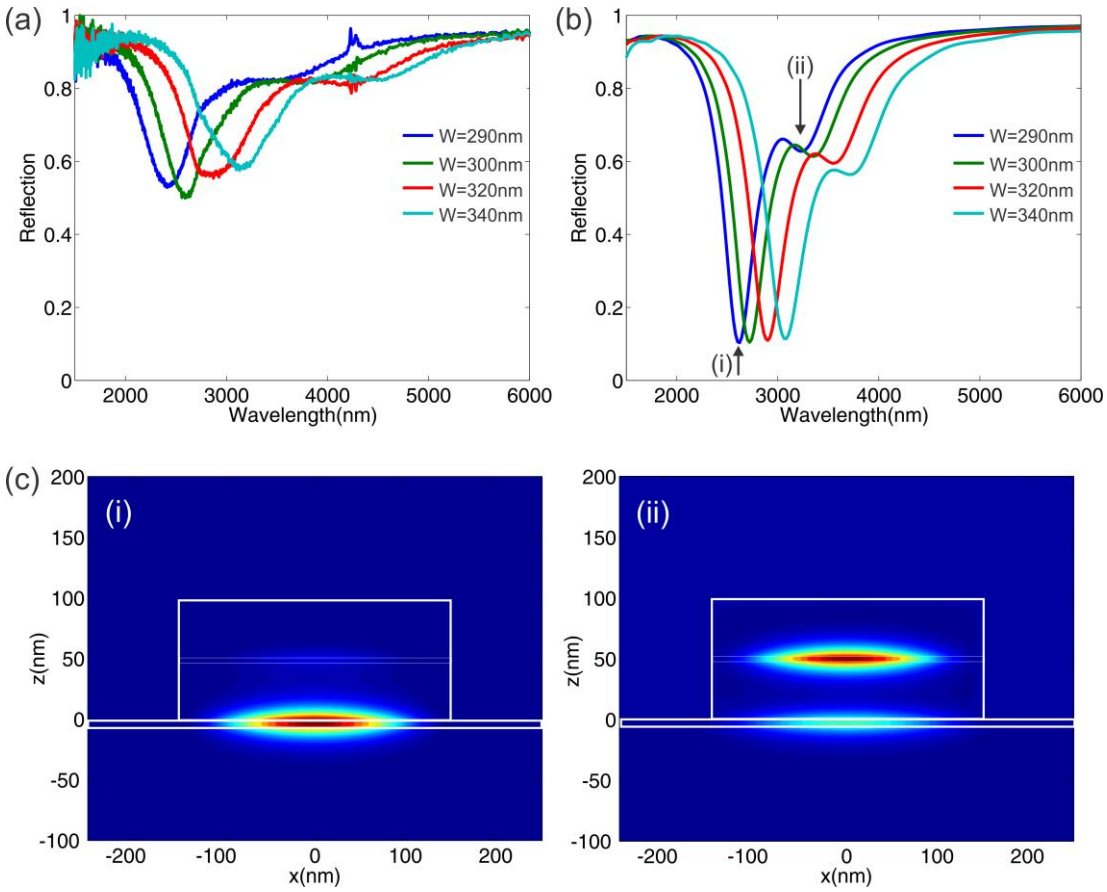

Figure 4-17. (a) Measured and (b) simulated reflectance spectra for W=290nm, 300nm, 320nm and 340nm (Period=500nm). (c) Magnetic field intensities for the resonances shown in (b).

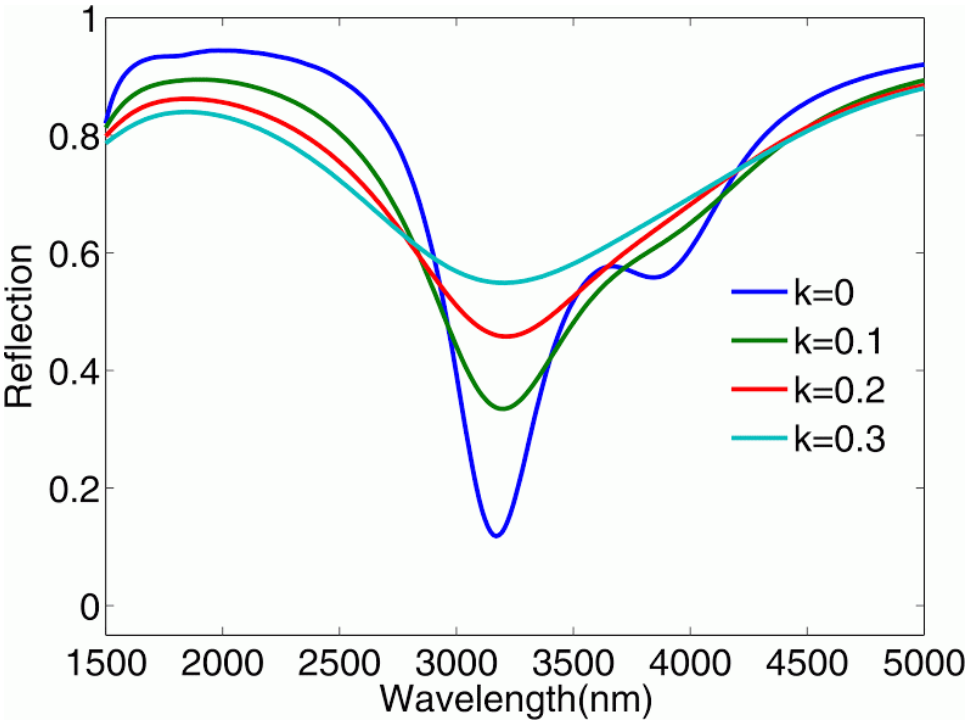

Figure 4-18. Simulated reflection spectra for the hierarchical MIM structure with two oxide layers assuming different extinction coefficients for the native oxide layer.

The effect of the top and bottom oxide thicknesses on the reflection spectra are further studied by varying these thicknesses in simulations (Figure 4-19). The resonance wavelengths shift drastically with sub-nm changes in the ultrathin oxide layers (2-5 nm) as shown in Figure 4-19 for W=300nm. When both oxide layers are neglected in the simulations, no resonances in the MIR are observed as expected (Figure 4-19a). If the thinner top oxide is neglected, only the short wavelength resonance is excited where it is confined to the bottom oxide layer. If the thicker bottom oxide is neglected, only the longer wavelength resonance is excited where the magnetic field is confined to top oxide layer. The effect of the native oxide layer on the longer wavelength resonance is investigated by varying the thickness of the top oxide layer in between 0.5nm and 3.5 nm for 5nm thick bottom oxide layer (Figure 4-19b). As the top oxide thickness decreases, the longer wavelength resonance red-shifts. As the thickness approaches the bottom oxide's value (5nm) the resonances start overlapping. As a result, the top and bottom oxide thicknesses have to be different to observe a multispectral response. If the oxide thicknesses are the same, only one mode is excited with stronger confinement of light into both oxide layers.

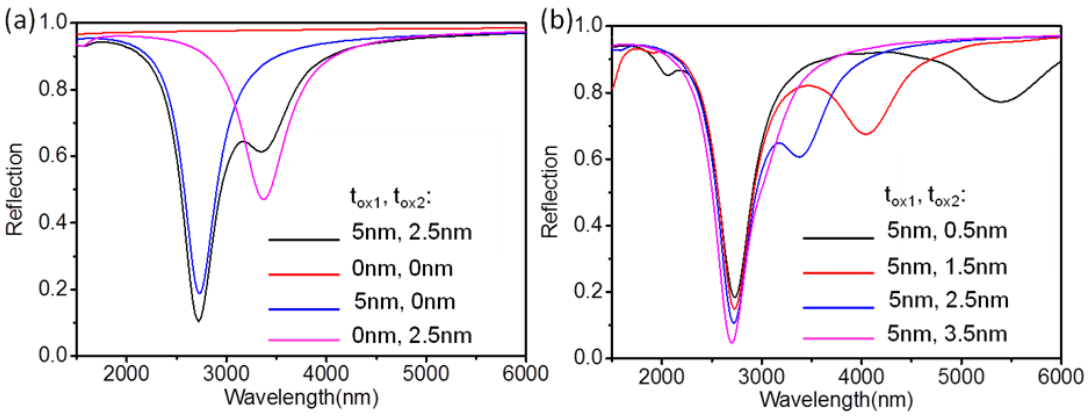

Figure 4-19. Simulated reflection spectra for (a) varying t_{ox-1} and t_{ox-2}, (b) varying t_{ox-2} with t_{ox-1}=5nm. W=300 nm, P=500 nm for all cases

The use of the native oxide as the spacer layer offers an easy fabrication route to realize higher order hierarchical resonator structures (Figure 4-20a). The optical response and field distribution of such structures with 3 and 4 oxide layers are studied using simulations. Since the resonance wavelength of an MIM resonator strongly depends on the thickness of the oxide layer, it is possible to excite as many modes as the number of oxide layers. Hence 3 distinct resonances are observed when 3 oxide layers with different thicknesses are used (Figure 4-20b). Similar to the previous simulation results with two oxide layers, when top two oxide thicknesses are chosen to be the same, only two resonances are observed. The study is repeated for 4 oxide layers and 3 different thickness combinations: 1) all thicknesses different, 2) two of the thicknesses are the same, 3) three of the thicknesses are the same resulting in 4, 3 and 2 distinct resonances, respectively (Figure 4-20c, d). As the number of layers with the same thickness increases, the bandwidth decreases, yet light couples into the MIM mode determined by the common oxide thickness more strongly.

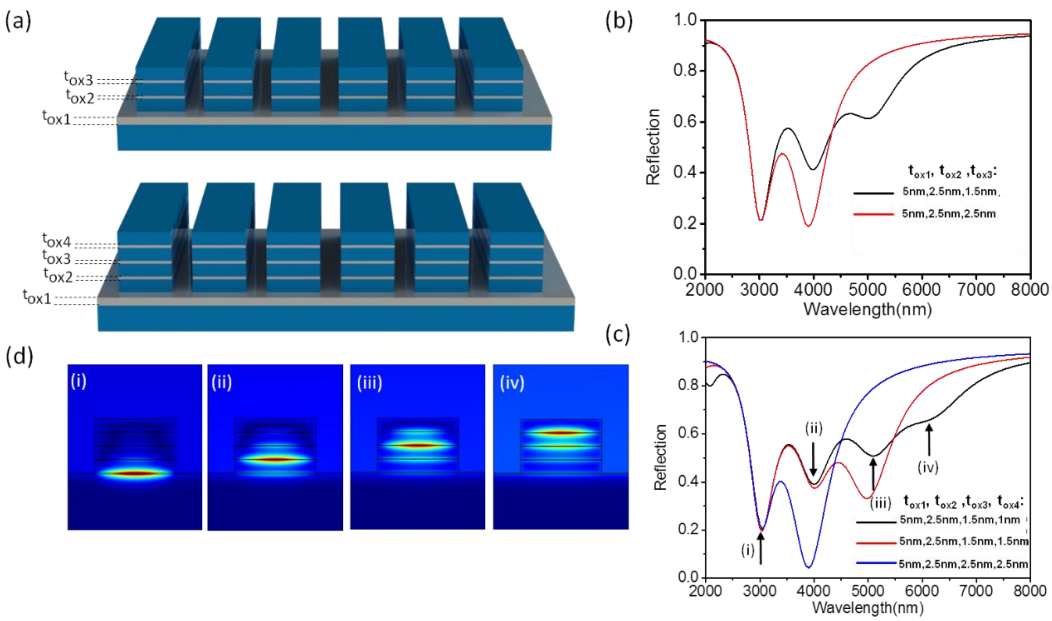

Figure 4-20. (a) 3D schematics of higher order hierarchical aluminum surfaces with multiple MIM resonators. Simulated reflectance spectra for structures with (b) 3, (c) 4 oxide layers. (d) Corresponding magnetic field profiles for the resonances shown in (c). The thickness of the top Al layers is 50nm, W=300nm and P=500nm for both geometries.

4.6. Conclusion

In conclusion, we have demonstrated the use of Al and its native Al_2O_3 to fabricate MIM resonators spanning the visible and IR wavelengths using top-down fabrication techniques. Large area plasmonic surfaces are fabricated by depositing thin Ag films near percolation threshold and the resonance wavelength is tuned by longer exposure of Al layer to air. We fabricated hierarchical plasmonic surfaces using multiple native oxide layers and the percolating Ag films and used these surfaces as SERS and SEIRA substrates for the detection of monolayer DDT. Then we have then improved the bandwidth of native oxide based plasmonic surfaces by sequential deposition and oxidation of Al films through breaking the vacuum of the physical vapor deposition system by exposing the Al films to air. Different resonances are confined to different native oxide layers with different thicknesses.

Chapter 5

Interference Coating Based Sensing Platforms

In the previous chapters we have designed and fabricated plasmonic structures to study novel optical phenomena such as SERS, SEIRA and plasmonic hot-electron effects. In this chapter, we shift our focus to interference coatings and their applications. We present two novel applications of these types of coatings. For the first application, we have developed a novel sensing platform in the IR. By utilizing phase change property of $Ge_2Sb_2Te_5$ (GST), tunable surfaces are fabricated and used for sensing ultrathin (~5nm) polymer films, self-assembled and protein monolayers. The performance of such surfaces is comparable or better than the plasmonic counterparts. As a second application, we propose and fabricate a sensing platform based on strong interference coatings. Unlike interference coatings, the thicknesses of such surfaces are about $t=\lambda/8n$. The sensing mechanism is based on the color change due to accumulation of bio-molecules on the sensing surface. Protein monolayer and bilayers are detected using these surfaces.

5.1. Thermally Tunable Ultrasensitive Vibrational Spectroscopy Platforms Based on Thin Phase Change Films

Infrared spectroscopy enables identification of materials through characterization of the vibrational modes of molecular moieties which are typically observed as small dips in the reflection/transmission spectrum. The vibrational mode signals increase with enhancement of electric field in the vicinity of the probe molecules. Plasmonic

surfaces with very high but localized field enhancements are typically used for sensing of small amounts of materials. Here, we propose using thin, unpatterned phase changing GST films deposited on wafer-scale metal ground planes with modest field enhancement factors ($|E|^2/|E_o|^2$~4) on the entire GST surface for ultrasensitive vibrational spectroscopy. Optical properties of the top GST layer are tuned by annealing the surfaces leading to tuning of the wavelengths at which electric field is enhanced. The ease of fabrication combined with ultra-sensitivity of these surfaces offer convenient optical platforms for the infrared vibrational spectroscopy of materials ranging from monolayers to μm thickness in size.

5.1.1. Introduction

Infrared vibrational spectroscopy is one of the widely used tools in chemistry[235] and biology[62], [236] for characterization of materials. The molecular signatures of materials can be sensed in the far-field signals (reflection or transmission spectrum). Current infrared measurement techniques such as Fourier Transform Infrared Spectroscopy (FTIR) require large amounts of molecules to collect significant information. Attenuated total internal reflection[237] and grazing angle objective[65] methods are commonly used to enhance the signals due to vibrational modes of small amount of materials to be sensed. The intensity of far-field molecular vibrational bands scale with square of local electric field intensity ($|E|^2$) as stated by the Beer's Law[238]. The wavelength dependent percentage of absorbed power can be estimated as

$$A(\lambda) = \int_0^{dV} \frac{4\pi n(\lambda)k(\lambda)}{\lambda} |E(r,\lambda)|^2 dV \qquad (5.1)$$

Thus, increasing near-field intensities in the vicinity of the probe molecules results in increased signal intensities of the vibrational modes. Recently, rough metal surfaces[58], patterned metal structures[239] and nanoantennas[240] have been demonstrated to enhance the vibrational modes of molecular monolayers in the infrared by increasing field intensities through exiting plasmons. This technique is widely known as Surface Enhanced Infrared Absorption Spectroscopy (SEIRA). In SEIRA, patterned plasmonic structures that have resonances close to the vibrational bands of a molecule are used to enhance the far-field signal intensities. Depending on the vibrational bands to be enhanced, the geometry of the plasmonic structure has to be tuned[67]. Smart designs with multispectral[233] responses have been demonstrated to enhance different infrared bands of a molecule.

Plasmonic surfaces used in SEIRA are usually fabricated using e-beam and optical lithography and multi-step processes, limiting the sensing area and increasing the cost. Although there are easier methods to fabricate plasmonic surfaces such as interference[26] and nanosphere lithography[241], they typically do not allow wavelength tunability over large bandwidths. Field enhancement factors ($|E|^2/|E_o|^2$) in plasmonic structures are very high but localized. The field enhancement calculations are based on the assumption that most of the contributing vibrational band signal comes from the high field enhancement regions. Although SEIRA enhancement of plasmonic structures are typically estimated to be in the range of 10^2-10^5, the far-field signal intensity changes due to vibrational bands of monolayers are typically small (<10%). Designs like pedestal shaped plasmonic antennas[242] have been proposed to increase the far-field signal through increasing the enhanced field area accessible to the probe molecules[243], [244]. Here we propose using entire surface of an optical platform with modest field enhancements (~4) similar to what is implemented in recent reports of electrically tunable graphene Salisbury screens[245]–[247]. The optical platforms are formed by depositing thin dielectric layers (Si and GST) on metal films which show optical resonances accompanied by field enhancements on the dielectric surfaces in the mid-infrared (MIR) regime. Thickness (t) of the lossless dielectric films (amorphous Si and GST) is determined as $\lambda_V/4n$ (λ_V: vibrational mode wavelength, n: refractive index). Crystalline GST exhibits a non-zero extinction coefficient (k) in the IR resulting in strong interference effects[74] ($t< \lambda_V/4n$). Very thin (5 nm) films of poly(methyl methacrylate) (PMMA) and monolayers of bovine serum albumin (BSA) and octadecanthiol (ODT) molecules are used to test the performance of the surfaces. The studied surfaces are proposed as highly-sensitive, angle-independent infrared spectroscopy platforms which can be fabricated with low cost, very fast owing to the simple structure with two continuous layers, without patterning, on large-area rigid or flexible substrates, e.g., Al foil, and can be tuned by varying the thickness or phase of the dielectric layer. Unlike plasmonic surfaces used in SEIRA, the proposed surfaces do not exhibit Fano type vibrational bands due to the strong coupling of plasmonic and vibrational modes. Hence, complicated post-processing methods required for plasmonic structures are eliminated using these surfaces.

5.1.2. Results

A very-thin (~nm) suspended layer of a material enables the most basic infrared spectroscopy method as the vibrational modes can be observed as small dips in the transmission spectrum with an electric field enhancement factor of ~1 (Figure 5-1a(i),(ii)). For a ultrathin absorbing layer, the Equation 5.1 becomes $A(\lambda) = 4\pi n(\lambda)k(\lambda)/\lambda|E(\lambda)|^2 t$. The far-field signals of the vibrational modes are expected to be detectable but small (Figure 5-1a (iii), (iv)). For 1732 cm^{-1} k~0.5, thus for t=5nm intensity change in the far-field transmission is about 1%. This signal intensity change is in the order of signal intensities (1-5%) obtained with plasmonic surfaces. Achieving a suspended layer of any material, e.g., 5 nm PMMA, over a rather large area (~mm), however, is not possible. A thin (~50 nm) suspended membrane, such as Si_3N_4, can be used to address this problem while introducing other issues such as limited area, fragility of the substrate, and observation of strong signals from vibrational bands of the membrane material. The IR transmission measurements of a 5 nm PMMA coated 50 nm thick Si_3N_4 membrane show detectable but small signal for the major PMMA band at 1732 cm^{-1} and very strong signals (~40%) for the Si-N vibrational bands (Figure 5-3).

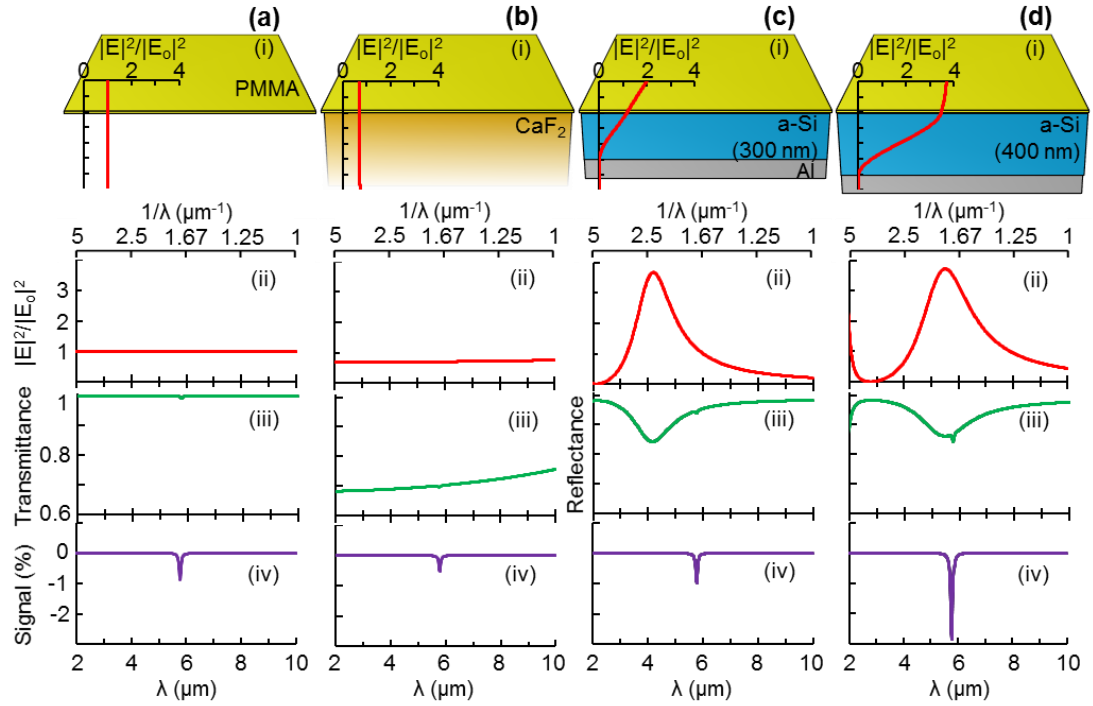

Figure 5-1. Sensing performance of various optical platforms. 5 nm PMMA (a) suspended in air, (b) on semi-continuous CaF_2 substrate, (c) on 300 nm a-Si/Al surface, (d) on 400 nm a-Si/Al surface. (i) Simulated electric field enhancement profiles on cartoon illustrations at λ: 5780 nm (1/λ: 1732 cm^{-1}). (ii) Simulated electric field enhancement factors on the surface of each structure, (iii) far-field signal (transmittance/reflectance) spectra, (iv) signal from the major PMMA band. The signal is the difference between the far-field signals w/ and w/o PMMA layer. Measured optical properties of PECVD deposited a-Si are used for the simulations (n: 3.3 in the IR). Optical properties of PMMA are fitted to a Lorentzian oscillator (Figure 5-2) centered around 5780 nm.

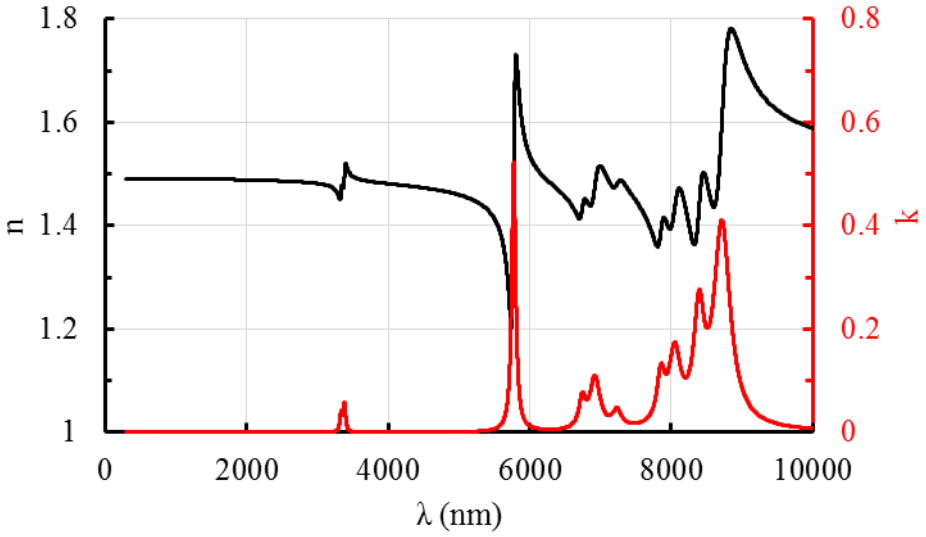

Figure 5-2. Measured refractive index and extinction coefficient of PMMA. The optical parameters are extracted using spectroscopic IR ellipsometer measurements of 130 nm PMMA film on a Si wafer using the Lorentzian oscillator model for each PMMA band. Only the vibrational band at 5780 nm is used for the simulations.

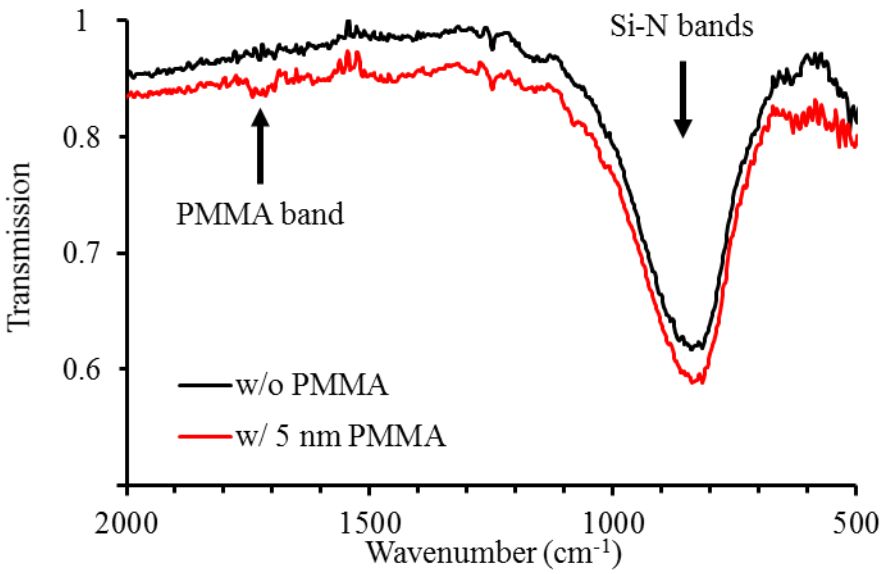

Figure 5-3. Transmission spectra of 50 nm thick suspended SiN_x membranes with and without 5 nm PMMA layer. The vibrational band of SiNx is observed as a significant dip in the transmission spectra. The signal from the PMMA band at 1732 cm^{-1}, however, is small.

A thick IR transparent substrate, such as CaF_2 or MgF_2, can also be used to detect the vibrational bands on the transmission spectrum (Figure 5-1b) with an enhancement factor of ~0.7 on the surface. Although the vibrational mode signals are expected to be smaller compared to the suspended layer configuration, such IR substrates have the advantages of strength and large area. Alternatively vibrational mode signals can be detected on the reflection spectrum using a reflective substrate such as metal-coated Si wafer. Electric field enhancement factor increases from almost zero on the metal surface to 4 at a distance quarter wavelength ($\lambda/4$) away from the surface[245], [246]. The vibrational band signal is expected to be maximized when the probe material is $\lambda_V/4$ away from the metal surface where the enhancement factor is ~4. While this can be achieved by forming a thin membrane over a metal surface, the most trivial way is using a dielectric coated reflective layer. The enhancement factor at the air-dielectric interface in this case is given as

$$\frac{|E|^2}{|E_o|^2} = \left(\frac{r_{12} + r_{23}e^{2i\beta}}{1 + r_{12}r_{23}e^{2i\beta}} + 1\right)^2 \tag{5.2}$$

where $r_{xy}=(\tilde{n}_x-\tilde{n}_y)/(\tilde{n}_x+\tilde{n}_y)$, $\tilde{n}$ is the complex refractive index, $\beta=(2\pi/\lambda)\tilde{n}_2 t$, and layers 1, 2, and 3 are air, dielectric, and metal, respectively. The total reflection coefficient (r_t) is 1 when r_{12} is zero (n_2=1) and decreases with increasing n_2 ($-1 < r_{12} < 0$). Using a relatively high refractive index material such a-Si requires smaller thickness but slightly reduces the enhancement factor to ~3.7. If the dielectric thickness is not

exactly $\lambda_V/4n_2$, the vibrational mode signal can still be sensed owing to non-zero field enhancement (Figure 5-1c). The signal intensity is maximized for $t= \lambda_V/4n_2$ (Figure 5-1d). The enhancement of electric field extends up to $\lambda/4$ above the dielectric surface, enabling sensing of thicker probe materials, e.g., cells, which is typically not possible for plasmonic surfaces due to low spatial extent (<100 nm) of field enhancements[248]. For a certain dielectric material of $\lambda_V/4n_2$ thickness, the enhancement factor reaches its theoretical limit of 4 for $r_{23}=-1$ which is achieved for a perfect electrical conductor (PEC) layer (Figure 5-4). Hence the more closely a metal behaves like a PEC in the MIR, the higher the enhancement factor is. Simulation results for various metals, including Al, Au and Ag, show that Al and Au can achieve the highest enhancement factors (~ 3.7) in the MIR for a-Si dielectric layer. Hence, Al is chosen as the ground plane material owing to its low cost, abundance and CMOS compatibility for the fabrication of the surfaces. Using Al ground planes enables comparing IR absorption and sensing performances of these surfaces to those of based on thin Al foils which are cheap, bendable and large area substrates.

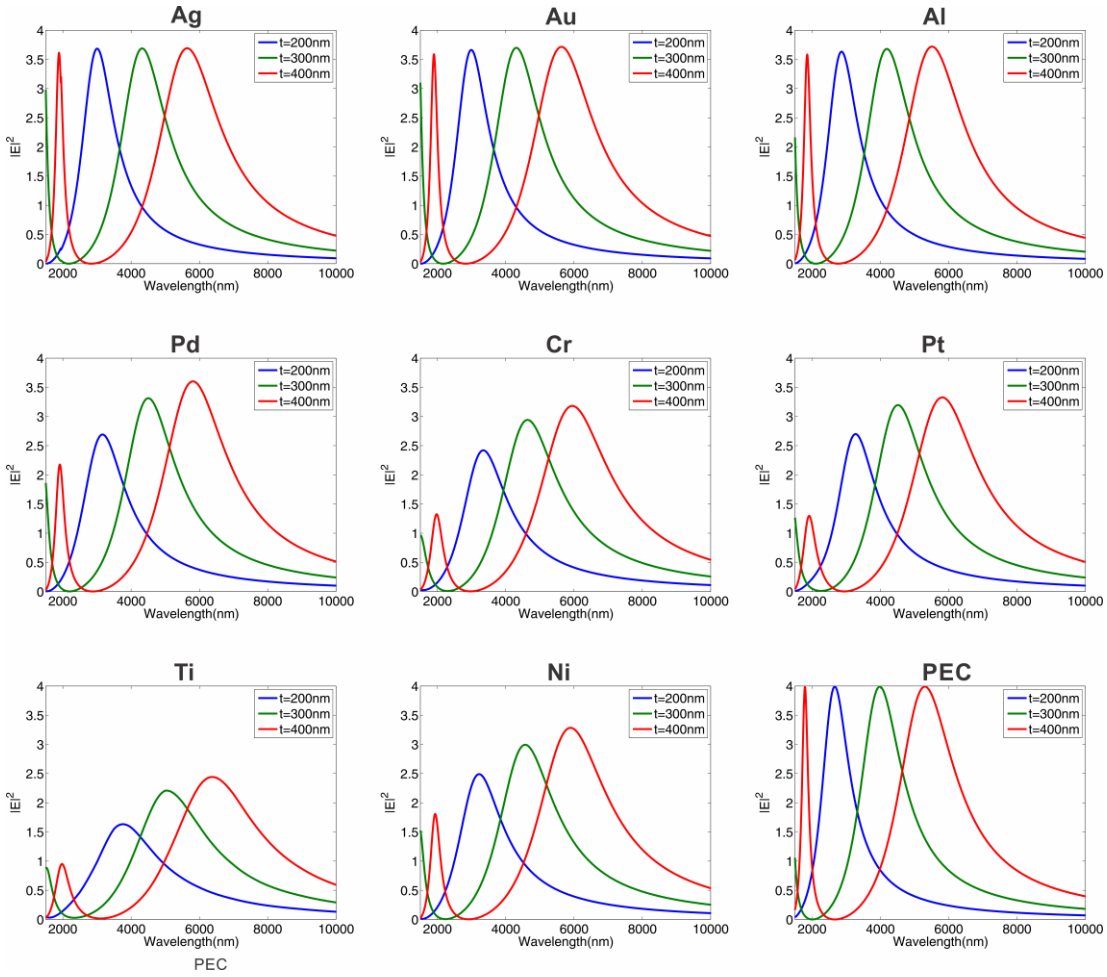

Figure 5-4. Simulated electric field enhancements on the surfaces of a-Si layers with various thicknesses on metals and a perfect electrical conductor (PEC) layer. The enhancement factor increases with increasing wavelength for metals as their optical properties approach those of a perfect electrical conductor.

The initial surfaces are fabricated using amorphous silicon (a-Si) as the dielectric layer on Al coated Si substrates following the simulations in Figure 5-1. The surfaces are coated with 5 nm PMMA layer, used as the probe material to test the sensing performance of the surfaces. The a-Si thickness is chosen to tune the surface's first order resonance to be close to the PMMA's strongest vibrational band at 1732 cm^{-1} (λ~5.77 µm). The center to edge variation in the a-Si thickness (400 – 460 nm) results in resonances in between 5.3 and 6.1 µm, revealing the major PMMA band with signal intensities of 6-7 % after background subtraction (Figure 5-5). The sensing performance of the surface is still good at extreme incident angles (75°) for both TE and TM polarizations (Figure 5-6), enabling relaxed design options for sensing systems based on these surfaces. These surfaces are successful at identifying PMMA, however also exhibit very strong Si-H vibrational bands[238], [249] at

~2010 cm^{-1}. The presence of Si-H bands is attributed to SiH_4 gas used for the deposition of the films in a plasma enhanced chemical vapor deposition (PECVD) system. The strong signal due to the Si-H vibrational bands would prevent sensing materials with vibrational bands in this regime, limiting the use of the surfaces formed by PECVD deposited a-Si layers. The Si-H and PMMA vibrational bands in the reflection spectrum are not observed for PECVD deposited, thinner a-Si layers whose primary resonances are at lower wavelengths (Figure 5-7).

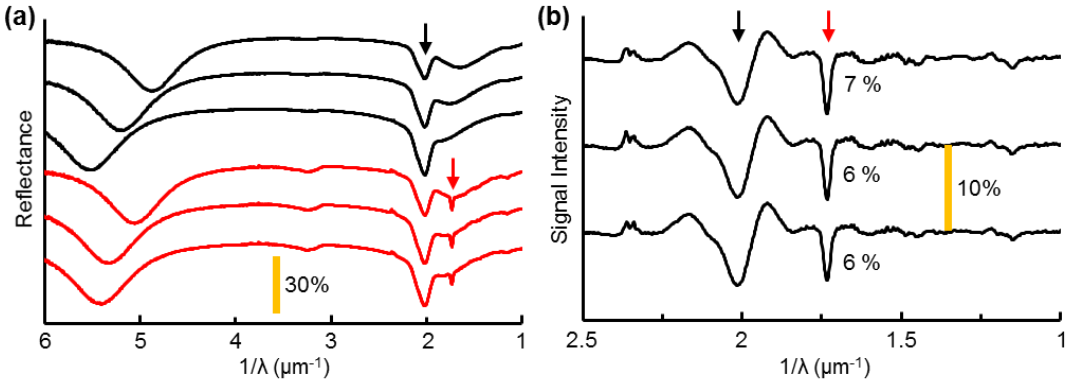

Figure 5-5. Experimental demonstration of infrared sensing using a-Si layers with different thicknesses (400-460 nm). (a) Reflectance spectra of the as fabricated (black) and 5 nm PMMA coated surfaces (red). Arrows mark the Si-H band at 2010 cm^{-1} and PMMA and 1732 cm^{-1}. (b) The signal intensities after background subtraction. The background signal is calculated by smoothing the reflectance curves using the moving average method. The signal intensity decreases as the resonance shifts away from the major PMMA band.

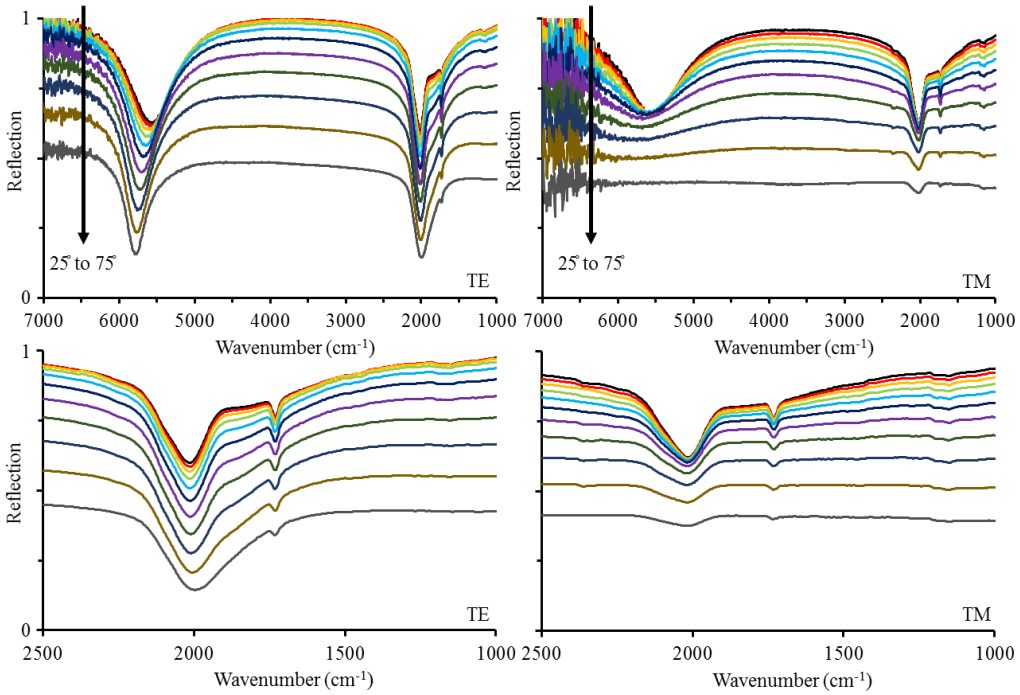

Figure 5-6. Angle dependent infrared ellipsometer measurement results for 5 nm PMMA coated 400 nm PECVD Si on Al surface (The normal incidence results are shown in Figure 2 of the main document). The incident angle is varied between 25° to 75° with 5° steps. The signal intensity due to the PMMA vibrational band at 1732 cm^{-1} reduces to %1.7 at 75° from % 5.6 at 25°. For TM polarization, the resonances and the signals from the PMMA and Si-H bands are strong up to high incident angles.

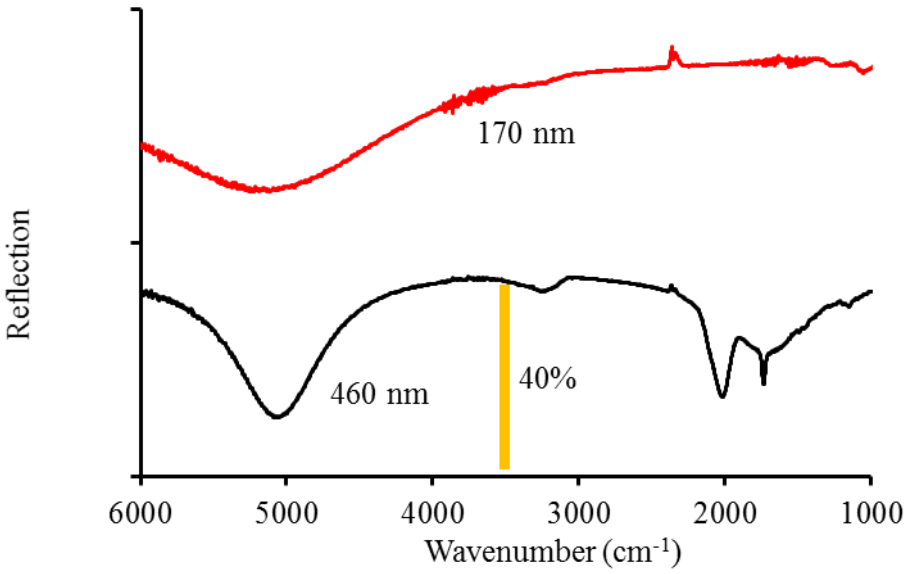

Figure 5-7. Reflection spectra of 5 nm PMMA coated PECVD deposited a-Si surfaces with 170 and 460 nm thicknesses on Al. No significant Si-H or PMMA bands are observed for 170 nm a-Si surface.

5.1.3. Thermally Tunable IR Spectroscopy Platforms Using $Ge_2Sb_2Te_5$

$Ge_2Sb_2Te_5$ (GST) in amorphous phase has a similar refractive index function to that of a-Si in the MIR and does not have a-Si layer's inherent surface problems. Chalcogenides, in general, are preferred for IR applications owing to their high IR transparency, low temperature-coefficient of refractive index and low dispersion[250]. GST, in particular, is a phase-change material, exhibiting amorphous to face-centered cubic structure (c-GST) transition at ~150 C which is accompanied by a large change in its electrical and optical properties. Phase-change material based electrical data storage (phase-change memory, PCM) devices, which target the non-volatile memory market, take advantage of the contrast between the electrical resistivity of the material in amorphous and crystalline phases[251]. The contrast in the optical properties of phase-change materials like GST has been used in the optical data storage media for decades[252]. Although optical properties of the phase-change materials have long been studied, number of reports on optical devices/surfaces using these materials have recently increased due to their potential use in plasmonic applications in the IR[253], [254] and strong-interference-effect based applications in the visible regime[255], [256]. GST thicknesses used in these devices/surfaces are typically small (7 - 50 nm). A rather thick GST (>80 nm) on a metal layer exhibits optical resonances in the IR[257]. The optical responses of these surfaces are tuned over a larger wavelength range owing to large refractive index contrast between amorphous and crystalline phases (Figure 5-8).

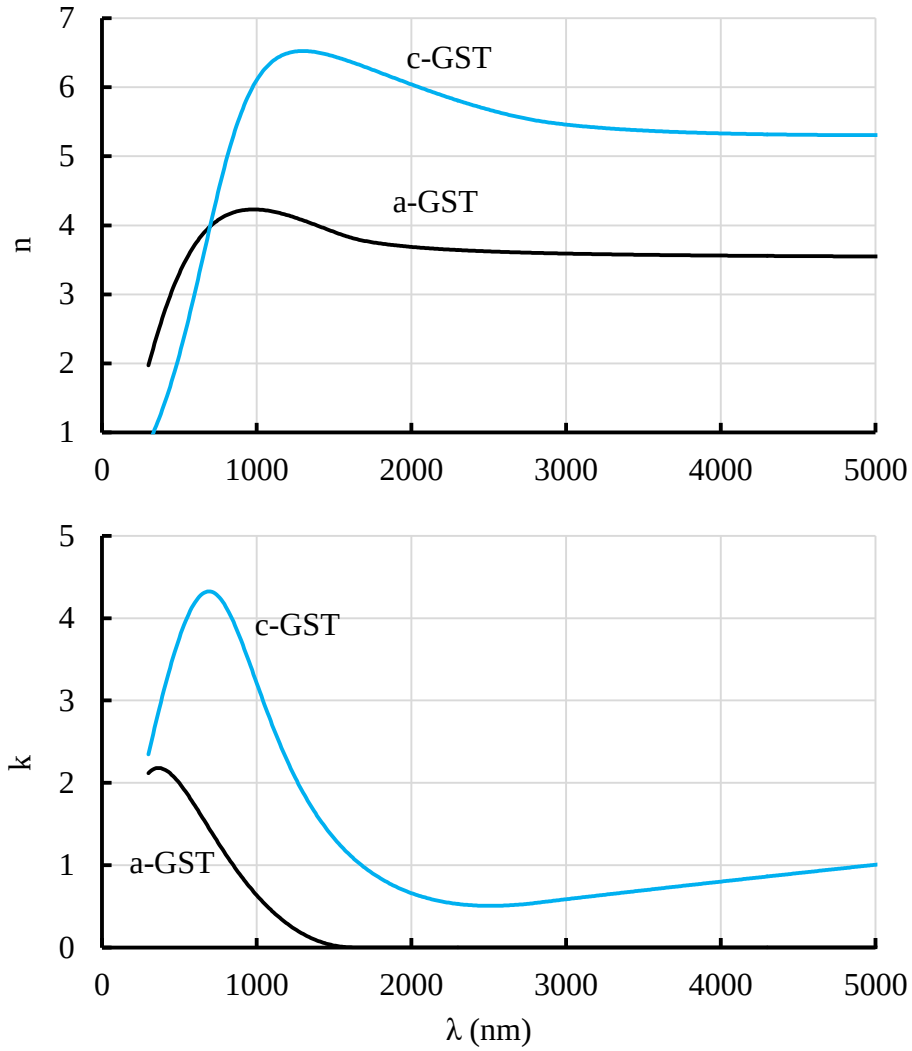

Figure 5-8. Refractive index and extinction coefficient of a-GST and c-GST films. The optical parameters are extracted by spectroscopic ellipsometer measurements of GST films on Si wafers at various angles in the 300 – 1700 nm range. The optical parameters are extracted within and beyond this wavelength range using the Tauc-Lorentz oscillator model for a-GST films and the Tauc-Lorentz + Drude oscillator models for c- GST films. The refractive index of c-GST predicts higher resonance wavelengths than what is observed in measurements. This is attributed to diffusion of Al into GST and reducing the effective refractive index of the GST layer during crystallization of the GST films. Diffusion of Al into GST can be avoided by introducing a thin barrier layer, such as TiN, in between Al and GST layers.

The measured reflection spectra of GST films on Al show great potential for the sensing purposes as the near-IR (NIR) and MIR spectrum are covered by varying the GST thickness and can be further tuned by crystallizing the films (Figure 5-9). Crystallization of a-GST layer consistently red-shifts the resonance owing to the larger refractive index of c-GST. When crystalline to amorphous volume ratio is changed gradually, instead of complete crystallization, a mixed optical response is

achieved. Partial crystallization is performed by laser annealing of different portions of a-GST films on Al surfaces (Figure 5-9).

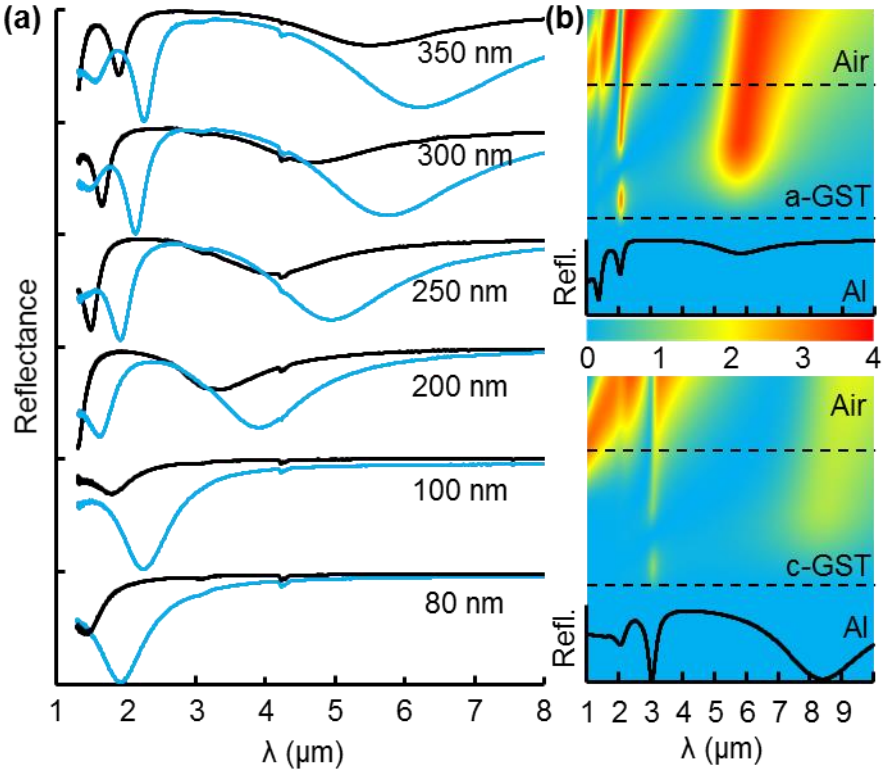

Figure 5-9. NIR and MIR results for GST layers on Al. (a) Reflection spectra of a-GST (black) and c-GST (blue) covered Al surfaces for indicated GST thicknesses. The crystallized films are expected to be 5 % thinner than the as-fabricated a-GST films[257]. (b) Calculated electric field ($|E|^2/|E_o|^2$) enhancements across cross-sections of 350 nm a-GST and c-GST films on Al and corresponding reflection spectra.

Alternatively, the gradual crystallization can be achieved by controlling the annealing duration of a-GST films at a high temperature (<150 C), which requires simultaneous monitoring of the optical response of the surfaces. For sensing experiments, only complete amorphous or complete crystalline films are used, since the areas of the laser scanned surfaces are limited to 100 x 100 μm^2. The calculated maximum field enhancement factors on the surface of 350 nm films is ~3.5 for a-GST and ~1.4 for c-GST (Figure 5-9). The lower enhancement factor for c-GST, at the resonance is attributed to the high refractive index (n) and non-zero extinction coefficient (k) of c-GST, which makes c-GST a lossy dielectric in the MIR. As a result, crystallizing a-GST films enables tuning the resonance to a higher wavelength

while reducing the enhancement factor. The higher order resonances for both phases are observed to be sharp with field confinements within the films (Figure 5-9).

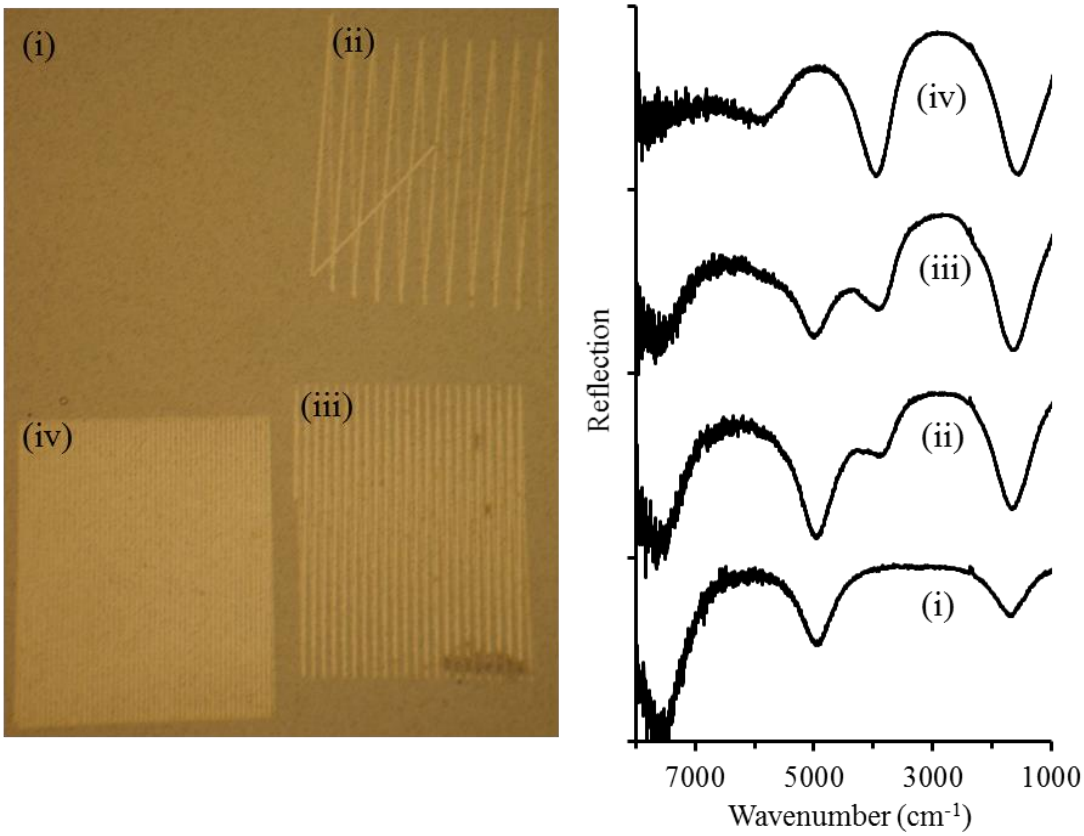

Figure 5-10. Optical microscope image and reflection spectra of 100 µm x 100 µm GST surfaces (t: 350 nm) on Al. Crystalline to amorphous ratio increases from (i) to (iv), (i) being completely amorphous and (iv) being completely crystalline. Lighter color lines are crystalline regions. The surface is laser-scanned using a green laser with 1 µm spot size equipped on a Raman system.

Sensing performance of the GST surfaces are tested using very thin (5 nm) PMMA layer on GST films with 200 and 350 nm thicknesses (Figure 5-11) which target the PMMA vibrational bands around 3000 and 1500 cm^{-1}, respectively. 200 nm a-GST surface reveals the bands at 2997, 2952 and 1732 cm^{-1}. 200 nm c-GST surface shows the PMMA bands at 2997, 2952 cm^{-1} with lower signal intensities, and the 1732 cm^{-1} band with a higher signal intensity owing to its higher wavelength resonance (Figure 5-11). The major PMMA band at 1732 cm^{-1} is observed as ~7 % drop in the reflection spectrum of 350 nm a-GST surface. 350 nm a-GST is particularly good at sensing all the vibrational bands larger than 1000 cm^{-1}. 350 nm c-GST surface exhibits a smaller signal at 1732 cm^{-1} due to its smaller enhancement factor despite its deeper resonance and performs better for higher wavelength PMMA bands such as 1151 cm^{-1} compared to 350 nm a-GST surface. Monolayer sensing

performance of 350 nm a-GST surface is tested by binding BSA on the surface. The BSA vibrational bands at 1652 and 1531 cm^{-1} are observed on the reflection spectrum of 350 nm a-GST surface with a signal intensity of 6 % at 1652 cm^{-1}. This signal intensity is larger than 3-4 % which are reported for plasmonic surfaces in the literature[64], [240]. The GST surfaces are further tested with ODT molecules which forms a monolayer on Au. 250 nm a-GST surface is functionalized by depositing 1.5 nm Au on top. The top Au layer is chosen to be very thin to form Au nano-islands instead of a continuous film on the GST surface in order not to modify the optical response significantly (Figure 5-12). Both ODT bands at 2849 and 2917 cm^{-1} are sensed by 250 nm a-GST and c-GST surfaces. The signal due to the ODT band at 2917 cm^{-1} is 3 % for 250 nm a-GST surface, despite a slight mismatch between the surface's resonance and the targeted ODT bands (Figure 5-13), being similar to the enhanced performance of pedestal gold structuress from the literature[242].

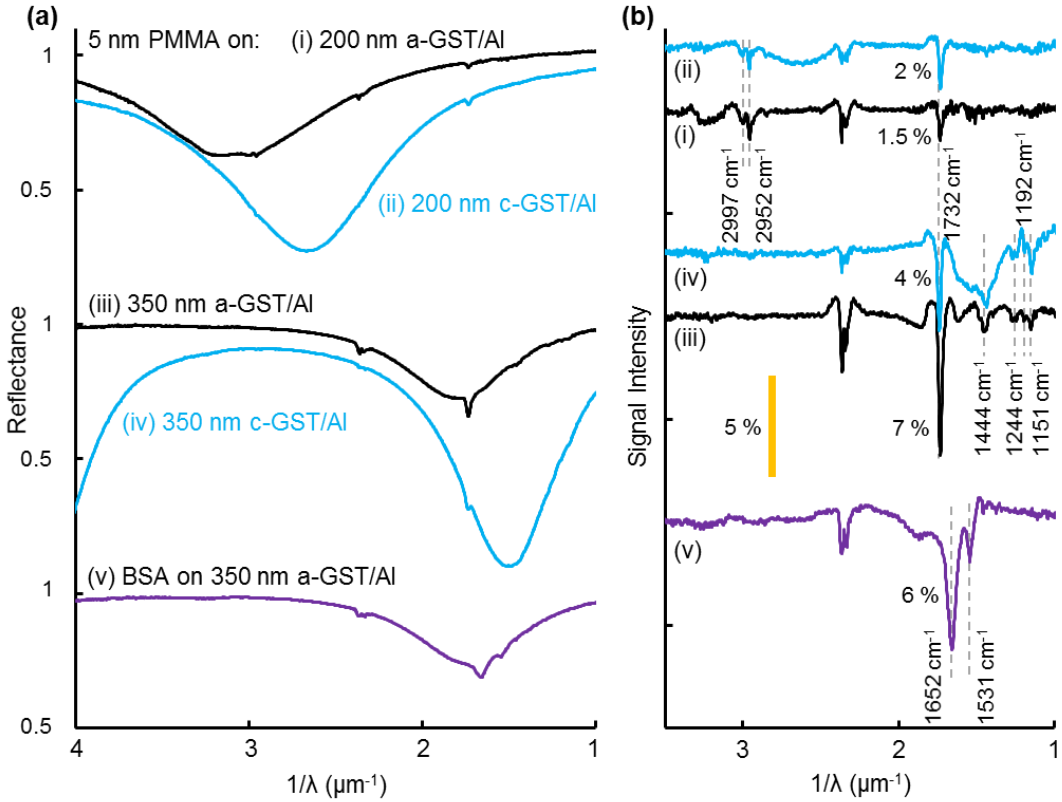

Figure 5-11. Sensing performances of GST surfaces. (a) Reflection spectra of 200 and 350 nm GST surfaces covered with 5 nm thick PMMA or monolayer BSA. (b) The signal intensities after background subtraction. The background signal is calculated by smoothing the measurement curves using the moving average method. The sensed vibrational bands of PMMA and BSA are marked with dashed lines and labeled.

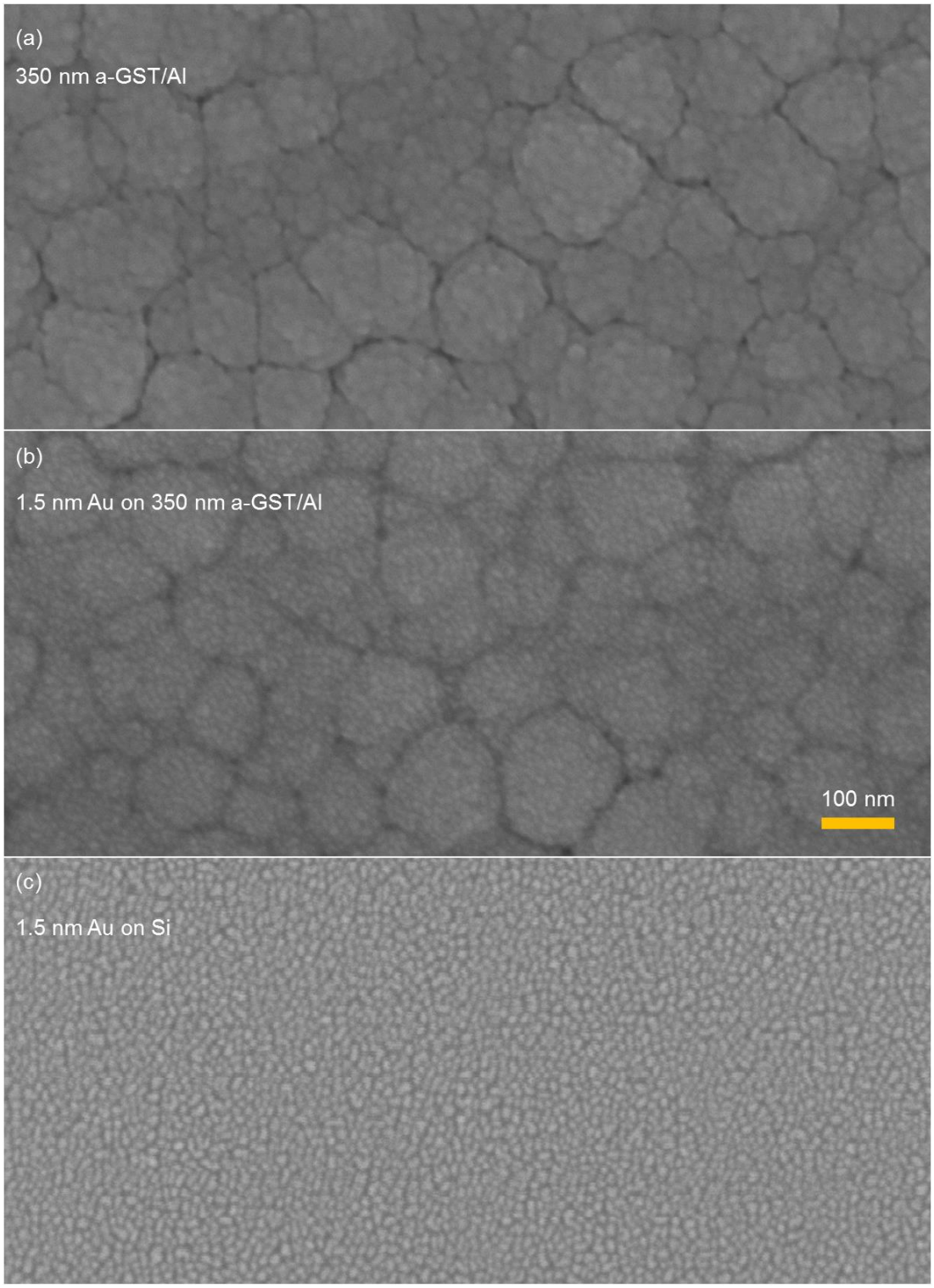

Figure 5-12. Scanning electron microscopy (SEM) images of 350 nm a-GST films on Al (a) with and (b) without 1.5 nm Au top layers. (c) SEM image of 1.5 nm Au on Si.

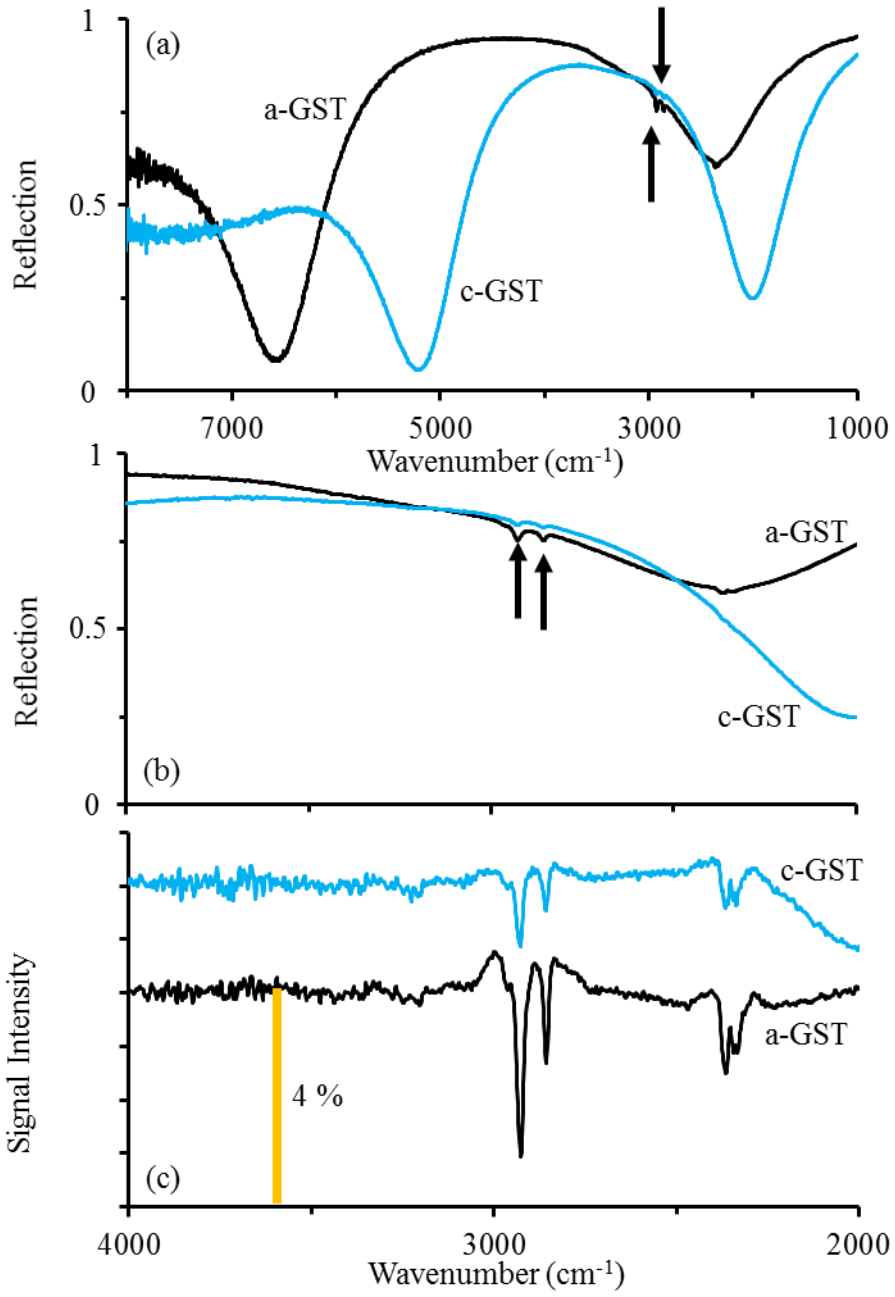

Figure 5-13. (a-b) Reflection spectra of ODT covered 1.5 nm Au/250 nm GST/Al surfaces. Arrows mark the ODT bands at 2849 and 2917 cm^{-1}. (c) Signal intensities due to the ODT bands after background subtraction. Signal intensities at 2917 cm^{-1} are % 3 for a-GST and % 1 for c-GST surface.

5.2. Strong Interference Based Colorimetric Sensors

5.2.1. Introduction

Label free detection of biomolecular interaction has attracted great attention due to its importance for pharmacological and biomedical applications in both health and research areas[1], [32], [258]–[262]. Different types of label-free sensing platforms

have been developed to overcome the difficulties that the label-based sensing platforms face[33], [55], [263]. Surface plasmon based sensors are among the most studied label-free sensors[33], [56], [224], [264]–[266]. Different types of platforms utilizing surface plasmons have been developed. Surface enhanced Raman spectroscopy (SERS)[210], [267]–[270] and surface enhanced infrared absorption spectroscopy (SEIRA)[63], [64], [67] use the vibrational bands of molecules that interact with localized or surface plasmons. Although, in SERS, the scattered Raman signal is too complicated to determine specific biomolecular interactions, bio-detection at the single molecule sensitivity is possible[198], [211], [270]. On the other hand, in SEIRA the vibrational signatures of different molecules exhibit similar bands limiting the probing of biomolecular interactions. Other than vibrational spectroscopies, surface plasmon sensors (SPR) emerges as one of the prominent label-free sensor technologies by taking advantage of local refractive index change during biomolecular binding events[1], [33], [224], [265], [271]–[273]. SPR technology is further improved for probing multiple biomolecular events by incorporating imaging equipment to the system[56]. Generally, these types of SPR systems rely on the reflected light intensity that is captured by a camera and is a type of refractometric sensor. Among the refractometric sensors, interference based refractometric sensors draw attention due to their ease of use and lab-on-chip compatibility[258], [274], [275]. These types of sensors rely on the local refractive index change due to the change in the thicknesses of bio-molecules. These sensors are typically fabricated on silicon chips and composed of thick layer of oxide which exhibits interference fringes in the reflection spectra. The biomolecular interactions are investigated by illuminating the chip with either a broadband or narrow light source and collecting the reflected light with either a spectrometer or a camera. Colorimetric sensing mechanism is in the core of the current label-based sensing mechanisms such as ELISA[56], [261], [276]. Recently, a new type of sensing mechanism using plasmonic nano-particles has emerged[272], [277]. These type of sensors are based on the chemical-reaction driven color change occurred due to the presence of target molecules due to either change in size of particles or the distance between them. Metal ions and bio-molecules have been detected using these type of sensors[278].

A reflective surface, such as a thin metal film, covered with a thin layer of lossy dielectric show optical resonances (strong interferences) and can show perfect

absorption at certain wavelengths depending on the complex refractive indices (n+ik) of the metal and dielectric layers. The strong interference resonances are due to destructive interference of the light reflected form the top and bottom of the lossy dielectric layer with phases different from 0 or π. The analysis of the strong interference effects and the n and k conditions which provide resonances are elucidated by Kats et al[74]. Unlike the thin film interference coatings ($t \approx \lambda/4n$) these surfaces exhibit resonances for thinner dielectric coatings ($t \approx \lambda/8n$). Thinner dielectric coatings also enable a wide angular spectral response due to small phase accumulation. Since then, strong interference effects have been investigated for coloring surfaces using gold and germanium[74], tunable, dynamic infrared filters using sapphire and VO_2[279], light sensing using Ag and amorphous Si[77] and advanced optical data storage using Au and $Ge_2Sb_2Te_5$ (GST)[280]. So far, most of the studies based on these types of coatings are utilized for color printing applications. In this part of the thesis a novel colorimetric sensor based on interference coatings using highly absorptive layer is presented. Unlike the refractometric interference sensors, a lossy dielectric layer is deposited on top of a mirror or metal surface. The proposed sensor surfaces can be fabricated on large areas and have wide angle optical response. Ultra-thin dielectric coatings and protein monolayer are detected using these sensors.

5.2.2. Results

The proposed sensing surface is shown in Figure 5-14. The structure consists of a thin amorphous silicon (~20nm) layer on top of a thick (~80 nm) aluminum film. Similar surfaces using different absorptive dielectric films have been demonstrated to have resonances in the visible spectrum. Such surfaces are utilized mostly for color printing applications. It has been shown that even small variations in the thickness of absorptive dielectric films with high refractive indices results in color change. The proposed sensing principle is based the color change due to molecular binding events as shown in Figure 5-14a. The optical microscope image of a fabricated surface is shown in the inset of Figure 5-14b. The image is taken under halogen light illumination with 5x magnification. Since the surface color strongly depends on the spectrum of the illumination light, the surface shows different colors under different light sources. For this work, we used a halogen bulb integrated to optical microscope for all measurements. The reflection spectrum shows a resonance with almost perfect

absorption at ~510nm as shown in Figure 5-14b. The resonance, hence the color of the surface, is wide angle for both polarizations (Figure 5-14 c, d). The resonance wavelength of the surface can be tuned by increasing the thickness of a-Si layer. Thicker a-Si thickness also results similar reflectance spectra due to excitation of higher order interference modes (See Figure 5-15). However, wavelength shift due to dielectric layer for thicker a-Si layer negligible due to higher electric confinement to the a-Si layer and smaller electric field intensity at air/a-Si interface.

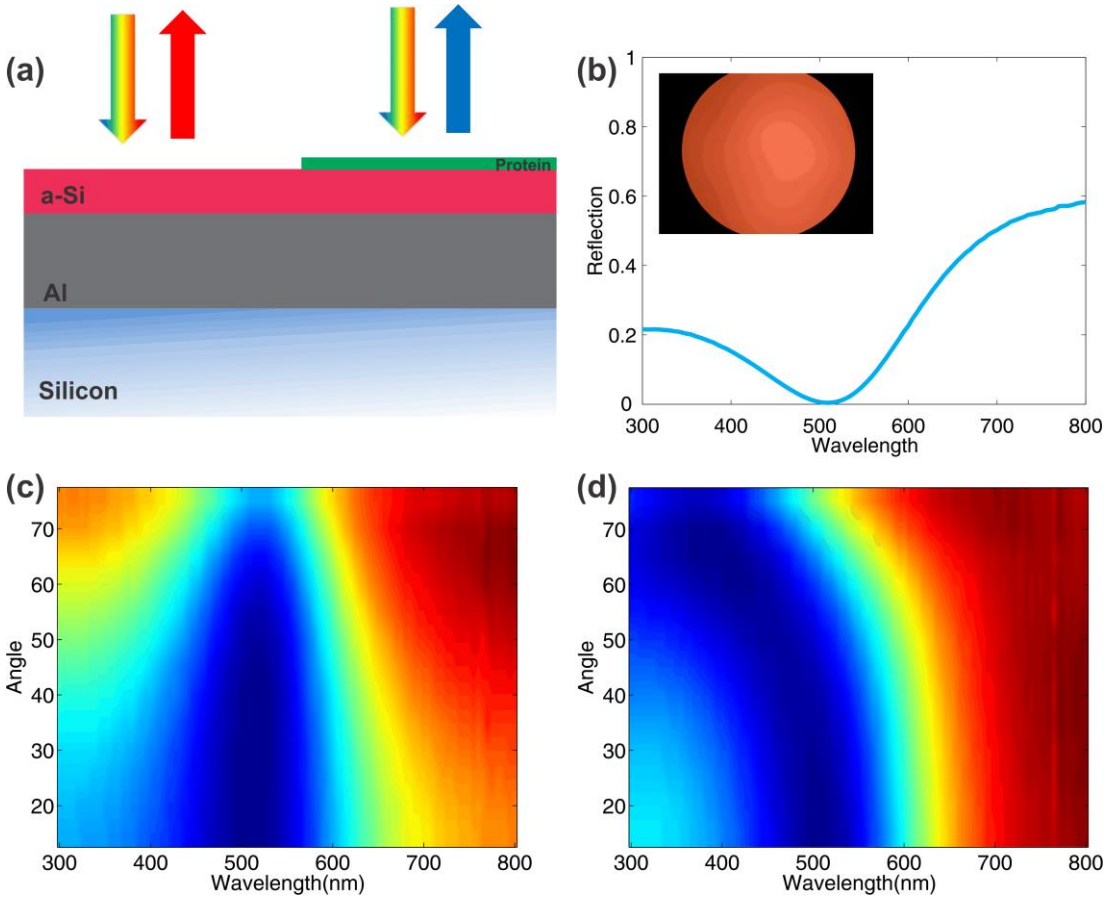

Figure 5-14. Optical characterization and the working principle of the proposed sensing platforms. (a) Cross section illustration of the sensing platform. For broadband excitation (white light), surfaces reflects distinct color. The color of reflected light changes upon deposition of a very thin dielectric layer (~3-5nm) or protein monolayer. (b) Reflection spectra of surfaces. (Inset) Microscope image of the surface illuminated with halogen light. Measured reflectance spectra map for (c) s and (d) p polarizations.

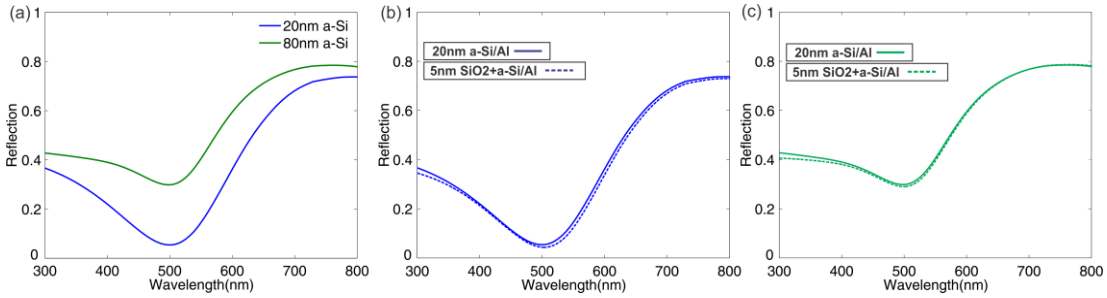

Figure 5-15. Comparison of sensing performances of surfaces with different a-Si thicknesses. (a) Simulated reflected spectra for 20nm and 80nm a-Si on Al. Simulated reflectance spectra without(solid curve) and with(dashed curve) 5nm dielectric layer(n=1.5) for 20nm(b) and 80nm a-Si thicknesses.

In order to characterize the colorimetric sensing performance, dielectric films with varying thicknesses deposited on top the surfaces. Similar experiments have been performed by depositing Al_2O_3 on germanium coated gold films recently to enhance the color contrast by e-beam evaporation. Here, SiO_2 films are deposited by e-beam evaporation with different thicknesses (5, 10, 15 and 20nm) on our sensing surfaces. The thickness and refractive index of deposited films are characterized by variable angle spectroscopic ellipsometer (n~1.5). The reflectance spectra shows a red-shift in the resonance wavelength when the thickness of the SiO_2 increases (Figure 2 a, b). The color of the sensing surfaces is shown in Figure 2c. The intensity of the blue channel changes significantly due to increase in SiO2 thickness as shown in Table 1. However, the green and red channels do not show a significant trend. The intensity change of blue channel is attributed to the blue-shift in resonance wavelength where blue portion (~400-450nm) of the spectrum is reflected more and the red portion of the spectrum(~650-700nm) is reflected less. We have also deposited Al_2O_3 films by atomic layer deposition (ALD) at 80^{o}C with three different thicknesses (50, 100 and 150 cycles). The thicknesses of Al_2O_3 films are measured to be 5, 10 and 15nm using ellipsometer. The refractive index of Al_2O_3 is close to that of SiO_2 and proteins (~1.5) which is different than the refractive index values reported in the literature. Al_2O_3 deposited surfaces also show wavelength shift with increasing oxide thickness similar to SiO_2 deposited surfaces (See Figure 5-17). We have also demonstrated color change by depositing ultrathin PMMA layer on the sensor surface. 5nm PMMA film is spin-coated on the surfaces shows also color change as shown in Figure S6. The square regions in Figure S6b are patterned by e-beam lithography and PMMA-free region have different color than the PMMA coated regions.

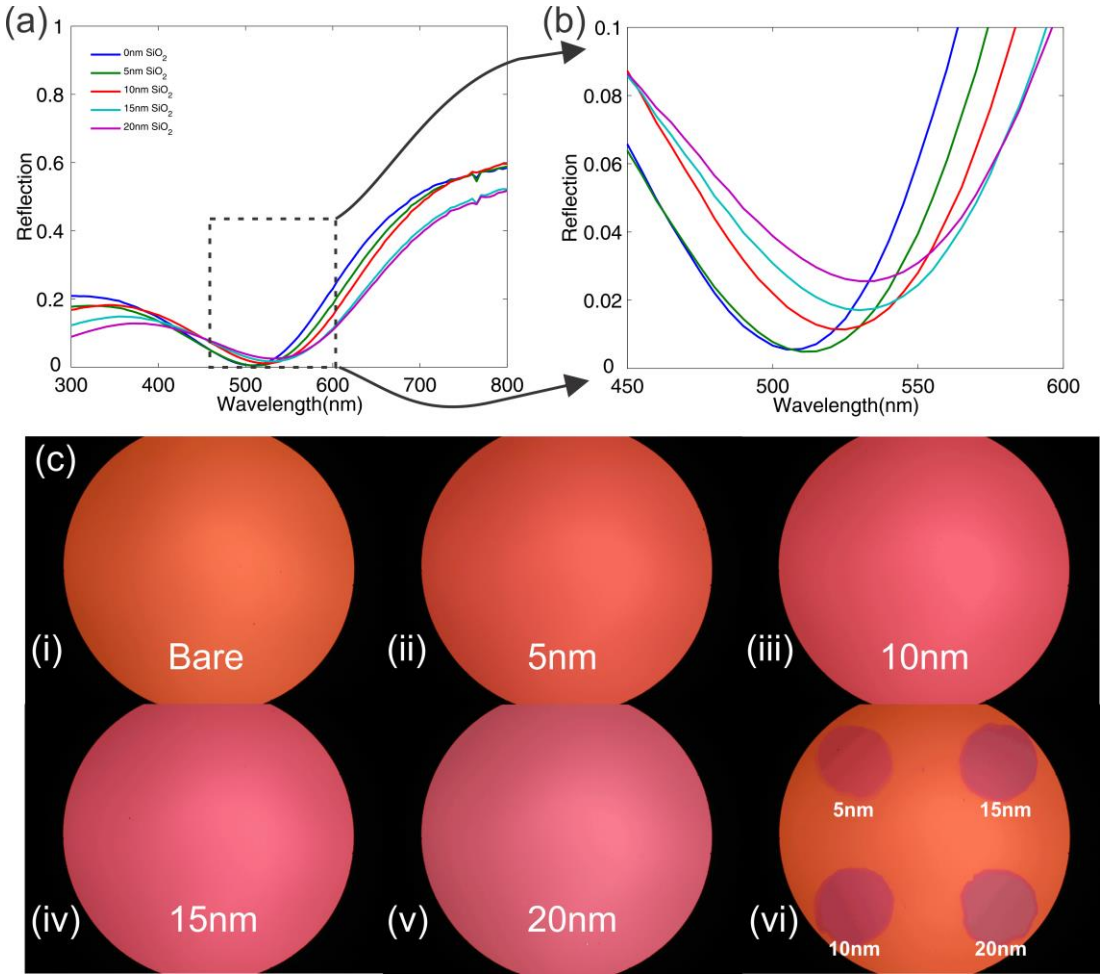

Figure 5-16. Optical characterization of sensing platforms with different SiO_2 thicknesses. (a) Reflection spectra with 0, 5, 10, 15 and 20nm SiO_2 thicknesses. (b) Reflectance spectra around the resonance wavelength. (c) Optical images of the surfaces with (i) 0nm, (ii) 5nm, (iii) 10nm, (iv) 15nm and (v) 20nm SiO_2 thickness. (vi) SiO_2 spots with different thicknesses are deposited on the sample surfaces with a shadow mask

Table 1. RGB values of sensing platforms with different SiO_2 thicknesses.

	0nm SiO_2	5nm SiO_2	10nm SiO_2	15nm SiO_2	20nm SiO_2
R	221	222	225	223	218
G	94	85	84	89	98
B	58	69	97	110	117

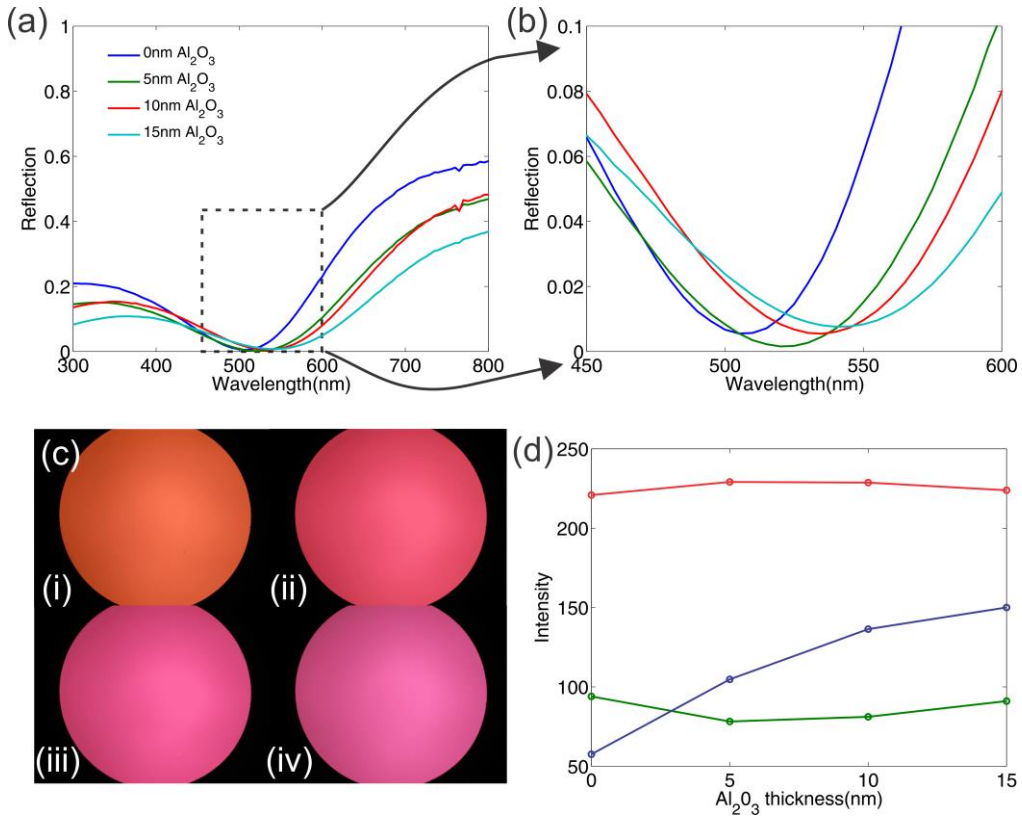

Figure 5-17. Optical characterization of sensing platforms with different Al_2O_3 thicknesses. (a) Reflection spectra with 0, 5, 10 and 15nm Al_2O_3 thicknesses. (b) Reflectance spectra around the resonance wavelength. (c) Optical images of the surfaces with (i) 0nm, (ii) 5nm, (iii) 10nm and (iv) 15nm Al_2O_3 thickness. (d) Intensity values for RGB channels for different SiO_2 thicknesses.

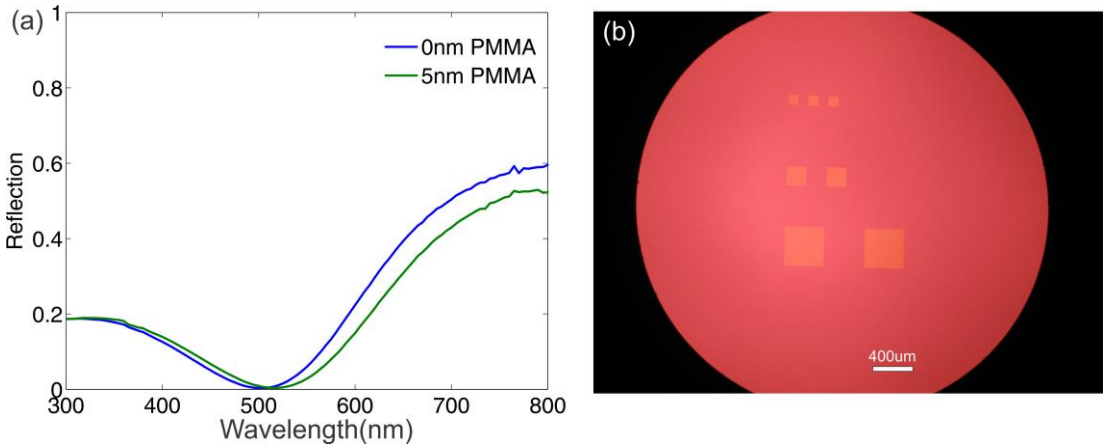

Figure 5-18. Optical characterization of sensing platforms with PMMA coating. (a) Reflection spectra with and without 5nm PMMA coating. (b) Optical image of the PMMA coated surface. The square patterns are PMMA-free regions.

5.2.3. Protein Binding Experiment

In order the test the biomolecular interaction of our sensor platform, we performed binding event using mono and bi-layer bovine serum albumin (BSA). For monolayer and bi-layer BSA coatings, we adopted a well known procedure[281]. The schematic of protein binding experiment is shown in Figure 5-19a. The sensor surfaces are immersed in BSA/citrate buffer solution for 2 hours for monolayer formation. Then the surfaces are washed with citrate buffer to remove un-bound BSA proteins. The surfaces are immersed in dextrane sulfate/citrate buffer solution for 1 hour to negatively charge the positively charged BSA surface for BSA layer coating. The reflectance spectra of BSA coated surfaces are shown in Figure 5-19b. The resonance wavelength red-shifts for monolayer BSA coating ($\Delta\lambda$~8nm). After the second BSA layer the resonance wavelength shift is about ($\Delta\lambda$~18nm). Higher resonance wavelength shift for the second BSA layer is attributed to the different optical properties and thicknesses of positively and negatively charged BSA layers. There is a significant difference between the surfaces as shown in Figure 5-19c. For bi-layer BSA coated surface, the color is close to purple due to the increased reflected light intensity at shorter wavelengths (~400-450nm). The surfaces can also be differentiated from the photographs of the same surfaces captured with a mobile phone's camera as shown in Figure 5-19d. The color change due to protein binding is also be detected with naked eye.

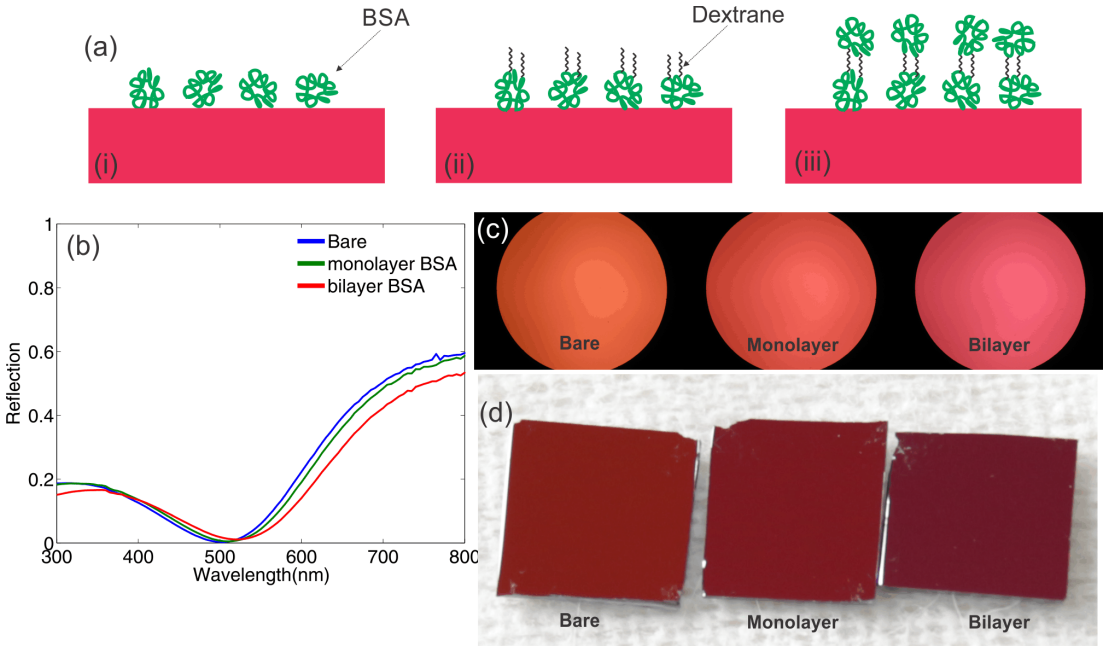

Figure 5-19. Colorimetric sensing of protein binding events. (a) Schematic of protein binding experiments. (i) BSA monolayer is coated on the sensor surface by physobsorption.(ii) Binding dextrane layer to BSA protein to negatively charge the BSA protein surface. (iii) Second BSA layer is covalently bound to dextran layer. (b) Reflectance spectra for bare surface, monolayer and bi-layer BSA coated surfaces. (c) Optical microscope images of bare (i), monolayer (ii) and bi-layer (iii) BSA coated surfaces. (d) Photograph of the same surface taken with a cell phone camera.

5.3. Conclusion

In the first part of this chapter, we propose using thin dielectric layers, such as aGST and a-Si, coated metal ground planes as optical platforms for ultrasensitive IR vibrational spectroscopy measurements. Switching to a-GST overcomes the a-Si layer's drawbacks and enables further tuning of the optical resonance by transitioning to c-GST at ~150 C. Crystallization of GST films on Al layers red-shifts the resonance owing to the higher refractive index and non-zero extinction coefficient of c-GST while the vibrational band signals at higher wavelengths are enhanced. The GST surfaces are successful at sensing monolayers of BSA and ODT, proving themselves as highly sensitive IR sensing platforms. The proposed surfaces are fabricated very fast with one deposition step, without any patterning process and on large substrates such as Al coated Si substrates or thin Al foils. High sensitivity, angle- independent response and large area of the surfaces reduce the strict IR sensing measurement requirements such as the need for magnification or specific

measurement angle which are typically used for lithographically defined small-area surfaces. While the cutting edge plasmonic based SEIRA studies aim to reach single molecule sensitivity[67] by extremely enhancing localized fields, the proposed surfaces perform better at detecting of ultra-thin and monolayers of materials with further advantages of fast, inexpensive, easy fabrication, wafer-scale dimensions, and thermal tunability.

In the second part, we have demonstrated a novel colorimetric sensor platform based on strong interference effects exhibited by highly absorbing dielectric films on metal surfaces. First, the sensing performance is tested using different dielectric coatings with different thicknesses. The resonance wavelength shifts of the surfaces are also prominent which can be used as sensing mechanism. The color change can easily be detected after very thin dielectric film deposition. Then, protein binding experiments are performed through monolayer and bi-layer BSA coatings on the sensing surfaces. Although our experiments are performed in air with monolayer and bi-layer BSA protein coatings, real time binding experiments can be performed by functionalizing the surfaces with protein antibodies. Since, there are no nano-fabrication process, e-beam or optical lithography steps, these sensor platforms can be fabricated on laboratory glass slides over large areas in large scales. These sensor surfaces can be integrated to mobile phone based o portable point of care devices which can be advantageous in low-resource areas for the detection of disease biomarkers.

Chapter 6

Conclusion

In this thesis, we first demonstrate simple coupled plasmonic geometry in the visible spectrum. A simple electrical circuit model is developed to understand optical properties. Surface enhanced Raman spectroscopy (SERS) is one of the important applications of these of plasmonic surfaces since multiple resonances exhibited by these surfaces can be exploited for either different laser excitation wavelength or Raman wavelengths. Confocal Raman experiments have shown that these surfaces exhibit unity Raman enhancement over large areas due to subwavelength periodicities. Although, these coupled plasmonic surfaces display broadband and multispectral spectral response, the use of e-beam lithography limits the fabrication of these surfaces over large areas. Similar plasmonic geometry with nanoparticle top layers can be fabricated over large areas showing similar optical properties using simple physical deposition methods. Fabricated surfaces perfectly absorb light for almost the whole visible spectrum up to 60 degrees angle of incidence. Single Raman events are detected using nanoparticle based coupled plasmonic surfaces using confocal Raman system. Single molecule Raman events can also be detected using a mobile phone's camera either with camera or spectrometer mode. Similar surfaces with thinner insulator layers are used to study plasmon enhanced hot electron effects. Hot-electron effects are probed using an XPS system with external laser excitation without using electrical contacts. The energy shifts of photoelectrons caused by laser excitation are used to extract photoresponsivities. The photoresponsivities display fair values, when compared to hot-electron currents of similar geometries. Aluminum based metal-insulator-metal plasmonic surfaces are fabricated by exploiting the native oxide layer to show resonances in the visible and IR wavelengths. The resonance wavelengths are simply tuned by exposing the surfaces to air for longer durations. The thicknesses of native oxide layer are characterized by XPS.

Nanoparticle based hierarchical aluminum surfaces are used SERS and SEIRA applications. All aluminum hierarchical surfaces are demonstrated with multiple resonances in the IR using native oxide layer as the spacer layer. In the last part, two novel applications of regular and strong interference coatings are demonstrated. Tunable surfaces are fabricated using phase change materials in the IR wavelengths. By simply heating the surfaces up-to phase change temperatures, the resonance wavelength is tuned. We have demonstrated SEIRA using these surfaces. By tuning resonance wavelength, different IR bands are enhanced. Amorphous silicon based strong interference coatings are fabricated and used as colorimetric sensor platforms. Monolayer and bilayer proteins can be detected using these surfaces as the change in surface color.

Bibliography

[1] H. Im, H. Shao, Y. Il Park, V. M. Peterson, C. M. Castro, R. Weissleder, and H. Lee, "Label-free detection and molecular profiling of exosomes with a nano-plasmonic sensor.," *Nat. Biotechnol.*, vol. 32, no. 5, pp. 490–5, May 2014.

[2] J. Homola, S. S. Yee, and G. Gauglitz, "Surface plasmon resonance sensors: review," *Sensors Actuators B Chem.*, vol. 54, no. 1–2, pp. 3–15, Jan. 1999.

[3] J. Homola, "Present and future of surface plasmon resonance biosensors.," *Anal. Bioanal. Chem.*, vol. 377, no. 3, pp. 528–39, Oct. 2003.

[4] J. A. Dionne, E. Verhagen, A. Polman, and H. A. Atwater, "Are negative index materials achievable with surface plasmon waveguides? A case study of three plasmonic geometries," *Opt. Express*, vol. 16, no. 23, p. 19001, Nov. 2008.

[5] E. Feigenbaum and M. Orenstein, "Perfect 4-way splitting in nano plasmonic X-junctions," *Opt. Express*, vol. 15, no. 26, p. 17948, Dec. 2007.

[6] M. C. Gather, K. Meerholz, N. Danz, and K. Leosson, "Net optical gain in a plasmonic waveguide embedded in a fluorescent polymer," *Nat. Photonics*, vol. 4, no. July, pp. 457–461, 2010.

[7] R. F. Oulton, V. J. Sorger, D. a. Genov, D. F. P. Pile, and X. Zhang, "A hybrid plasmonic waveguide for subwavelength confinement and long-range propagation," *Nat. Photonics*, vol. 2, no. 8, pp. 496–500, Jul. 2008.

[8] A. Sobhani, M. W. Knight, Y. Wang, B. Zheng, N. S. King, L. V Brown, Z. Fang, P. Nordlander, and N. J. Halas, "Narrowband photodetection in the near-infrared with a plasmon-induced hot electron device.," *Nat. Commun.*, vol. 4, p. 1643, Jan. 2013.

[9] A. Akbari, R. N. Tait, and P. Berini, "Surface plasmon waveguide Schottky detector," *Opt. Express*, vol. 18, no. 8, p. 8505, Apr. 2010.

[10] A. Akbari and P. Berini, "Schottky contact surface-plasmon detector integrated with an asymmetric metal stripe waveguide," *Appl. Phys. Lett.*, vol. 95, no. 2, p. 021104, Jul. 2009.

[11] V. E. Babicheva, N. Kinsey, G. V. Naik, M. Ferrera, A. V. Lavrinenko, V. M. Shalaev, and A. Boltasseva, "Towards CMOS-compatible nanophotonics: Ultra-compact modulators using alternative plasmonic materials," *Opt. Express*, vol. 21, no. 22, p. 27326, Nov. 2013.

[12] T. Zentgraf, Y. Liu, M. H. Mikkelsen, J. Valentine, and X. Zhang, “Plasmonic Luneburg and Eaton lenses.,” *Nat. Nanotechnol.*, vol. 6, no. 3, pp. 151–5, Mar. 2011.

[13] J. Qi, X. Dang, P. T. Hammond, and A. M. Belcher, “Highly efficient plasmon-enhanced dye-sensitized solar cells through metal@oxide core-shell nanostructure.,” *ACS nano*, vol. 5, no. 9. pp. 7108–16, 27-Sep-2011.

[14] M. W. Knight, H. Sobhani, P. Nordlander, and N. J. Halas, “Photodetection with active optical antennas.,” *Science*, vol. 332, no. 6030, pp. 702–4, May 2011.

[15] J. B. Lassiter, H. Sobhani, M. W. Knight, W. S. Mielczarek, P. Nordlander, and N. J. Halas, “Designing and deconstructing the fano lineshape in plasmonic nanoclusters.,” *Nano Lett.*, vol. 12, no. 2, pp. 1058–62, Feb. 2012.

[16] M. W. Knight, L. Liu, Y. Wang, L. Brown, S. Mukherjee, N. S. King, H. O. Everitt, P. Nordlander, and N. J. Halas, “Aluminum plasmonic nanoantennas.,” *Nano Lett.*, vol. 12, no. 11, pp. 6000–4, Nov. 2012.

[17] N. Yamamoto, S. Ohtani, and F. J. García de Abajo, “Gap and Mie plasmons in individual silver nanospheres near a silver surface.,” *Nano Lett.*, vol. 11, no. 1, pp. 91–5, Jan. 2011.

[18] H. Raether, *Surface Plasmons on Smooth and Rough Surfaces and on Gratings*, vol. 111. Springer-Verlag: Berlin, 1988.

[19] A. J. Pasquale, B. M. Reinhard, and L. Dal Negro, “Engineering photonic-plasmonic coupling in metal nanoparticle necklaces.,” *ACS Nano*, vol. 5, no. 8, pp. 6578–85, Aug. 2011.

[20] R. Scattering, F. Le, D. W. Brandl, Y. A. Urzhumov, H. Wang, J. Kundu, N. J. Halas, J. Aizpurua, and P. Nordlander, “Metallic Nanoparticle Arrays : A Common,” vol. 2, no. 4, pp. 707–718, 2008.

[21] N. Liu, M. Mesch, T. Weiss, M. Hentschel, and H. Giessen, “Infrared perfect absorber and its application as plasmonic sensor.,” *Nano Lett.*, vol. 10, no. 7, pp. 2342–8, Jul. 2010.

[22] X. Liu, T. Tyler, T. Starr, A. Starr, N. Jokerst, and W. Padilla, “Taming the Blackbody with Infrared Metamaterials as Selective Thermal Emitters,” *Phys. Rev. Lett.*, vol. 107, no. 4, Jul. 2011.

[23] E. J. Smythe, M. D. Dickey, J. Bao, G. M. Whitesides, and F. Capasso, “Optical Antenna Arrays on a Fiber Facet for in Situ Surface-Enhanced Raman Scattering Detection 2009,” *Nano Lett.*, vol. 9, no. 3, pp. 1132–1138, 2009.

[24] S. Rodriguez, a. Abass, B. Maes, O. Janssen, G. Vecchi, and J. Gómez Rivas, “Coupling Bright and Dark Plasmonic Lattice Resonances,” *Phys. Rev. X*, vol. 1, no. 2, pp. 1–7, Dec. 2011.

[25] A. Kocabas, G. Ertas, S. S. Senlik, and A. Aydinli, “Plasmonic band gap structures for surface-enhanced Raman scattering,” *Opt. Express*, vol. 16, no. 17, p. 12469, Aug. 2008.

[26] A. A. Yanik, A. E. Cetin, M. Huang, A. Artar, S. H. Mousavi, A. Khanikaev, J. H. Connor, G. Shvets, and H. Altug, “Seeing protein monolayers with naked eye through plasmonic Fano resonances.,” *Proc. Natl. Acad. Sci. U. S. A.*, pp. 1–6, Jun. 2011.

[27] G. H. Chan, J. Zhao, E. M. Hicks, G. C. Schatz, and R. P. Van Duyne, “Plasmonic Properties of Copper Nanoparticles Fabricated by Nanosphere Lithography,” *Nano Lett.*, vol. 7, no. 7, pp. 1947–1952, Jul. 2007.

[28] B. Kasemo, C. Langhammer, and Z. Michael, “Nanodisk Plasmons : Material Damping Mechanisms,” *ACS Nano*, vol. 5, no. 4, pp. 2535–2546, 2011.

[29] S. Ayas, G. Cinar, A. D. Ozkan, Z. Soran, O. Ekiz, D. Kocaay, A. Tomak, P. Toren, Y. Kaya, I. Tunc, H. Zareie, T. Tekinay, A. B. Tekinay, M. O. Guler, and A. Dana, “Label-free nanometer-resolution imaging of biological architectures through surface enhanced Raman scattering.,” *Sci. Rep.*, vol. 3, p. 2624, Jan. 2013.

[30] D. Wang, W. Zhu, M. D. Best, J. P. Camden, and K. B. Crozier, “Wafer-scale metasurface for total power absorption, local field enhancement and single molecule Raman spectroscopy.,” *Sci. Rep.*, vol. 3, p. 2867, Jan. 2013.

[31] A. I. Maaroof and D. S. Sutherland, “Optimum plasmon hybridization at percolation threshold of silver films near metallic surfaces,” *J. Phys. D. Appl. Phys.*, vol. 43, no. 40, p. 405301, Oct. 2010.

[32] B. Zhang, R. B. Kumar, H. Dai, and B. J. Feldman, “A plasmonic chip for biomarker discovery and diagnosis of type 1 diabetes,” *Nat. Med.*, vol. 20, no. 8, pp. 948–953, 2014.

[33] S. M. Tabakman, L. Lau, J. T. Robinson, J. Price, S. P. Sherlock, H. Wang, B. Zhang, Z. Chen, S. Tangsombatvisit, J. a Jarrell, P. J. Utz, and H. Dai, “Plasmonic substrates for multiplexed protein microarrays with femtomolar sensitivity and broad dynamic range.,” *Nat. Commun.*, vol. 2, p. 466, 2011.

[34] G. V Naik, V. M. Shalaev, and A. Boltasseva, “Alternative plasmonic materials: beyond gold and silver.,” *Adv. Mater.*, vol. 25, no. 24, pp. 3264–94, Jun. 2013.

[35] J. Wang, Y. Chen, X. Chen, J. Hao, M. Yan, and M. Qiu, “Photothermal reshaping of gold nanoparticles in a plasmonic absorber.,” *Opt. Express*, vol. 19, no. 15, pp. 14726–34, Jul. 2011.

[36] Y. C. Cao, R. Jin, and C. a Mirkin, “Nanoparticles with Raman spectroscopic fingerprints for DNA and RNA detection.,” *Science*, vol. 297, no. 5586, pp. 1536–40, Aug. 2002.

[37] H. Liu, Y. M. Liu, T. Li, S. M. Wang, S. N. Zhu, and X. Zhang, “Coupled magnetic plasmons in metamaterials,” *Phys. status solidi*, vol. 246, no. 7, pp. 1397–1406, Jul. 2009.

[38] R. Kekatpure, E. Barnard, W. Cai, and M. Brongersma, “Phase-Coupled Plasmon-Induced Transparency,” *Phys. Rev. Lett.*, vol. 104, no. 24, pp. 1–4, Jun. 2010.

[39] P. Nordlander, C. Oubre, E. Prodan, K. Li, and M. I. Stockman, “Plasmon Hybridization in Nanoparticle Dimers,” *Nano Lett.*, vol. 4, no. 5, pp. 899–903, May 2004.

[40] P. Nordlander and E. Prodan, “Plasmon Hybridization in Nanoparticles near Metallic Surfaces,” *Nano Lett.*, vol. 4, no. 11, pp. 2209–2213, Nov. 2004.

[41] J. B. Lassiter, J. Aizpurua, L. I. Hernandez, D. W. Brandl, I. Romero, S. Lal, J. H. Hafner, P. Nordlander, and N. J. Halas, “Close Encounters between Two Nanoshells 2008,” *Nano Lett.*, vol. 8, no. 4, pp. 1212–1218, 2008.

[42] S. Y. Lee, J. J. Amsden, S. V Boriskina, A. Gopinath, A. Mitropolous, D. L. Kaplan, F. G. Omenetto, and L. Dal Negro, “Spatial and spectral detection of protein monolayers with deterministic aperiodic arrays of metal nanoparticles.,” *Proc. Natl. Acad. Sci. U. S. A.*, vol. 107, no. 27, pp. 12086–12090, 2010.

[43] N. J. Halas, S. Lal, W. S. Chang, S. Link, and P. Nordlander, “Plasmons in strongly coupled metallic nanostructures,” *Chem. Rev.*, vol. 111, no. 6, pp. 3913–3961, 2011.

[44] A. Moreau, C. Ciracì, J. J. Mock, R. T. Hill, Q. Wang, B. J. Wiley, A. Chilkoti, and D. R. Smith, “Controlled-reflectance surfaces with film-coupled colloidal nanoantennas.,” *Nature*, vol. 492, no. 7427, pp. 86–9, Dec. 2012.

[45] C. Ciracì, X. Chen, J. J. Mock, F. McGuire, X. Liu, S.-H. Oh, and D. R. Smith, “Film-coupled nanoparticles by atomic layer deposition: Comparison with organic spacing layers,” *Appl. Phys. Lett.*, vol. 104, no. 2, p. 023109, Jan. 2014.

[46] C. Ciracì, R. T. Hill, J. J. Mock, Y. Urzhumov, a I. Fernández-Domínguez, S. a Maier, J. B. Pendry, a Chilkoti, and D. R. Smith, “Probing the ultimate limits of plasmonic enhancement.,” *Science*, vol. 337, no. 6098, pp. 1072–4, Aug. 2012.

[47] J. Valentine, S. Zhang, T. Zentgraf, E. Ulin-Avila, D. A. Genov, G. Bartal, and X. Zhang, “Three-dimensional optical metamaterial with a negative refractive index.,” *Nature*, vol. 455, no. 7211, pp. 376–9, Sep. 2008.

[48] S. Xiao, V. P. Drachev, A. V Kildishev, X. Ni, U. K. Chettiar, H.-K. Yuan, and V. M. Shalaev, "Loss-free and active optical negative-index metamaterials.," *Nature*, vol. 466, no. 7307, pp. 735–8, Aug. 2010.

[49] Y. Wang, T. Sun, T. Paudel, Y. Zhang, Z. Ren, and K. Kempa, "Metamaterial-plasmonic absorber structure for high efficiency amorphous silicon solar cells.," *Nano Lett.*, vol. 12, no. 1, pp. 440–5, Jan. 2012.

[50] A. Tittl, P. Mai, R. Taubert, D. Dregely, N. Liu, and H. Giessen, "Palladium-based plasmonic perfect absorber in the visible wavelength range and its application to hydrogen sensing.," *Nano Lett.*, vol. 11, no. 10, pp. 4366–9, Oct. 2011.

[51] M. Khorasaninejad, S. Mohsen Raeis-Zadeh, H. Amarloo, N. Abedzadeh, S. Safavi-Naeini, and S. S. Saini, "Colorimetric sensors using nano-patch surface plasmon resonators.," *Nanotechnology*, vol. 24, no. 35, p. 355501, 2013.

[52] H. Chalabi, D. Schoen, and M. L. Brongersma, "Hot-electron photodetection with a plasmonic nanostripe antenna.," *Nano Lett.*, vol. 14, no. 3, pp. 1374–80, Mar. 2014.

[53] Y. Chu, M. G. Banaee, and K. B. Crozier, "Double-Resonance Plasmon Substrates for Surface-Enhanced Raman Scattering Stokes Frequencies," *ACS Nano*, vol. 4, no. 5, pp. 2804–2810, 2010.

[54] K. Chen, R. Adato, and H. Altug, "Dual-band perfect absorber for multispectral plasmon-enhanced infrared spectroscopy.," *ACS Nano*, vol. 6, no. 9, pp. 7998–8006, Sep. 2012.

[55] A. J. Qavi, A. L. Washburn, J. Y. Byeon, and R. C. Bailey, "Label-free technologies for quantitative multiparameter biological analysis," *Anal. Bioanal. Chem.*, vol. 394, no. 1, pp. 121–135, 2009.

[56] O. Tokel, F. Inci, and U. Demirci, "Advances in plasmonic technologies for point of care applications," *Chem. Rev.*, vol. 114, no. 11, pp. 5728–5752, 2014.

[57] D. L. Jeanmaire and R. P. Van Duyne, "Surface raman spectroelectrochemistry," *J. Electroanal. Chem. Interfacial Electrochem.*, vol. 84, no. 1, pp. 1–20, Nov. 1977.

[58] T. R. Jensen, R. P. Van Duyne, S. A. Johnson, and V. A. Maroni, "Surface-Enhanced Infrared Spectroscopy: A Comparison of Metal Island Films with Discrete and Nondiscrete Surface Plasmons," *Appl. Spectrosc.*, vol. 54, no. 3, pp. 371–377, Mar. 2000.

[59] A. D. McFarland and R. P. Van Duyne, "Single Silver Nanoparticles as Real-Time Optical Sensors with Zeptomole Sensitivity," *Nano Lett.*, vol. 3, no. 8, pp. 1057–1062, Aug. 2003.

[60] M. G. Banaee and K. B. Crozier, “Mixed dimer double-resonance substrates for surface-enhanced Raman spectroscopy.,” *ACS Nano*, vol. 5, no. 1, pp. 307–14, Jan. 2011.

[61] E. Kim, F. Wang, W. Wu, Z. Yu, and Y. Shen, “Nonlinear optical spectroscopy of photonic metamaterials,” *Phys. Rev. B*, vol. 78, no. 11, Sep. 2008.

[62] C. Kendall, M. Isabelle, F. Bazant-Hegemark, J. Hutchings, L. Orr, J. Babrah, R. Baker, and N. Stone, “Vibrational spectroscopy: a clinical tool for cancer diagnostics.,” *Analyst*, vol. 134, no. 6, pp. 1029–45, Jun. 2009.

[63] C. D. Andrea, A. Toma, C. Huck, F. Neubrech, E. Messina, E. Di Fabrizio, M. Lamy, D. La Chapelle, P. G. Gucciardi, B. Fazio, and O. M. Marago, “Optical Nanoantennas for Multiband Surface-Enhanced Infrared and Raman Spectroscopy,” *ACS Nano*, vol. 7, no. 4, pp. 3522–3531, 2013.

[64] R. Adato, A. a Yanik, J. J. Amsden, D. L. Kaplan, F. G. Omenetto, M. K. Hong, S. Erramilli, and H. Altug, “Ultra-sensitive vibrational spectroscopy of protein monolayers with plasmonic nanoantenna arrays.,” *Proc. Natl. Acad. Sci. U. S. A.*, vol. 106, no. 46, pp. 19227–32, Nov. 2009.

[65] Y. Ishino and H. Ishida, “Grazing Angle Metal-Overlayer Infrared ATR Spectroscopy,” *Appl. Spectrosc.*, vol. 42, no. 7, pp. 1296–1302, Sep. 1988.

[66] J. Kundu, F. Le, P. Nordlander, and N. J. Halas, “Surface enhanced infrared absorption (SEIRA) spectroscopy on nanoshell aggregate substrates,” *Chem. Phys. Lett.*, vol. 452, no. 1–3, pp. 115–119, Feb. 2008.

[67] L. V Brown, K. Zhao, N. King, H. Sobhani, P. Nordlander, and N. J. Halas, “Surface-enhanced infrared absorption using individual cross antennas tailored to chemical moieties.,” *J. Am. Chem. Soc.*, vol. 135, no. 9, pp. 3688–95, Mar. 2013.

[68] F. P. Garcia de Arquer, A. Mihi, D. Kufer, and G. Konstantatos, “Photoelectric Energy Conversion of Plasmon-Generated Hot Carriers in,” *ACS Nano*, vol. 7, no. 4, pp. 3581–3588, 2013.

[69] A. K. Pradhan, T. Holloway, R. Mundle, H. Dondapati, and M. Bahoura, “Energy harvesting in semiconductor-insulator-semiconductor junctions through excitation of surface plasmon polaritons,” *Appl. Phys. Lett.*, vol. 100, no. 6, p. 061127, Feb. 2012.

[70] S. Mubeen, J. Lee, N. Singh, S. Krämer, G. D. Stucky, and M. Moskovits, “An autonomous photosynthetic device in which all charge carriers derive from surface plasmons.,” *Nat. Nanotechnol.*, vol. 8, no. 4, pp. 247–51, Apr. 2013.

[71] F. Wang and N. A. Melosh, “Plasmonic energy collection through hot carrier extraction.,” *Nano Lett.*, vol. 11, no. 12, pp. 5426–30, Dec. 2011.

[72] H. A. Atwater and A. Polman, “Plasmonics for improved photovoltaic devices.,” *Nat. Mater.*, vol. 9, no. 3, pp. 205–13, Mar. 2010.

[73] F. Wang and N. A. Melosh, “Power-independent wavelength determination by hot carrier collection in metal-insulator-metal devices.,” *Nat. Commun.*, vol. 4, p. 1711, Jan. 2013.

[74] M. A. Kats, R. Blanchard, P. Genevet, and F. Capasso, “Nanometre optical coatings based on strong interference effects in highly absorbing media.,” *Nat. Mater.*, vol. 12, no. 1, pp. 20–4, Jan. 2013.

[75] M. A. Kats, R. Blanchard, S. Ramanathan, and F. Capasso, “Thin-Film Interference in Lossy, Ultra-Thin Layers,” *Opt. Photonics News*, vol. 25, p. 40, 2014.

[76] F. F. Schlich and R. Spolenak, “Strong interference in ultrathin semiconducting layers on a wide variety of substrate materials,” *Appl. Phys. Lett.*, vol. 103, no. 21, p. 213112, Nov. 2013.

[77] H. Song, L. Guo, Z. Liu, K. Liu, X. Zeng, D. Ji, N. Zhang, H. Hu, S. Jiang, and Q. Gan, “Nanocavity enhancement for ultra-thin film optical absorber,” *Adv. Mater.*, vol. 26, no. 17, pp. 2737–2743, 2014.

[78] M. A. Kats, S. J. Byrnes, R. Blanchard, M. Kolle, P. Genevet, J. Aizenberg, and F. Capasso, “Enhancement of absorption and color contrast in ultra-thin highly absorbing optical coatings,” *Appl. Phys. Lett.*, vol. 103, no. 10, p. 101104, 2013.

[79] S. A. Maier, “Plasmonics: Fundamentals and Applications,” *Springer*, 2007.

[80] W. L. Barnes, A. Dereux, and T. W. Ebbesen, “Surface plasmon subwavelength optics.,” *Nature*, vol. 424, no. 6950, pp. 824–30, Aug. 2003.

[81] A. K. Popov, S. A. Myslivets, T. F. George, and V. M. Shalaev, “Four-wave mixing, quantum control, and compensating losses in doped negative-index photonic metamaterials,” *Opt. Lett.*, vol. 32, no. 20, p. 3044, Oct. 2007.

[82] S. Palomba, S. Zhang, Y. Park, G. Bartal, X. Yin, and X. Zhang, “Optical negative refraction by four-wave mixing in thin metallic nanostructures.,” *Nat. Mater.*, vol. 11, no. 1, pp. 34–8, Jan. 2012.

[83] J. T. Choy, B. J. M. Hausmann, T. M. Babinec, I. Bulu, M. Khan, P. Maletinsky, A. Yacoby, and M. Lončar, “Enhanced single-photon emission from a diamond–silver aperture,” *Nat. Photonics*, vol. 5, no. 12, pp. 738–743, Oct. 2011.

[84] I. L. Chuang and Y. Yamamoto, “Simple quantum computer,” *Phys. Rev. A*, vol. 52, no. 5, pp. 3489–3496, Nov. 1995.

[85] K. Kneipp, Y. Wang, H. Kneipp, L. Perelman, I. Itzkan, R. Dasari, and M. Feld, "Single Molecule Detection Using Surface-Enhanced Raman Scattering (SERS)," *Phys. Rev. Lett.*, vol. 78, no. 9, pp. 1667–1670, Mar. 1997.

[86] S. Nie, "Probing Single Molecules and Single Nanoparticles by Surface-Enhanced Raman Scattering," *Science (80-.).*, vol. 275, no. 5303, pp. 1102–1106, Feb. 1997.

[87] Y. Fang, N.-H. Seong, and D. D. Dlott, "Measurement of the Distribution of Site Enhancements in Surface-Enhanced Raman Scattering," *Science (80-.).*, vol. 321, no. 5887, pp. 388–392, Jul. 2008.

[88] J. J. Baumberg, T. A. Kelf, Y. Sugawara, S. Cintra, M. E. Abdelsalam, P. N. Bartlett, and A. E. Russell, "Angle-resolved surface-enhanced Raman scattering on metallic nanostructured plasmonic crystals.," *Nano Lett.*, vol. 5, no. 11, pp. 2262–7, Nov. 2005.

[89] A. Kocabas, G. Ertas, S. S. Senlik, and A. Aydinli, "Plasmonic band gap structures for surface-enhanced Raman scattering," *Opt. Express*, vol. 16, no. 17, p. 12469, Aug. 2008.

[90] W. J. Cho, Y. Kim, and J. K. Kim, "Ultrahigh Density Array of Silver Nanoclusters for SERS Substrate with High Sensitivity and Excellent Reproducibility.," *ACS Nano*, vol. 6, no. 1, pp. 249–255, Nov. 2011.

[91] I. P. Kaminow, W. L. Mammel, and H. P. Weber, "Metal-clad optical waveguides: analytical and experimental study.," *Appl. Opt.*, vol. 13, no. 2, pp. 396–405, Feb. 1974.

[92] Y. Todorov, L. Tosetto, J. Teissier, A. M. Andrews, P. Klang, R. Colombelli, I. Sagnes, G. Strasser, and C. Sirtori, "Optical properties of metal-dielectric-metal microcavities in the THz frequency range," *Opt. Express*, vol. 18, no. 13, p. 13886, Jun. 2010.

[93] N. Engheta, A. Salandrino, and A. Alù, "Circuit Elements at Optical Frequencies: Nanoinductors, Nanocapacitors, and Nanoresistors," *Phys. Rev. Lett.*, vol. 95, no. 9, Aug. 2005.

[94] J. Zhou, E. N. Economon, T. Koschny, and C. M. Soukoulis, "Unifying approach to left-handed material design," *Opt. Lett.*, vol. 31, no. 24, p. 3620, Dec. 2006.

[95] L. Fu, H. Schweizer, H. Guo, N. Liu, and H. Giessen, "Synthesis of transmission line models for metamaterial slabs at optical frequencies," *Phys. Rev. B*, vol. 78, no. 11, Sep. 2008.

[96] Y. Chu, D. Wang, W. Zhu, and K. B. Crozier, "Double resonance surface enhanced Raman scattering substrates: an intuitive coupled oscillator model," *Opt. Express*, vol. 19, no. 16, p. 14919, Jul. 2011.

[97] M. Pu, C. Hu, M. Wang, C. Huang, Z. Zhao, C. Wang, Q. Feng, and X. Luo, "Design principles for infrared wide-angle perfect absorber based on plasmonic structure," *Opt. Express*, vol. 19, no. 18, p. 17413, Aug. 2011.

[98] H. T. Miyazaki and Y. Kurokawa, "Squeezing Visible Light Waves into a 3-nm-Thick and 55-nm-Long Plasmon Cavity," *Phys. Rev. Lett.*, vol. 96, no. 9, p. 097401, Mar. 2006.

[99] H. Liu, D. Genov, D. Wu, Y. Liu, J. Steele, C. Sun, S. Zhu, and X. Zhang, "Magnetic Plasmon Propagation Along a Chain of Connected Subwavelength Resonators at Infrared Frequencies," *Phys. Rev. Lett.*, vol. 97, no. 24, Dec. 2006.

[100] A. Yariv, Y. Xu, R. K. Lee, and A. Scherer, "Coupled-resonator optical waveguide: a proposal and analysis," *Opt. Lett.*, vol. 24, no. 11, p. 711, Jun. 1999.

[101] A. N. Grigorenko, A. K. Geim, H. F. Gleeson, Y. Zhang, A. A. Firsov, I. Y. Khrushchev, and J. Petrovic, "Nanofabricated media with negative permeability at visible frequencies.," *Nature*, vol. 438, no. 7066, pp. 335–8, Nov. 2005.

[102] V. Giannini, G. Vecchi, and J. Gómez Rivas, "Lighting Up Multipolar Surface Plasmon Polaritons by Collective Resonances in Arrays of Nanoantennas," *Phys. Rev. Lett.*, vol. 105, no. 26, Dec. 2010.

[103] B. Auguié and W. Barnes, "Collective Resonances in Gold Nanoparticle Arrays," *Phys. Rev. Lett.*, vol. 101, no. 14, Sep. 2008.

[104] E. Feigenbaum and H. A. Atwater, "Resonant Guided Wave Networks," *Phys. Rev. Lett.*, vol. 104, no. 14, p. 147402, Apr. 2010.

[105] K. Aydin, V. E. Ferry, R. M. Briggs, and H. A. Atwater, "Broadband polarization-independent resonant light absorption using ultrathin plasmonic super absorbers," *Nat. Commun.*, vol. 2, p. 517, Nov. 2011.

[106] S. Wang, X. Shan, U. Patel, X. Huang, J. Lu, J. Li, and N. Tao, "Label-free imaging, detection, and mass measurement of single viruses by surface plasmon resonance.," *Proc. Natl. Acad. Sci. U. S. A.*, vol. 107, no. 37, pp. 16028–32, Sep. 2010.

[107] N. Liu, M. L. Tang, M. Hentschel, H. Giessen, and A. P. Alivisatos, "Nanoantenna-enhanced gas sensing in a single tailored nanofocus.," *Nat. Mater.*, vol. 10, no. 8, pp. 631–636, May 2011.

[108] T. V. Teperik, F. J. García de Abajo, a. G. Borisov, M. Abdelsalam, P. N. Bartlett, Y. Sugawara, and J. J. Baumberg, "Omnidirectional absorption in nanostructured metal surfaces," *Nat. Photonics*, vol. 2, no. 5, pp. 299–301, Apr. 2008.

[109] E. Cubukcu, S. Zhang, Y.-S. Park, G. Bartal, and X. Zhang, “Split ring resonator sensors for infrared detection of single molecular monolayers,” *Appl. Phys. Lett.*, vol. 95, no. 4, p. 043113, Jul. 2009.

[110] C. Cao, J. Zhang, X. Wen, S. L. Dodson, N. T. Dao, L. M. Wong, S. Wang, S. Li, T. A. Phan, and Q. Xiong, “Metamaterials-BasedLabel-Free Nanosensors for Conformation and Affinity Biosensing,” *ACS Nano*, vol. 7, no. 9, pp. 7583–7591, 2013.

[111] F. B. P. Niesler, J. K. Gansel, S. Fischbach, and M. Wegener, “Metamaterial metal-based bolometers,” *Appl. Phys. Lett.*, vol. 100, no. 20, p. 203508, 2012.

[112] V. Savinov, V. a Fedotov, P. a J. de Groot, and N. I. Zheludev, “Radiation-harvesting resonant superconducting sub-THz metamaterial bolometer,” *Supercond. Sci. Technol.*, vol. 26, no. 8, p. 084001, Aug. 2013.

[113] N. Landy, S. Sajuyigbe, J. Mock, D. Smith, and W. Padilla, “Perfect Metamaterial Absorber,” *Phys. Rev. Lett.*, vol. 100, no. 20, p. 207402, May 2008.

[114] J. W. Park, P. Van Tuong, J. Y. Rhee, K. W. Kim, W. H. Jang, E. H. Choi, L. Y. Chen, and Y. Lee, “Multi-band metamaterial absorber based on the arrangement of donut-type resonators,” *Opt. Express*, vol. 21, no. 8, pp. 9691–9702, 2013.

[115] H. Wakatsuchi, S. Greedy, C. Christopoulos, and J. Paul, “Customised broadband metamaterial absorbers for arbitrary polarisation.,” *Opt. Express*, vol. 18, no. 21, pp. 22187–98, Oct. 2010.

[116] M. Diem, T. Koschny, and C. Soukoulis, “Wide-angle perfect absorber/thermal emitter in the terahertz regime,” *Phys. Rev. B*, vol. 79, no. 3, p. 033101, Jan. 2009.

[117] H. Tao, N. I. Landy, C. M. Bingham, X. Zhang, R. D. Averitt, and W. J. Padilla, “A metamaterial absorber for the terahertz regime : Design , fabrication and characterization Abstract :,” vol. 16, no. 10, pp. 1494–1496, 2008.

[118] J. Hao, J. Wang, X. Liu, W. J. Padilla, L. Zhou, and M. Qiu, “High performance optical absorber based on a plasmonic metamaterial,” *Appl. Phys. Lett.*, vol. 96, no. 25, p. 251104, Jun. 2010.

[119] X. Liu, T. Starr, A. F. Starr, and W. J. Padilla, “Infrared Spatial and Frequency Selective Metamaterial with Near-Unity Absorbance,” *Phys. Rev. Lett.*, vol. 104, no. 20, p. 207403, May 2010.

[120] J. Hao, L. Zhou, and M. Qiu, “Nearly total absorption of light and heat generation by plasmonic metamaterials,” *Phys. Rev. B*, vol. 83, no. 16, p. 165107, Apr. 2011.

[121] X. Liu, T. Tyler, T. Starr, A. F. Starr, N. M. Jokerst, and W. J. Padilla, "Taming the Blackbody with Infrared Metamaterials as Selective Thermal Emitters," *Phys. Rev. Lett.*, vol. 107, no. 4, p. 045901, Jul. 2011.

[122] R. Alaee, C. Menzel, C. Rockstuhl, and F. Lederer, "Perfect absorbers on curved surfaces and their potential applications," *Opt. Express*, vol. 20, no. 16, p. 18370, Jul. 2012.

[123] L. P. Wang and Z. M. Zhang, "Wavelength-selective and diffuse emitter enhanced by magnetic polaritons for thermophotovoltaics," *Appl. Phys. Lett.*, vol. 100, no. 6, p. 063902, Feb. 2012.

[124] P. Zhu and L. Jay Guo, "High performance broadband absorber in the visible band by engineered dispersion and geometry of a metal-dielectric-metal stack," *Appl. Phys. Lett.*, vol. 101, no. 24, p. 241116, 2012.

[125] M. G. Nielsen, A. Pors, O. Albrektsen, and S. I. Bozhevolnyi, "Efficient absorption of visible radiation by gap plasmon resonators.," *Opt. Express*, vol. 20, no. 12, pp. 13311–9, Jun. 2012.

[126] J. Wang, C. Fan, P. Ding, J. He, Y. Cheng, W. Hu, G. Cai, E. Liang, and Q. Xue, "Tunable broad-band perfect absorber by exciting of multiple plasmon resonances at optical frequency," *Opt. Express*, vol. 20, no. 14, p. 14871, Jun. 2012.

[127] K. Aydin, V. E. Ferry, R. M. Briggs, and H. a Atwater, "Broadband polarization-independent resonant light absorption using ultrathin plasmonic super absorbers.," *Nat. Commun.*, vol. 2, p. 517, Jan. 2011.

[128] J. A. Bossard, L. Lin, S. Yun, L. Liu, D. H. Werner, and T. S. Mayer, "Near-Ideal Optical Metamaterial Bandwidth," *ACS Nano*, vol. 8, no. 2, pp. 1517–1524, 2014.

[129] R. Alaee, C. Menzel, U. Huebner, E. Pshenay-Severin, S. Bin Hasan, T. Pertsch, C. Rockstuhl, and F. Lederer, "Deep-subwavelength plasmonic nanoresonators exploiting extreme coupling.," *Nano Lett.*, vol. 13, no. 8, pp. 3482–6, Aug. 2013.

[130] X. Wang, C. Luo, G. Hong, and X. Zhao, "Metamaterial optical refractive index sensor detected by the naked eye," *Appl. Phys. Lett.*, vol. 102, no. 9, p. 091902, 2013.

[131] M. K. Hedayati, M. Javaherirahim, B. Mozooni, R. Abdelaziz, A. Tavassolizadeh, V. S. K. Chakravadhanula, V. Zaporojtchenko, T. Strunkus, F. Faupel, and M. Elbahri, "Design of a perfect black absorber at visible frequencies using plasmonic metamaterials.," *Adv. Mater.*, vol. 23, no. 45, pp. 5410–4, Dec. 2011.

[132] M. Elbahri, M. K. Hedayati, V. S. Kiran Chakravadhanula, M. Jamali, T. Strunkus, V. Zaporojtchenko, and F. Faupel, "An omnidirectional transparent

conducting-metal-based plasmonic nanocomposite.," *Adv. Mater.*, vol. 23, no. 17, pp. 1993–7, May 2011.

[133] A. Moreau, C. Ciracì, J. J. Mock, R. T. Hill, Q. Wang, B. J. Wiley, A. Chilkoti, and D. R. Smith, "Controlled-reflectance surfaces with film-coupled colloidal nanoantennas.," *Nature*, vol. 492, no. 7427, pp. 86–9, Dec. 2012.

[134] Z. H. Jiang, S. Yun, F. Toor, D. H. Werner, and T. S. Mayer, "Conformal Dual-Band Near-Perfectly Coating," *ACS Nano*, vol. 5, no. 6, pp. 4641–4647, 2011.

[135] Y. Cui, K. H. Fung, J. Xu, H. Ma, Y. Jin, S. He, and N. Fang, "Ultra-broadband Light Absorption by a Sawtooth Anisotropic Metamaterial Slab.," *Nano Lett.*, Feb. 2012.

[136] B. Zhang, Y. Zhao, Q. Hao, B. Kiraly, I.-C. Khoo, S. Chen, and T. J. Huang, "Polarization-independent dual-band infrared perfect absorber based on a metal-dielectric-metal elliptical nanodisk array," *Opt. Express*, vol. 19, no. 16, p. 15221, Jul. 2011.

[137] C.-W. Cheng, M. N. Abbas, C.-W. Chiu, K.-T. Lai, M.-H. Shih, and Y.-C. Chang, "Wide-angle polarization independent infrared broadband absorbers based on metallic multi-sized disk arrays," *Opt. Express*, vol. 20, no. 9, p. 10376, Apr. 2012.

[138] J. Hendrickson, J. Guo, B. Zhang, W. Buchwald, and R. Soref, "Wideband perfect light absorber at midwave infrared using multiplexed metal structures.," *Opt. Lett.*, vol. 37, no. 3, pp. 371–3, Feb. 2012.

[139] E. Lansey, I. R. Hooper, J. N. Gollub, A. P. Hibbins, and D. T. Crouse, "Light localization, photon sorting, and enhanced absorption in subwavelength cavity arrays.," *Opt. Express*, vol. 20, no. 22, pp. 24226–36, Oct. 2012.

[140] J. Le Perchec, Y. Desieres, N. Rochat, and R. Espiau de Lamaestre, "Subwavelength optical absorber with an integrated photon sorter," *Appl. Phys. Lett.*, vol. 100, no. 11, p. 113305, 2012.

[141] W. Ma, Y. Wen, and X. Yu, "Broadband metamaterial absorber at mid-infrared using multiplexed cross resonators," *Opt. Express*, vol. 21, no. 25, pp. 154–156, 2013.

[142] H. Ko, D.-H. Ko, Y. Cho, and I. K. Han, "Broadband light absorption using a multilayered gap surface plasmon resonator," *Appl. Phys. A*, no. Mmdm, May 2014.

[143] P. Pitchappa, C. P. Ho, P. Kropelnicki, N. Singh, D.-L. Kwong, and C. Lee, "Dual band complementary metamaterial absorber in near infrared region," *J. Appl. Phys.*, vol. 115, no. 19, p. 193109, May 2014.

[144] S. Ayas, H. Guner, B. Turker, O. O. Ekiz, F. Dirisaglik, A. K. Okyay, and A. Dana, “Raman Enhancement on a Broadband,” *ACS Nano*, vol. 6, no. 8, pp. 6852–6861, 2012.

[145] D. Li, L. Qin, X. Xiong, R.-W. Peng, Q. Hu, G.-B. Ma, H.-S. Zhou, and M. Wang, “Exchange of electric and magnetic resonances in multilayered metal/dielectric nanoplates,” *Opt. Express*, vol. 19, no. 23, p. 22942, Oct. 2011.

[146] C. Koechlin, P. Bouchon, F. Pardo, J. Pelouard, and R. Ha, “Analytical description of subwavelength plasmonic MIM resonators and of their combination Abstract :,” vol. 21, no. 6, pp. 4641–4647, 2013.

[147] R. Filter, C. Rockstuhl, and F. Lederer, “Circular Optical Nanoantennas - An Analytical Theory,” *Phys. Rev. B*, vol. 85, no. 125429, pp. 1–16, 1887.

[148] F. Minkowski, F. Wang, A. Chakrabarty, and Q.-H. Wei, “Resonant cavity modes of circular plasmonic patch nanoantennas,” *Appl. Phys. Lett.*, vol. 104, no. 2, p. 021111, Jan. 2014.

[149] J. G. Bergman, D. S. Chemla, P. F. Liao, A. M. Glass, A. Pinczuk, R. M. Hart, and D. H. Olson, “Relationship between surface-enhanced Raman scattering and the dielectric properties of aggregated silver films,” *Opt. Lett.*, vol. 6, no. 1, p. 33, Jan. 1981.

[150] A. I. Maaroof and D. S. Sutherland, “Optimum plasmon hybridization at percolation threshold of silver films near metallic surfaces,” *J. Phys. D. Appl. Phys.*, vol. 43, no. 40, p. 405301, Oct. 2010.

[151] J. J. Mock, R. T. Hill, A. Degiron, S. Zauscher, A. Chilkoti, and D. R. Smith, “Distance-dependent plasmon resonant coupling between a gold nanoparticle and gold film.,” *Nano Lett.*, vol. 8, no. 8, pp. 2245–52, Aug. 2008.

[152] S. Mubeen, S. Zhang, N. Kim, S. Lee, S. Krämer, H. Xu, and M. Moskovits, “Plasmonic properties of gold nanoparticles separated from a gold mirror by an ultrathin oxide.,” *Nano Lett.*, vol. 12, no. 4, pp. 2088–94, Apr. 2012.

[153] D. Y. Lei, A. I. Fernandez-Dominguez, Y. Sonnefraud, K. Appavoo, R. F. Haglund, J. B. Pendry, and S. A. Maier, “Revealing Plasmonic Gap Modes in Particle-on-Film Systems Using Dark-Field Spectroscopy.,” *ACS Nano*, Jan. 2012.

[154] N. M. B. Perney, J. J. Baumberg, M. E. Zoorob, M. D. B. Charlton, S. Mahnkopf, and C. M. Netti, “Tuning localized plasmons in nanostructured substrates for surface-enhanced Raman scattering,” *Opt. Express*, vol. 14, no. 2, p. 847, Jan. 2006.

[155] J. A. Dieringer, R. B. Lettan, K. A. Scheidt, and R. P. Van Duyne, “A frequency domain existence proof of single-molecule surface-enhanced

Raman spectroscopy.," *J. Am. Chem. Soc.*, vol. 129, no. 51, pp. 16249–56, Dec. 2007.

[156] S. R. Emory, R. A. Jensen, T. Wenda, M. Han, and S. Nie, "Re-examining the origins of spectral blinking in single-molecule and single-nanoparticleSERS," *Faraday Discuss.*, vol. 132, pp. 249–259, Apr. 2006.

[157] Z. Wang and L. J. Rothberg, "Origins of blinking in single-molecule Raman spectroscopy.," *J. Phys. Chem. B*, vol. 109, no. 8, pp. 3387–91, Mar. 2005.

[158] E. C. Le Ru, M. Meyer, and P. G. Etchegoin, "Proof of single-molecule sensitivity in surface enhanced Raman scattering (SERS) by means of a two-analyte technique.," *J. Phys. Chem. B*, vol. 110, no. 4, pp. 1944–8, Feb. 2006.

[159] K. A. Bosnick and L. E. Brus, "Fluctuations and Local Symmetry in Single-Molecule Rhodamine 6G Raman Scattering on Silver Nanocrystal Aggregates †," *J. Phys. Chem. B*, vol. 106, no. 33, pp. 8096–8099, Aug. 2002.

[160] S. Khatua and M. Orrit, "Toward single-molecule microscopy on a smart phone.," *ACS Nano*, vol. 7, no. 10, pp. 8340–3, Oct. 2013.

[161] A. Otto, "Theory of First Layer and Single Molecule Surface Enhanced Raman Scattering (SERS)," *Phys. status solidi*, vol. 188, no. 4, pp. 1455–1470, Dec. 2001.

[162] Y. Maruyama, M. Ishikawa, and M. Futamata, "Thermal Activation of Blinking in SERS Signal," *J. Phys. Chem. B*, vol. 108, no. 2, pp. 673–678, Jan. 2004.

[163] P. C. Andersen, M. L. Jacobson, and K. L. Rowlen, "Flashy Silver Nanoparticles," *J. Phys. Chem. B*, vol. 108, no. 7, pp. 2148–2153, Feb. 2004.

[164] Y. Shirai, A. J. Osgood, Y. Zhao, K. F. Kelly, and J. M. Tour, "Directional control in thermally driven single-molecule nanocars.," *Nano Lett.*, vol. 5, no. 11, pp. 2330–4, Nov. 2005.

[165] M. Schunack, T. R. Linderoth, F. Rosei, E. Lægsgaard, I. Stensgaard, and F. Besenbacher, "Long Jumps in the Surface Diffusion of Large Molecules," *Phys. Rev. Lett.*, vol. 88, no. 15, p. 156102, Mar. 2002.

[166] J. Weckesser, J. V. Barth, and K. Kern, "Direct observation of surface diffusion of large organic molecules at metal surfaces: PVBA on Pd(110)," *J. Chem. Phys.*, vol. 110, no. 11, p. 5351, Mar. 1999.

[167] A. Otto, "What is observed in single molecule SERS, and why?," *J. Raman Spectrosc.*, vol. 33, no. 8, pp. 593–598, Aug. 2002.

[168] S. K. Brown, M. R. Sim, M. J. Abramson, and C. N. Gray, "Concentrations of Volatile Organic Compounds in Indoor Air - A Review," *Indoor Air*, vol. 4, no. 2, pp. 123–134, Jun. 1994.

[169] M. Phillips, J. Herrera, S. Krishnan, M. Zain, J. Greenberg, and R. N. Cataneo, "Variation in volatile organic compounds in the breath of normal humans," *J. Chromatogr. B Biomed. Sci. Appl.*, vol. 729, no. 1–2, pp. 75–88, Jun. 1999.

[170] A. Kinkhabwala, Z. Yu, S. Fan, Y. Avlasevich, K. Müllen, and W. E. Moerner, "Large single-molecule fluorescence enhancements produced by a bowtie nanoantenna," *Nat. Photonics*, vol. 3, no. 11, pp. 654–657, Oct. 2009.

[171] R. Henriques, M. Lelek, E. F. Fornasiero, F. Valtorta, C. Zimmer, and M. M. Mhlanga, "QuickPALM: 3D real-time photoactivation nanoscopy image processing in ImageJ.," *Nat. Methods*, vol. 7, no. 5, pp. 339–40, May 2010.

[172] D. Gallegos, K. D. Long, H. Yu, P. P. Clark, Y. Lin, S. George, P. Nath, and B. T. Cunningham, "Label-free biodetection using a smartphone.," *Lab Chip*, vol. 13, no. 11, pp. 2124–32, Jun. 2013.

[173] A. Otto, "The 'chemical' (electronic) contribution to surface-enhanced Raman scattering," *J. Raman Spectrosc.*, vol. 36, no. 6–7, pp. 497–509, Jun. 2005.

[174] S. A. Maier and H. A. Atwater, "Plasmonics: Localization and guiding of electromagnetic energy in metal/dielectric structures," *J. Appl. Phys.*, vol. 98, no. 1, p. 011101, Jul. 2005.

[175] J. A. Schuller, E. S. Barnard, W. Cai, Y. C. Jun, J. S. White, and M. L. Brongersma, "Plasmonics for extreme light concentration and manipulation.," *Nat. Mater.*, vol. 9, no. 3, pp. 193–204, Mar. 2010.

[176] H. A. Atwater and A. Polman, "Plasmonics for improved photovoltaic devices.," *Nat. Mater.*, vol. 9, no. 3, pp. 205–13, Mar. 2010.

[177] F. Wang and N. A. Melosh, "Power-independent wavelength determination by hot carrier collection in metal-insulator-metal devices.," *Nat. Commun.*, vol. 4, p. 1711, 2013.

[178] K. Kempa, M. J. Naughton, Z. F. Ren, A. Herczynski, T. Kirkpatrick, J. Rybczynski, and Y. Gao, "Hot electron effect in nanoscopically thin photovoltaic junctions," *Appl. Phys. Lett.*, vol. 95, no. 23, p. 233121, Dec. 2009.

[179] F. Wang and N. A. Melosh, "Plasmonic energy collection through hot carrier extraction.," *Nano Lett.*, vol. 11, no. 12, pp. 5426–30, Dec. 2011.

[180] M. A. Green, "Third generation photovoltaics: Ultra-high conversion efficiency at low cost," *Prog. Photovoltaics Res. Appl.*, vol. 9, no. 2, pp. 123–135, Mar. 2001.

[181] F. B. Atar, E. Battal, L. E. Aygun, B. Daglar, M. Bayindir, and A. K. Okyay, "Plasmonically enhanced hot electron based photovoltaic device," *Opt. Express*, vol. 21, no. 6, p. 7196, Mar. 2013.

[182] T. P. White and K. R. Catchpole, “Plasmon-enhanced internal photoemission for photovoltaics: Theoretical efficiency limits,” *Appl. Phys. Lett.*, vol. 101, no. 7, p. 073905, Aug. 2012.

[183] Y. H. Wang, H. Steinberg, P. Jarillo-Herrero, and N. Gedik, “Observation of Floquet-Bloch states on the surface of a topological insulator.,” *Science*, vol. 342, no. 6157, pp. 453–7, Oct. 2013.

[184] J. Cao, Y. Gao, R. J. D. Miller, H. E. Elsayed-Ali, and D. A. Mantell, “Femtosecond photoemission study of ultrafast electron dynamics on Cu(100),” *Phys. Rev. B*, vol. 56, no. 3, pp. 1099–1102, Jul. 1997.

[185] M. Bauer, C. Lei, K. Read, R. Tobey, J. Gland, M. M. Murnane, and H. C. Kapteyn, “Direct Observation of Surface Chemistry Using Ultrafast Soft-X-Ray Pulses,” *Phys. Rev. Lett.*, vol. 87, no. 2, p. 025501, Jun. 2001.

[186] O. O. Ekiz, K. Mizrak, and A. Dâna, “Chemically specific dynamic characterization of photovoltaic and photoconductivity effects of surface nanostructures.,” *ACS Nano*, vol. 4, no. 4, pp. 1851–60, Apr. 2010.

[187] H. Sezen, A. A. Rockett, and S. Suzer, “XPS Investigation of a CdS-Based Photoresistor under Working Conditions: Operando–XPS,” *Anal. Chem.*, vol. 84, no. 6, pp. 2990–2994, Mar. 2012.

[188] H. Sezen and S. Suzer, “Charging/discharging dynamics of CdS and CdSe films under photoillumination using dynamic x-ray photoelectron spectroscopy,” *J. Vac. Sci. Technol. A Vacuum, Surfaces, Film.*, vol. 28, no. 4, p. 639, Jun. 2010.

[189] S. Suzer, H. Sezen, and A. Dâna, “Two-dimensional X-ray photoelectron spectroscopy for composite surface analysis.,” *Anal. Chem.*, vol. 80, no. 10, pp. 3931–6, May 2008.

[190] S. Suzer and A. Dâna, “X-ray photoemission for probing charging/discharging dynamics.,” *J. Phys. Chem. B*, vol. 110, no. 39, pp. 19112–5, Oct. 2006.

[191] S. Ayas, H. Güner, B. Türker, O. Ö. Ekiz, F. Dirisaglik, A. K. Okyay, and A. Dâna, “Raman Enhancement on a Broadband Meta-Surface,” *ACS Nano*, vol. 6, no. 8, pp. 6852–6861, Aug. 2012.

[192] M. L. Huang, Y. C. Chang, Y. H. Chang, T. D. Lin, J. Kwo, and M. Hong, “Energy-band parameters of atomic layer deposited Al2O3 and HfO2 on InxGa1-xAs,” *Appl. Phys. Lett.*, vol. 94, no. 5, p. 052106, Feb. 2009.

[193] G. Ertas, U. K. Demirok, A. Atalar, and S. Suzer, “X-ray photoelectron spectroscopy for resistance-capacitance measurements of surface structures,” *Appl. Phys. Lett.*, vol. 86, no. 18, p. 183110, Apr. 2005.

[194] H. Cohen, “Chemically resolved electrical measurements using x-ray photoelectron spectroscopy,” *Appl. Phys. Lett.*, vol. 85, no. 7, p. 1271, Aug. 2004.

[195] P. R. West, S. Ishii, G. V. Naik, N. K. Emani, V. M. Shalaev, and a. Boltasseva, “Searching for better plasmonic materials,” *Laser Photon. Rev.*, vol. 4, no. 6, pp. 795–808, Nov. 2010.

[196] Y. Jeyaram, S. K. Jha, M. Agio, J. F. Löffler, and Y. Ekinci, “Magnetic metamaterials in the blue range using aluminum nanostructures,” *Opt. Lett.*, vol. 35, no. 10, p. 1656, May 2010.

[197] A. Taguchi, Y. Saito, K. Watanabe, S. Yijian, and S. Kawata, “Tailoring plasmon resonances in the deep-ultraviolet by size-tunable fabrication of aluminum nanostructures,” *Appl. Phys. Lett.*, vol. 101, no. 8, p. 081110, 2012.

[198] S. K. Jha, Z. Ahmed, M. Agio, Y. Ekinci, and J. F. Löffler, “Deep-Ultraviolet Surface-Enhanced Resonance Raman Scattering of Adenine on Aluminum Nanoparticle Arrays.,” *J. Am. Chem. Soc.*, vol. 134, no. 4, pp. 1966–1969, Jan. 2012.

[199] Y. Yang, J. M. Callahan, T.-H. Kim, A. S. Brown, and H. O. Everitt, “Ultraviolet nanoplasmonics: a demonstration of surface-enhanced Raman spectroscopy, fluorescence, and photodegradation using gallium nanoparticles.,” *Nano Lett.*, vol. 13, no. 6, pp. 2837–41, Jun. 2013.

[200] M. Kanehara, H. Koike, T. Yoshinaga, and T. Teranishi, “Indium tin oxide nanoparticles with compositionally tunable surface plasmon resonance frequencies in the near-IR region.,” *J. Am. Chem. Soc.*, vol. 131, no. 49, pp. 17736–7, Dec. 2009.

[201] G. Garcia, R. Buonsanti, E. L. Runnerstrom, R. J. Mendelsberg, A. Llordes, A. Anders, T. J. Richardson, and D. J. Milliron, “Dynamically modulating the surface plasmon resonance of doped semiconductor nanocrystals.,” *Nano Lett.*, vol. 11, no. 10, pp. 4415–20, Oct. 2011.

[202] J. M. Luther, P. K. Jain, T. Ewers, and a P. Alivisatos, “Localized surface plasmon resonances arising from free carriers in doped quantum dots.,” *Nat. Mater.*, vol. 10, no. 5, pp. 361–6, May 2011.

[203] S. Q. Li, P. Guo, L. Zhang, W. Zhou, T. W. Odom, T. Seideman, J. B. Ketterson, and R. P. H. Chang, “Infrared Plasmonics with Indium–Tin-Oxide Nanorod Arrays,” *ACS Nano*, vol. 5, no. 11, pp. 9161–9170, 2011.

[204] G. V Naik, J. Liu, A. V Kildishev, V. M. Shalaev, and A. Boltasseva, “Demonstration of Al:ZnO as a plasmonic component for near-infrared metamaterials.,” *Proc. Natl. Acad. Sci. U. S. A.*, vol. 109, no. 23, pp. 8834–8, Jun. 2012.

[205] V. W. Brar, M. S. Jang, M. Sherrott, J. J. Lopez, and H. A. Atwater, “Highly confined tunable mid-infrared plasmonics in graphene nanoresonators.,” *Nano Lett.*, vol. 13, no. 6, pp. 2541–7, Jun. 2013.

[206] M. Abb, Y. Wang, N. Papasimakis, C. H. de Groot, and O. L. Muskens, “Surface-enhanced infrared spectroscopy using metal oxide plasmonic antenna arrays.,” *Nano Lett.*, vol. 14, no. 1, pp. 346–52, Jan. 2014.

[207] L. Yu, A. Rosenberg, and D. Wasserman, “All-semiconductor plasmonic nanoantennas for infrared sensing.,” *Nano Lett.*, vol. 13, no. 9, pp. 4569–74, Sep. 2013.

[208] H. J. Lezec, J. A. Dionne, and H. A. Atwater, “Negative refraction at visible frequencies.,” *Science*, vol. 316, no. 5823, pp. 430–2, Apr. 2007.

[209] T. Xu, A. Agrawal, M. Abashin, K. J. Chau, and H. J. Lezec, “All-angle negative refraction and active flat lensing of ultraviolet light.,” *Nature*, vol. 497, no. 7450, pp. 470–4, May 2013.

[210] K. E. Shafer-Peltier, C. L. Haynes, M. R. Glucksberg, and R. P. Van Duyne, “Toward a glucose biosensor based on surface-enhanced Raman scattering.,” *J. Am. Chem. Soc.*, vol. 125, no. 2, pp. 588–93, Jan. 2003.

[211] S. Nie, “Probing Single Molecules and Single Nanoparticles by Surface-Enhanced Raman Scattering,” *Science (80-.).*, vol. 275, no. 5303, pp. 1102–1106, Feb. 1997.

[212] J. C. Reed, H. Zhu, A. Y. Zhu, C. Li, and E. Cubukcu, “Graphene-enabled silver nanoantenna sensors.,” *Nano Lett.*, vol. 12, no. 8, pp. 4090–4, Aug. 2012.

[213] M. H. Chowdhury, K. Ray, S. K. Gray, J. Pond, and J. R. Lakowicz, “Aluminum nanoparticles as substrates for metal-enhanced fluorescence in the ultraviolet for the label-free detection of biomolecules.,” *Anal. Chem.*, vol. 81, no. 4, pp. 1397–403, Feb. 2009.

[214] G. H. Chan, J. Zhao, G. C. Schatz, and R. P. Van Duyne, “Localized Surface Plasmon Resonance Spectroscopy of Triangular Aluminum Nanoparticles,” *J. Phys. Chem. C*, vol. 112, no. 36, pp. 13958–13963, Sep. 2008.

[215] D. O. Sigle, E. Perkins, J. J. Baumberg, and S. Mahajan, “Reproducible Deep-UV SERRS on Aluminum Nanovoids,” *J. Phys. Chem. Lett.*, vol. 4, no. 9, pp. 1449–1452, May 2013.

[216] G. Maidecchi, G. Gonella, R. Proietti Zaccaria, R. Moroni, L. Anghinolfi, A. Giglia, S. Nannarone, L. Mattera, H.-L. Dai, M. Canepa, and F. Bisio, “Deep ultraviolet plasmon resonance in aluminum nanoparticle arrays.,” *ACS Nano*, vol. 7, no. 7, pp. 5834–41, Jul. 2013.

[217] M. a Ordal, L. L. Long, R. J. Bell, S. E. Bell, R. R. Bell, R. W. Alexander, and C. a Ward, “Optical properties of the metals Al, Co, Cu, Au, Fe, Pb, Ni, Pd, Pt, Ag, Ti, and W in the infrared and far infrared.,” *Appl. Opt.*, vol. 22, no. 7, pp. 1099–20, Apr. 1983.

[218] J. Martin, J. Proust, D. Gérard, and J. Plain, “Localized surface plasmon resonances in the ultraviolet from large scale nanostructured aluminum films,” *Opt. Mater. Express*, vol. 3, no. 7, p. 954, Jun. 2013.

[219] G. Maidecchi, G. Gonella, R. Proietti Zaccaria, R. Moroni, L. Anghinolfi, A. Giglia, S. Nannarone, L. Mattera, H.-L. Dai, M. Canepa, and F. Bisio, “Deep ultraviolet plasmon resonance in aluminum nanoparticle arrays.,” *ACS Nano*, vol. 7, no. 7, pp. 5834–41, Jul. 2013.

[220] B. Kasemo, C. Langhammer, and Z. Michael, “Gold, Platinum, and Aluminum Nanodisk Plasmons: Material Independence, Subradiance, and Damping Mechanisms,” *ACS Nano*, vol. 5, no. 4, pp. 2535–2546, 2011.

[221] S. J. Tan, L. Zhang, D. Zhu, X. M. Goh, Y. M. Wang, K. Kumar, C.-W. Qiu, and J. K. W. Yang, “Plasmonic color palettes for photorealistic printing with aluminum nanostructures.,” *Nano Lett.*, vol. 14, no. 7, pp. 4023–9, Jul. 2014.

[222] Y. Ekinci, H. H. Solak, and J. F. Löffler, “Plasmon resonances of aluminum nanoparticles and nanorods,” *J. Appl. Phys.*, vol. 104, no. 8, p. 083107, 2008.

[223] M. W. Knight, N. S. King, L. Liu, H. O. Everitt, P. Nordlander, and N. J. Halas, “Aluminum for plasmonics.,” *ACS Nano*, vol. 8, no. 1, pp. 834–40, Jan. 2014.

[224] F. Mazzotta, G. Wang, C. Hägglund, F. Höök, and M. P. Jonsson, “Nanoplasmonic biosensing with on-chip electrical detection.,” *Biosens. Bioelectron.*, vol. 26, no. 4, pp. 1131–6, Dec. 2010.

[225] E. Ozbay, “Plasmonics: merging photonics and electronics at nanoscale dimensions.,” *Science*, vol. 311, no. 5758, pp. 189–93, Jan. 2006.

[226] A. Hryciw, Y. C. Jun, and M. L. Brongersma, “Plasmonics: Electrifying plasmonics on silicon.,” *Nat. Mater.*, vol. 9, no. 1, pp. 3–4, Jan. 2010.

[227] J. a. Dionne, L. a. Sweatlock, M. T. Sheldon, A. P. Alivisatos, and H. A. Atwater, “Silicon-Based Plasmonics for On-Chip Photonics,” *IEEE J. Sel. Top. Quantum Electron.*, vol. 16, no. 1, pp. 295–306, 2010.

[228] C. Langhammer, M. Schwind, B. Kasemo, and I. Zoric, “Localized Surface Plasmon Resonances in Aluminum Nanodisks,” *Nano Lett., 8 (5), pp 1461–1471*, vol. 8, no. 5, p. pp 1461–1471, 2008.

[229] M. Surfaces, P. E. Laibinis, G. M. Whitesides, and D. L. Allara, “Comparison of the Structures and Wetting Properties of Self-Assembled Monolayers of,” pp. 7152–7167, 1991.

[230] F. Neubrech, A. Pucci, T. Cornelius, S. Karim, A. García-Etxarri, and J. Aizpurua, "Resonant Plasmonic and Vibrational Coupling in a Tailored Nanoantenna for Infrared Detection," *Phys. Rev. Lett.*, vol. 101, no. 15, p. 157403, Oct. 2008.

[231] S. Aksu, M. Huang, A. Artar, A. a Yanik, S. Selvarasah, M. R. Dokmeci, and H. Altug, "Flexible plasmonics on unconventional and nonplanar substrates.," *Adv. Mater.*, vol. 23, no. 38, pp. 4422–30, Oct. 2011.

[232] S. Ayas, A. Cupallari, O. O. Ekiz, Y. Kaya, and A. Dana, "Counting Molecules with a Mobile Phone Camera Using Plasmonic Enhancement," *ACS Photonics*, vol. 1, no. 1, pp. 17–26, Jan. 2014.

[233] H. Aouani, M. Rahmani, H. Šípová, V. Torres, K. Hegnerová, M. Beruete, J. Homola, M. Hong, M. Navarro-Cía, and S. a. Maier, "Plasmonic Nanoantennas for Multispectral Surface-Enhanced Spectroscopies," *J. Phys. Chem. C*, vol. 117, no. 36, pp. 18620–18626, Sep. 2013.

[234] P. Jouy, Y. Todorov, a. Vasanelli, R. Colombelli, I. Sagnes, and C. Sirtori, "Coupling of a surface plasmon with localized subwavelength microcavity modes," *Appl. Phys. Lett.*, vol. 98, no. 2, p. 021105, 2011.

[235] A. Hartstein, J. Kirtley, and J. Tsang, "Enhancement of the Infrared Absorption from Molecular Monolayers with Thin Metal Overlayers," *Phys. Rev. Lett.*, vol. 45, no. 3, pp. 201–204, Jul. 1980.

[236] R. Adato and H. Altug, "In-situ ultra-sensitive infrared absorption spectroscopy of biomolecule interactions in real time with plasmonic nanoantennas.," *Nat. Commun.*, vol. 4, p. 2154, Jan. 2013.

[237] P. Bassan, A. Sachdeva, J. Lee, and P. Gardner, "Substrate contributions in micro-ATR of thin samples: implications for analysis of cells, tissue and biological fluids.," *Analyst*, vol. 138, no. 14, pp. 4139–46, Jul. 2013.

[238] D. Dregely, F. Neubrech, H. Duan, R. Vogelgesang, and H. Giessen, "Vibrational near-field mapping of planar and buried three-dimensional plasmonic nanostructures," *Nat. Commun.*, vol. 4, p. 2237, Jan. 2013.

[239] A. E. Cetin, M. Turkmen, S. Aksu, D. Etezadi, and H. Altug, "Multi-resonant compact nanoaperture with accessible large nearfields," *Appl. Phys. B*, vol. 118, no. 1, pp. 29–38, Oct. 2014.

[240] A. E. Cetin, D. Etezadi, and H. Altug, "Accessible Nearfields by Nanoantennas on Nanopedestals for Ultrasensitive Vibrational Spectroscopy," *Adv. Opt. Mater.*, vol. 2, no. 9, pp. 866–872, Sep. 2014.

[241] S. Cataldo, J. Zhao, F. Neubrech, B. Frank, C. Zhang, P. V Braun, and H. Giessen, "Hole-mask colloidal nanolithography for large-area low-cost metamaterials and antenna-assisted surface-enhanced infrared absorption substrates.," *ACS Nano*, vol. 6, no. 1, pp. 979–85, Jan. 2012.

[242] C. Huck, A. Toma, F. Neubrech, M. Chirumamilla, J. Vogt, F. De Angelis, and A. Pucci, “Gold Nanoantennas on a Pedestal for Plasmonic Enhancement in the Infrared,” *ACS Photonics*, vol. 2, no. 4, pp. 497–505, Apr. 2015.

[243] Y. Shen, J. Zhou, T. Liu, Y. Tao, R. Jiang, M. Liu, G. Xiao, J. Zhu, Z.-K. Zhou, X. Wang, C. Jin, and J. Wang, “Plasmonic gold mushroom arrays with refractive index sensing figures of merit approaching the theoretical limit.,” *Nat. Commun.*, vol. 4, p. 2381, Jan. 2013.

[244] Y. Kaya, S. Ayas, A. E. Topal, H. Guner, and A. Dana, “Sensitivity comparison of localized plasmon resonance structures and prism coupler,” *Sensors Actuators B Chem.*, vol. 191, pp. 516–521, Feb. 2014.

[245] M. S. Jang, V. W. Brar, M. C. Sherrott, J. J. Lopez, L. Kim, S. Kim, M. Choi, and H. A. Atwater, “Tunable large resonant absorption in a midinfrared graphene Salisbury screen,” *Phys. Rev. B*, vol. 90, no. 16, p. 165409, Oct. 2014.

[246] V. Thareja, J.-H. Kang, H. Yuan, K. M. Milaninia, H. Y. Hwang, Y. Cui, P. G. Kik, and M. L. Brongersma, “Electrically tunable coherent optical absorption in graphene with ion gel.,” *Nano Lett.*, vol. 15, no. 3, pp. 1570–6, Mar. 2015.

[247] V. W. Brar, M. C. Sherrott, M. S. Jang, S. Kim, L. Kim, M. Choi, L. A. Sweatlock, and H. A. Atwater, “Electronic modulation of infrared radiation in graphene plasmonic resonators,” *Nat. Commun.*, vol. 6, p. 7032, May 2015.

[248] F. Neubrech, S. Beck, T. Glaser, M. Hentschel, H. Giessen, and A. Pucci, “Spatial extent of plasmonic enhancement of vibrational signals in the infrared.,” *ACS Nano*, vol. 8, no. 6, pp. 6250–8, Jun. 2014.

[249] D. J. Michalak, S. R. Amy, D. Aureau, M. Dai, A. Estève, and Y. J. Chabal, “Nanopatterning Si(111) surfaces as a selective surface-chemistry route.,” *Nat. Mater.*, vol. 9, no. 3, pp. 266–71, Mar. 2010.

[250] B. J. Eggleton, B. Luther-Davies, and K. Richardson, “Chalcogenide photonics,” *Nat. Photonics*, vol. 5, no. 3, pp. 141–148, Dec. 2011.

[251] S. Raoux, F. Xiong, M. Wuttig, and E. Pop, “Phase change materials and phase change memory,” *MRS Bull.*, vol. 39, no. 08, pp. 703–710, Aug. 2014.

[252] M. Wuttig and N. Yamada, “Phase-change materials for rewriteable data storage.,” *Nat. Mater.*, vol. 6, no. 11, pp. 824–32, Nov. 2007.

[253] A.-K. U. Michel, D. N. Chigrin, T. W. W. Maß, K. Schönauer, M. Salinga, M. Wuttig, and T. Taubner, “Using low-loss phase-change materials for mid-infrared antenna resonance tuning.,” *Nano Lett.*, vol. 13, no. 8, pp. 3470–5, Aug. 2013.

[254] A.-K. U. Michel, P. Zalden, D. N. Chigrin, M. Wuttig, A. M. Lindenberg, and T. Taubner, “Reversible optical switching of infrared antenna resonances with

ultrathin phase-change layers using femtosecond laser pulses," *ACS Photonics*, vol. 1, no. 9, pp. 833–839, Aug. 2014.

[255] P. Hosseini, C. D. Wright, and H. Bhaskaran, "An optoelectronic framework enabled by low-dimensional phase-change films," *Nature*, vol. 511, no. 7508, pp. 206–211, Jul. 2014.

[256] F. F. Schlich, P. Zalden, A. M. Lindenberg, and R. Spolenak, "Color Switching with Enhanced Optical Contrast in Ultrathin Phase-Change Materials and Semiconductors Induced by Femtosecond Laser Pulses," *ACS Photonics*, vol. 2, no. 2, pp. 178–182, Feb. 2015.

[257] K. Shportko, S. Kremers, M. Woda, D. Lencer, J. Robertson, and M. Wuttig, "Resonant bonding in crystalline phase-change materials.," *Nat. Mater.*, vol. 7, no. 8, pp. 653–8, Aug. 2008.

[258] M. Cretich, M. R. Monroe, A. Reddington, X. Zhang, G. G. Daaboul, F. Damin, L. Sola, M. S. Unlu, and M. Chiari, "Interferometric silicon biochips for label and label-free DNA and protein microarrays," *Proteomics*, vol. 12, no. 19–20, pp. 2963–2977, 2012.

[259] M. Cretich, A. Reddington, M. Monroe, M. Bagnati, F. Damin, L. Sola, M. S. Unlu, and M. Chiari, "Silicon biochips for dual label-free and fluorescence detection: Application to protein microarray development," *Biosens. Bioelectron.*, vol. 26, no. 9, pp. 3938–3943, 2011.

[260] R. Jenison, S. Yang, a Haeberli, and B. Polisky, "Interference-based detection of nucleic acid targets on optically coated silicon.," *Nat. Biotechnol.*, vol. 19, no. 1, pp. 62–65, 2001.

[261] P. Mitchell, "F EATURE A perspective on protein microarrays Proteins , not genes , are the true targets of medicines , but their analysis by array technology still poses significant challenges for drug developers .," *Nat. Biotechnol.*, vol. 20, pp. 225–229, 2002.

[262] P. F. Predki, "Functional protein microarrays: Ripe for discovery," *Curr. Opin. Chem. Biol.*, vol. 8, no. 1, pp. 8–13, 2004.

[263] M. Zhao, X. Wang, and D. D. Nolte, "Molecular interferometric imaging.," *Opt. Express*, vol. 16, no. 10, pp. 7102–7118, 2008.

[264] A. F. Coskun, A. E. Cetin, B. C. Galarreta, D. A. Alvarez, H. Altug, and A. Ozcan, "Lensfree optofluidic plasmonic sensor for real-time and label-free monitoring of molecular binding events over a wide field-of-view," *Sci. Rep.*, vol. 4, p. 6789, 2014.

[265] A. E. Cetin, A. F. Coskun, B. C. Galarreta, M. Huang, D. Herman, A. Ozcan, and H. Altug, "Handheld high-throughput plasmonic biosensor using computational on-chip imaging," *Light Sci. Appl.*, vol. 3, no. 1, p. e122, 2014.

[266] M. Perino, E. Pasqualotto, a De Toni, D. Garoli, M. Scaramuzza, P. Zilio, T. Ongarello, a Paccagnella, and F. Romanato, “Development of a complete plasmonic grating based sensor and its application to Self Assembled Monolayer detection,” vol. 53, no. 26, pp. 24–26, 2014.

[267] U. S. Dinish, F. C. Yaw, A. Agarwal, and M. Olivo, “Development of highly reproducible nanogap SERS substrates: Comparative performance analysis and its application for glucose sensing,” *Biosens. Bioelectron.*, vol. 26, no. 5, pp. 1992–1987, 2011.

[268] A. Gopinath, S. V Boriskina, W. R. Premasiri, L. Ziegler, B. M. Reinhard, and L. Dal Negro, “Plasmonic nanogalaxies: multiscale aperiodic arrays for surface-enhanced Raman sensing.,” *Nano Lett.*, vol. 9, no. 11, pp. 3922–9, Nov. 2009.

[269] A. Barhoumi and N. J. Halas, “Label-free detection of DNA hybridization using surface enhanced Raman spectroscopy.,” *J. Am. Chem. Soc.*, vol. 132, no. 37, pp. 12792–3, Sep. 2010.

[270] L. Rodríguez-Lorenzo, R. a Alvarez-Puebla, I. Pastoriza-Santos, S. Mazzucco, O. Stéphan, M. Kociak, L. M. Liz-Marzán, and F. J. García de Abajo, “Zeptomol detection through controlled ultrasensitive surface-enhanced Raman scattering.,” *J. Am. Chem. Soc.*, vol. 131, no. 13, pp. 4616–8, Apr. 2009.

[271] M. R. Gartia, A. Hsiao, A. Pokhriyal, S. Seo, G. Kulsharova, B. T. Cunningham, T. C. Bond, and G. L. Liu, “Colorimetrics: Colorimetric Plasmon Resonance Imaging Using Nano Lycurgus Cup Arrays (Advanced Optical Materials 1/2013),” *Adv. Opt. Mater.*, vol. 1, no. 1, pp. 1–1, 2013.

[272] R. de la Rica and M. M. Stevens, “Plasmonic ELISA for the ultrasensitive detection of disease biomarkers with the naked eye,” *Nat. Nanotechnol.*, no. October, pp. 2–5, 2012.

[273] R. de la Rica and M. M. Stevens, “Plasmonic ELISA for the detection of analytes at ultralow concentrations with the naked eye.,” *Nat. Protoc.*, vol. 8, no. 9, pp. 1759–64, 2013.

[274] E. Ozkumur, J. W. Needham, D. a Bergstein, R. Gonzalez, M. Cabodi, J. M. Gershoni, B. B. Goldberg, and M. S. Unlü, “Label-free and dynamic detection of biomolecular interactions for high-throughput microarray applications.,” *Proc. Natl. Acad. Sci. U. S. A.*, vol. 105, no. 23, pp. 7988–7992, 2008.

[275] G. G. Daaboul, R. S. Vedula, S. Ahn, C. a. Lopez, a. Reddington, E. Ozkumur, and M. S. Ünlü, “LED-based Interferometric Reflectance Imaging Sensor for quantitative dynamic monitoring of biomolecular interactions,” *Biosens. Bioelectron.*, vol. 26, no. 5, pp. 2221–2227, 2011.

[276] R. L. Stears, T. Martinsky, and M. Schena, “Trends in microarray analysis,” *Nat. Med.*, vol. 9, no. 1, 2003.

[277] S. Kumar Vashist, “Nanoparticles-Based Naked-Eye Colorimetric Immunoassays for In Vitro Diagnostics,” *J. Nanomed. Nanotechnol.*, vol. 05, no. 01, pp. 1–3, 2014.

[278] J. M. Slocik, J. S. Zabinski, D. M. Phillips, and R. R. Naik, “Colorimetric response of peptide-functionalized gold nanoparticles to metal ions,” *Small*, vol. 4, no. 5, pp. 548–551, 2008.

[279] M. A. Kats, D. Sharma, J. Lin, P. Genevet, R. Blanchard, Z. Yang, M. M. Qazilbash, D. N. Basov, S. Ramanathan, and F. Capasso, “Ultra-thin perfect absorber employing a tunable phase change material,” *Appl. Phys. Lett.*, vol. 101, no. 22, p. 221101, Nov. 2012.

[280] F. F. Schlich, P. Zalden, A. M. Lindenberg, and R. Spolenak, “Color Switching with Enhanced Optical Contrast in Ultrathin Phase-Change Materials and Semiconductors Induced by Femtosecond Laser Pulses,” *ACS Photonics*, vol. 2, no. 2, pp. 178–182, Feb. 2015.

[281] M. Piliarik, H. Sípová, P. Kvasnička, N. Galler, J. R. Krenn, and J. Homola, “High-resolution biosensor based on localized surface plasmons.,” *Opt. Express*, vol. 20, no. 1, pp. 672–80, 2012.

Appendix A

A.1. Effective index simulation in MIM geometry

```
clc;clear all;
LM=1000:10:10000;
AL_rakic;
nal=interp1(nk(:,1),nk(:,2),LM);
kal=interp1(nk(:,1),nk(:,3),LM);
emetal=(nal-sqrt(-1)*1e0*kal).^2;
dgap=[1e-9:1e-9:6e-9];

for pp=1:length(dgap)

   for lll=1:length(LM)
      d=dgap(pp);
      ed=1.6*1.6;
      lambda=LM(lll)*1e-9;
      w=2*pi*3e8/lambda;
      em=emetal(lll);
      k0=2*pi/lambda;
      kd=k0*sqrt(ed);
      km=k0*sqrt(em);
      b=0:k0/100:50*k0;
      kd=sqrt(b.^2-ed*k0*k0);
      km=sqrt(b.^2-em*k0*k0);
      xx=ed*km+em*kd.*tanh(kd*d/2);
      x2=abs(real(xx));
      qx=abs(imag(xx));
      bbb=b(find(x2==min(x2)));
      neff(pp,lll)=bbb/k0;

   end
end
```

A.2. Field Profile Simulation in Multilayer Coatings

```
clear all
close all
clc
m=1;
w=300:1:1000;
Al_rakic; %Refractive index of Al from Rakic
nag=interp1(nk(:,1),nk(:,2),w,'cubic','extrap');
kag=interp1(nk(:,1),nk(:,3),w,'cubic','extrap');

aSiPVD_nk;%Refractive index of aSi
nd=interp1(nk(:,1),nk(:,2),w,'cubic','extrap');
kd=interp1(nk(:,1),nk(:,3),w,'cubic','extrap')+0.0;

rr=zeros(1,length(w));
ii=1;
theta=THETA;
for tt=[80]
for WL=w
   n=[1.0 1.5 nd(ii)-sqrt(-1)*kd(ii) nag(ii)-sqrt(-1)*kag(ii) 1.5];
   t=[1200 tt 20 100 200     pol='tm';
   [EE position2 r t]=fresnelmultilayer_field(WL,n,t,pol,1);
   E(ii,:)=EE;
   rr2(ii)=r;
   ii=ii+1;
end
ii=1;
rrr(m,:)=rr2;
m=m+1;
end

plot(w,(abs(rrr).^2))
figure
imagesc((abs(rrr).^2))
figure
plot(position2,abs(E3([201],:)).^2);
```

A.3. Transfer Matrix Code

```
function [EE position r tt]=fresnelmultilayer_field(lamda,n,t,pol,res)
nn=length(n);
tt=length(t);

if (pol=='te')
   Ao=[1 1;n(1) -n(1)];
end

if (pol=='tm')
   Ao=[1 1;n(1) -n(1)];
end

M=eye(2);
for i=2:nn-1
   k=(2*pi/lamda)*n(i);
   Tm=[exp(sqrt(-1)*k*t(i)) 0;0 exp(-sqrt(-1)*k*t(i))];
   Am=[1 1;n(i) -n(i)];
   Amm=Am^-1;
   M=M*Am*Tm*Amm;
end
M=M;
kt=2*pi/lamda*n(nn);
dm=sum(t(2:(nn-1)));
X=Ao^-1*M*[exp(-sqrt(-1)*kt*dm);exp(-sqrt(-1)*kt*dm)*n(nn)];

%%Calculate Transmission and reflection coefficients
tt=1/X(1,1);
r=X(2,1)/X(1,1);
Eb=r*1;
Et=tt*1;

E=zeros(1,sum(t)/res);

EE=[];tf=0;
El=[1;Eb];
Al=Ao;
zz=[];
for i=2:nn-1

   z=[tf:res:tf+t(i)-res];
   zz=[zz z];
   tf=t(i)+tf;
   k=(2*pi/lamda)*n(i);
   Tm=[exp(sqrt(-1)*k*t(i)) 0;0 exp(-sqrt(-1)*k*t(i))];
   Am=[1 1;n(i) -n(i)];
   Er=Tm^-1*Am^-1*Al*El;
```

```
    Ei=Er;
    EE=[EE Ei(1,1)*exp(-sqrt(-1)*k*(z-tf))+Ei(2,1)*exp(sqrt(-1)*k*(z-tf))];
    El=Er;
    Al=Am;
end
    k=(2*pi/lamda)*n(1);
    kt=(2*pi/lamda)*n(nn);
    z1=[-t(1):res:-res];z2=sum(t(2:nn-1)+res):res:sum(t(2:nn-1))+t(nn);
    EE=[1*exp(-sqrt(-1)*k*(z1))+Eb*exp(sqrt(-1)*k*(z1)) EE Et*exp(-sqrt(-
1)*kt*(z2))];
    position=[z1 zz z2];
```